CENTRALIZATION AND SYNCHRONIZATION OF MILLIMETER-WAVE COORDINATED MULTI-POINT TRANSMISSION IN HETEROGENEOUS FIBER-WIRELESS ACCESS NETWORKS

A Dissertation
Presented to
The Academic Faculty

By

Lin Cheng

In Partial Fulfillment
of the Requirements for the Degree
Doctor of Philosophy in the
School of Electrical and Computer Engineering

Georgia Institute of Technology
May, 2017

CENTRALIZATION AND SYNCHRONIZATION OF MILLIMETER-WAVE COORDINATED MULTI-POINT TRANSMISSION IN HETEROGENEOUS FIBER-WIRELESS ACCESS NETWORKS

Approved by

Dr. Gee-Kung Chang, Advisor
School of Electrical and Computer Engineering
Georgia Institute of Technology

Dr. John R. Barry
School of Electrical and Computer Engineering
Georgia Institute of Technology

Dr. Xiaoli Ma
School of Electrical and Computer Engineering
Georgia Institute of Technology

Dr. Biing Hwang Juang
School of Electrical and Computer Engineering
Georgia Institute of Technology

Dr. Umakishore Ramachandran
School of Computer Science
Georgia Institute of Technology

Date approved: Feb 15, 2017

To world peace.

ACKNOWLEDGEMENT

I would like to take this great opportunity to express my sincere gratitude to the many people who have made this dissertation possible.

I would like to thank my advisor, Professor Gee-Kung Chang for his guidance, patience, and continuous support in the past five years. He has been creating an exceptionally innovative research environment which inspires me to explore novel theories and experiments. His vast industry experience and visionary academic leadership have always been helping me become a better researcher.

I would like to thank Professor Xiaoli Ma and Professor John Barry for serving as my reading committee members and their guidance in the area of wireless communications that has made this dissertation possible. I would like to thank Professor Biing Hwang Juang and Professor Umakishore Ramachandran for serving as my defense committee members and their valuable suggestions on my dissertation.

I would like to thank Dr. Xiang Liu from Futurewei Technologies, Inc. and Dr. Anthony Ng'oma from Corning Inc. for their inspiration and all the opportunities that they have made possible in my research and career.

I would like to thank Dr. Zhensheng Jia, Dr. Cheng Liu, Dr. M. M. Usman Gul, Dr. Ming Zhu, Jing Wang, Dr. Junwen Zhang, Mu Xu, Feng Lu, Hyunwoo Cho, Yahya M. Alfadhli, Shuyi Shen, Hyung Joon Cho, and many other graduate students and researchers for their unending support, encouragement, as well as friendship that have accompanied me during my study at Georgia Tech.

Lastly, I would like to thank my family for their unconditional love and support.

TABLE OF CONTENTS

LIST OF TABLES

LIST OF FIGURES

LIST OF ABBREVIATIONS

ADC	Analog-to-digital convertor
AGC	Automatic gain control
AP	Access point
AWG	Arbitrary waveform generator
AWGN	Additive white Gaussian noise
BBU	Baseband processing unit
BER	Bit-error rate
BF	Beamforming
BPF	Band-pass filter
BS	Base station
BTB	Back-to-back
C-RAN	Cloud radio access network
CA	Carrier aggregation
CAZAC	Constant-amplitude zero-autocorrelation
CD	Chromatic dispersion
CFO	Carrier frequency offset
CO	Central office
CoMP	Coordinated multi-point transmission
CP	Cyclic prefix
CPRI	Common public radio interface
CS/CB	Coordinated scheduling/beamforming
CSI	Channel state information
CTI	Cross-tier interference
CV	Coefficient of variation
CW	Continuous wave
CWDM	Coarse wavelength-division multiplexing
DAC	Digital-to-analog convertor
DAS	Distributed antenna system
DFB	Distributed feedback
DML	Directly modulated laser
DPS	Dynamic point selection
DSP	Digital signal processing
DWDM	Dense wavelength division multiplexing
EA	Electrical amplifier
EDFA	Erbium-doped fiber amplifier
EHF	Extremely high frequency (30 – 300 GHz)
eICIC	Enhanced inter-cell interference coordination
EIRP	Equivalent isotropic radiated power
eNB	Evolved NodeB
EVM	Error-vector magnitude
E/O	Electrical to optical

FCC	Federal Communications Commission
FDD	Frequency-division duplexing
FDE	Frequency-domain equalization
FE	Frontend
FEC	Forward error correction
FFR	Fractional frequency reuse
FFT	Fast Fourier transform
FPGA	Field-programmable gate array
FTTH	Fiber-to-the-home
FWM	Four-wave mixing
GNSS	global navigation satellite system
GPS	Global positioning system
HA	Horn antenna
HetNet	Heterogeneous network
HF	High frequency
HFC	Hybrid fiber coaxial
HGW	Home gateway
ICI	Inter-cell interference
ICIC	Inter-cell interference coordination
IEEE	Institute of Electrical and Electronics Engineers
IETF	Internet Engineering Task Force
IF	Intermediate frequency
IFFT	Inverse fast Fourier transform
i.i.d.	Independent and identically distributed
IL	Interleaver
IM	Intensity modulation
IoT	Internet of things
IP	Internet protocol
ISI	Inter-symbol interference
ITU	International Telecommunications Union
JP	Joint processing
JT	Joint transmission
LAA	Licensed assisted access
LoS	Line-of-sight
LTE	Long term evolution
LTE-A	LTE-Advanced
LTE-U	LTE in unlicensed spectrum
MIMO	Multiple-input and multiple-output
MMW	Millimeter-wave (30 – 300 GHz)
MRC	Maximal ratio combining
MWP	Microwave photonics
MZM	Mach-Zehnder modulator
NLoS	Non-line-of-sight
NTP	Network time protocol
O&M	Operations and maintenance
O/E	Optical to electrical

OA	Omnidirectional antenna
OBSAI	Open base station architecture initiative
OCS	Optical carrier suppression
OFC	Optical frequency comb
OFDM	Orthogonal frequency-division multiplexing
OIC	Optical interference cancellation
OOK	On-off keying
OSCM	Optical subcarrier multiplexing
PC	Polarization controller
PD	Photodetector
PM	Phase modulation / Phase modulator
ppb	Part per billion
ppm	Part per million
PSS	Primary synchronization symbol
PTP	precision time protocol
QAM	Quadrature amplitude modulation
RAN	Radio access network
RAU	Remote antenna unit
rms	Root mean square
RoF	Radio-over-fiber
RRM	Radio resource management
RRH	Remote radio head
RRU	Remote radio unit
Rx	Receiver
S-GW	Serving gateway
SDR	Software-defined radio
SFBC	Space-frequency block coding
SFO	Sampling frequency offset
SHF	Super high frequency (3 – 30 GHz)
SISO	Single-input and single-output
SNR	Signal-to-noise ratio
SSMF	Standard single-mode fiber
STBC	Space-time block coding
SyncE	Synchronous Ethernet
TDD	Time-division duplexing
TO	Time offset
TSP	Telecommunications service provider
Tx	Transmitter
UE	User equipment
UHF	Ultra high frequency (300 MHz – 3 GHz)
VHF	Very high frequency (30 – 300 MHz)
WiGig	Wireless Gigabit
WLAN	Wireless local area network
ZC	Zadoff-Chu (sequence)
ZF	Zero-forcing

SUMMARY

Millimeter-wave (MMW) frequencies (30 – 300 GHz) provide sufficient spectral resource and avoid interference with existing wireless services that are mostly congested over bands lower than 6 GHz. Different from lower frequencies, a high-throughput and power-efficient MMW wireless link highly relies on line-of-sight (LoS) propagation. To introduce coordinated multi-point (CoMP) transmission into MMW bands is a promising approach to provide higher chance of LoS propagation, as well as combat interference and improve system efficiency.

This dissertation studies the feasibility of MMW CoMP as an enabling technology handling the MMW spectrum resource for high-density small-cell applications. Exploratory study on the one hand shows the promising gains of MMW CoMP that improve signal quality, average capacity, and system stability. On the other hand, the study also reveals stringent requirements on synchronizations and massive information exchange between cell sites in MMW CoMP, implying the urgent needs for backhauling solutions that are suitable for MMW CoMP. However, current solutions for lower-frequency CoMP can hardly apply in MMW small cells because of the inherent difference between existing macrocells and MMW small cells.

From another aspect, a distributed MMW CoMP architecture generates massive overhead traffic over the backhaul and distributes inefficient MMW signaling to cell sites, and most importantly, its performance deteriorates from uncontrollable asynchronization between cells. As a preliminary study, this dissertation first investigates the impact of asynchronization in an MMW CoMP system. It shows the high vulnerability of downlink and its criteria of synchronization in both time and frequency. It also shows that

optimizing parameters including carrier frequency, bandwidth, and subcarrier spacing provides very limited improvement.

To explore effective solutions, this dissertation develops the concept of centralized MMW CoMP. Different from conventional ones, the concept proposed in this research is inherent from the fiber-wireless architecture that enables full centralization for MMW generation, signaling, distribution, synchronization, and coordination. It utilizes centralized resource and local high-capacity fiber links to provide global coherency for coordination, transparency for multiple access technologies, and seamless integration with cloud and virtualized radio access networks. Fiber-wireless systems for centralization are studied and their performance is experimentally investigated. The feasibility of fiber-wireless centralized MMW CoMP is theoretically validated. Experimental evaluation of a downlink MMW CoMP system with fiber-wireless centralization is also demonstrated with supportive results.

Effective techniques for different applications are enabled by the proposed concept. Three of them are proposed in this dissertation. The first proposed method for small-cell design improves MMW coverage and continuity in small-cell RANs, providing increased signal quality, improved link robustness, and smooth inter-cell handoff. The second proposed method of reconfigurable MMW radio bundling applies in multi-section fiber-wireless mobile fronthaul to improve infrastructure utilization rate and radio access quality and reliability. At last, the method of optical processing is studied facing the developing technologies of silicon photonics and all-optical processing. Enabled by the fiber-wireless platform, the method uses optical components in the centralized coordination module to realize interference cancellation and cooperative multiple-input and multiple-output (MIMO) across MMW small cells.

Validated by these proposed methods, the concept of centralized MMW CoMP facilitates joint processing by resource sharing, reduces the complexity and cost of cell sites by centralizing network hardware and functions, and optically provides high-quality

and transparent delivery of analog MMW signals. It centralizes all data and information and their processing power, leaving the cell sites no distributed intelligence for inter-cell communications, completely avoiding any form of overhead traffic. Enabled by fiber-wireless centralization, homogeneous MMW signals are optically generated and distributed, increasing the overall power and infrastructure efficiency. Most importantly, it allows CoMP transmitters to share the same signaling resource that provides identical time and frequency information and therefore guarantees inherent synchronization on both time and frequency.

CHAPTER 1 INTRODUCTION

1.1 Motivation

When our sapiens ancestors walked out of the vast land of Africa 70,000 years ago, our journey of proliferating the world began. We cultivated lands, voyaged across the oceans, built metropolitan cities that resided hundreds of thousands of people, and ushered in the Industrial Revolution. But still, if we could by any means send a modern man to a random location on this planet two hundred years ago, the chance that this person could detect any civilization would be extremely low no matter what modern equipment he might have in his backpack. This had barely changed until we stepped into the 19th century and learnt to use electromagnetic waves, waves that we cannot see, hear, or sense, and beyond our imagination, and sent them as the proof of human civilizations to each corner on the planet surface, or even thousands of kilometers beyond it.

Electromagnetic waves were the fire seed of this modern civilization evolution, and they lit up the information explosion nowadays. In 1895, Guglielmo Marconi developed the first wireless telegraphy system sending and receiving "Hertzian waves"[1]. 120 years later, these waves carried 3.7 EB[2] of data serving 8 billion mobile devices every month [1]. The expansion of the application of electromagnetic waves has become a metric to measure the modernization of civilization, as the more metropolitan an area is the more wireless communications there will occur. People rely on electromagnetic waves to have wireless communications, and wireless communications help people to access information. They are acting like free nerve endings in the body of this society, sensing and connecting everyone and eventually everything via the internet of things (IoT), to the brain that runs cloud computing [2].

[1] Electromagnetic waves were initially called "Hertzian waves" after discovered by Heinrich Hertz in 1886.
[2] EB = Exabyte; 1 EB = 10^{18} B.

Every wireless communication needs its spectrum. In today's ecosystem, spectral resource is the capital of wireless services. Engineers maximize the information profit by increasing the spectral efficiency; service providers bid for new spectrum; and commissioners regulate the usage. Spectra at different frequencies have different properties, attracting different applications, investments, and development. Bands from VHF (30 – 300 MHz) to UHF (300 MHz to 3 GHz) have low atmospheric absorption, high penetrability, and low hardware complexity, making them ideal for macrocell or non-line-of-sight (NLoS) wireless services. In fact, most current wireless services that rely on these factors tend to be around these frequencies. For example, all 50 standardized LTE bands are below 6 GHz, and 46 of them are within UHF [3]. Consequently, these most precious frequencies are already well exploited today. With the upcoming 5G era, people are shifting the battlefield to SHF (3 – 30 GHz), or even the last frontier, EHF (30 – 300 GHz), also known as MMW frequencies.

Wireless communications are not only about spectrum, but also the effectiveness of information delivery. The majority of users do not care about how much spectrum they can use but more about how fast they can download a Snapchat video. The peak rate supported by LTE-A today is 1 Gb/s. Although MMW bands have more promising spectral resource and bandwidth, their high frequencies and high propagation loss keep us from utilizing them in the same way as utilizing UHF. A new wireless communication model has to be re-designed to make these upcoming MMW wireless links overcome their inherent defects. From the wireless aspect, we want to endow these links the ability to smartly cooperate and coordinate with each other to strengthen themselves. From the network aspect, this change in wireless communications leads our attention to the communications behind – the radio access network (RAN).

A RAN provides connections between the wireless coverage and the core network. Wireless coverage works like free nerve endings, while a RAN works like the neurons that connect these endings with the central nervous system. Most of the links in a

RAN are optical fibers nowadays. These links are hidden under the ground, just like the peripheral nervous system hidden under our skins all over our bodies. New types of MMW communications need supports from new types of RANs, just like different types of nerve endings are connected by different types of neurons. This involves the change of the function distribution over the fiber links, and the distribution of the fibers themselves.

In fact, the use of optical fiber is another fire seed in this civilization evolution. In 1960s, Charles K. Kao, known as the "Father of Fiber Optics" and also the Nobel Laureate, together with his colleague George A. Hockham promoted the idea that the attenuation in optical fibers could be reduced below 20 dB/km, making fibers a practical candidate for communications. In 1970, four researchers[3] from Corning Glass Works demonstrated a fiber with 17-dB/km attenuation. Today, with the attenuation below 0.2 dB/km, optical fibers have become the primary, or even *the only* medium for broadband communications. They spread under the ground, over the mountains, and across the oceans, connecting every human civilization like the nervous system of the planet. The arrival of MMW communications extends these nerve fibers to more cells with new forms of functionalities.

This evolution motivates us to rethink the relationship between the two fire seeds. From MMW to optical fibers, there are many questions that we need to answer before we can make MMW an efficient resource for interoperable and sustainable wireless communications based on current fiber networks. How to establish a reliable MMW coverage? How to backhaul these coverage cells? What is the RAN architecture? How to deploy fiber links to realize this architecture? To try to answer these questions, this dissertation summarizes some of the work that may help us reveal the concealed connection between MMW wireless communications and optical fiber communications.

[3] Robert D. Maurer, Donald Keck, Peter C. Schultz, and Frank Zimar.

1.2 Background and Challenges

1.2.1 Interference and coordination

To satisfy the dramatic growth of mobile data access, heterogeneous networks (HetNets) have proven their potentials of increasing data rates and proximity to end users by providing multi-tier coverage and allowing more efficient traffic offload, indoor coverage, and spatial spectrum reuse [4]. However, the desirable scheme of full frequency reuse and the trend of cell densification for high area spectral efficiency in a HetNet lead to unavoidable cross-tier interference (CTI) and inter-cell interference (ICI) resulting from the overlapping coverage of cells [5, 6], as shown in Fig. 1.

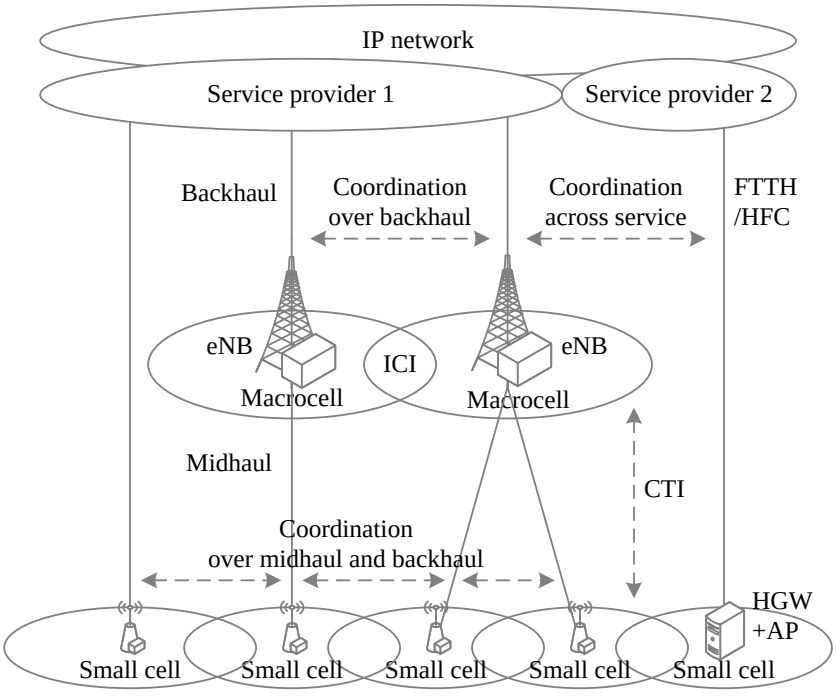

Fig. 1. CTI, ICI, and coordination in a distributed HetNet.

To mitigate ICI and CTI in a HetNet, coordination methods are adopted in LTE [7]. ICI coordination (ICIC) is introduced in LTE R8 as inherently a multi-cell radio resource management (RRM) function that takes into account information from multiple

cells and let eNBs communicate via the X2 interface[4] to mitigate ICI for users at the cell edge [8]. In LTE-A R10, ICIC has evolved to enhanced ICIC (eICIC) to better support HetNet deployments with the major change of the addition of time domain ICIC [9].

On top of eICIC, CoMP is introduced in LTE-A R11 [10]. CoMP either avoids interference or exploits the destructive interference into constructive signal combination. CoMP can jointly work with eICIC to provide extra gains [11, 12]. Other than interference mitigation, CoMP has the following advantages.

1) It enhances signal quality by increasing diversity in both downlink and uplink and increasing signal-to-noise ratio (SNR) in downlink.
2) It improves infrastructure utilization by providing users connections to multiple cells and making use of idle or under loaded cells.
3) It increases the chance of LoS communications by providing multiple wireless links over densified small cells.

CoMP transmission in LTE-A is categorized into two categories: coordinated scheduling/beamforming (CS/CB) and joint processing (JP) [10, 13]. In CS/CB, data for user equipment (UE) are only available at and transmitted from one point in the CoMP cooperating set for a time-frequency resource but user scheduling/beamforming decisions are made with coordination among points corresponding to the CoMP cooperating set. In this category, limited data are exchanged between cells for the purpose of multi-cell interference-aware link adaptation and scheduling. Each point adjusts its transmitting or receiving strategy according to some knowledge on ICI which does not require explicit information exchange between cells.

In JP, data for a UE is available at more than one point in the CoMP cooperating set for a time-frequency resource. The data are processed and exchanged among cells. One here considers non-coherent and coherent schemes, where the latter aims at aligning

[4] Logic link in LTE for communications between eNBs.

the phases of signals transmitted from multiple points. This requires precise synchronization between all involved entities. There are two sub-categories under JP. The first is joint transmission (JT) in which data are simultaneously transmitted from multiple points to a single UE or multiple UEs in a time-frequency resource, e.g. to improve the received signal quality and/or data throughput. The second is dynamic point selection (DPS) in which data are transmitted from one point within the CoMP cooperating set in a time-frequency resource although data are available simultaneously at multiple points.

This dissertation will focus on JT under JP.

CoMP can also be categorized as distributed and centralized CoMP schemes, referring to where the subject of cooperation takes place [13]. This dissertation will reveal the necessity of using centralized CoMP in MMW small cells.

CoMP improves HetNet performance, whereas brings stringent challenges. Conventional eICIC and CoMP techniques in LTE-A coordinate eNBs over serving gateways (S-GWs) and X2 logical links and involve backhaul/midhaul communications [14]. Their process is mainly accomplished in a digital and distributed manner. CoMP, especially JP, requires close cooperation between different eNBs. It generates significant overhead traffic across cell sites to enable coordination and also imposes stringent requirements on capacity, delay, and synchronization [15]. In a 10-MHz LTE-A X2 link, for instance, the capacity consumption is up to 4 Gb/s with a latency limitation of 1 ms [16]. This number will go even higher if the signal bandwidth does or carrier aggregation (CA) is applied [17].

In a HetNet, the access service is built on a variety of infrastructures, service providers, and cellular architectures, as shown in Fig. 1. Within a telecommunications service provider (TSP), coordination involves communications across various mobile backhaul and midhaul links with different requirements [18]. Coordination between different TSPs is also under research for better interoperability and more efficient

spectrum utilization [19]. Furthermore, to better serve small-cell users in a HetNet with high diversity in the future, the need for coordination is expected to be across different services (e.g. service provider 1 and 2 in Fig. 1) to allow small cells with different protocols to coexist, such as WiFi and licensed assisted access (LAA) (also known as LTE-U) [20]. To backhaul an inter-service coordination is extremely challenging considering their completely different network architectures and protocols. What makes it worse, wireless local access networks (WLANs) as the largest small cell market are mostly user-deployed over access points (APs) and home gateways (HGWs) accessed by fiber-to-the-home (FTTH) or hybrid fiber coaxial (HFC), as shown in Fig. 1. These unplanned WLANs perform more unpredictably than TSP-deployed small cells.

As FCC's approval of 27.5-29.5, 37-40.5, 47.2-50.2, 50.4-52.6, and 59.3-71 GHz for 5G study [21], MMW bands have become a strong candidate of spectral resource for future RANs. Considering the multi-GHz bandwidths and the high carrier frequencies of MMW, the requirement and consequent consumption for coordination between MMW cells will be significantly higher than current standards. More importantly, coordination requires accurate synchronization among different points. A distributed CoMP architecture for indoor small cells in a distributed HetNet can hardly have access to an effective reference clock, highly relying on backhaul support [22]. The deployment of MMW small cells will make their coordination more backhaul-dependent. JP for MMW small cells will especially become more challenging because of its high backhaul consumption, small latency tolerance, stringent phase control and synchronization, and also the narrow beam widths of MMW signals over a small cell size [23].

1.2.2 MMW wireless communications

MMW wireless communications exploit sufficient spectral resources to provide much more abundant bandwidths than current services operating below 6 GHz [24]. For example, IEEE 802.11ad provides 2.16 GHz on each channel while 11ac can only

support up to 160 MHz by channel binding. The use of MMW frequencies effectively avoids CTI with existing cells and allows the coexistence of cells from multiple tiers in a HetNet by providing spectral diversity [25, 26].

On top of the free-space path loss of $(4\pi d/\lambda)^2$, different MMW frequencies have different levels of attenuation attributed to atmospheric absorption [27]. Those being part of the reason, MMW radios have propagation properties and channel modelling different from UHF. By far, there has not been a general model that is popular accepted by researchers for channel modelling in MMW bands [28]. Generally, compared with UHF, MMW bands have higher loss from diffuse scattering because of smaller wavelengths, weaker multipath effect from less pronounced reflected and scattered energy, and lower rms delay spread from directional links [29]. For indoor coverage, high reflection and diffraction loss and low penetrability (derived from comparison between [30] and [31]) make MMW radio sensitive to shadowing [32, 33]. The high loss and low penetrability determine that MMW is more suitable for high-proximity small-cell coverage [34].

To compensate the high free-space power loss of isotropic propagation, antenna array or directional antennas are used. The small wavelengths of MMW frequencies facilitate the use of a large number of antenna elements in a compact form factor to synthesize highly directional beamforming (BF) corresponding to large array gains [35]. Also thanks to the short wavelengths and small antenna elements, massive MIMO can increase the capacity and reliability [36]. Directional beams can also mitigate ICI in densely deployed MMW infrastructure which is the precondition of high coverage and capacity [37]. Therefore, MMW is more suitable for minor-mobility, high-density high-directional small-cell coverage.

Other than wireless access, MMW has also applications such as WirelessHD, WiGig (IEEE 802.11ad and ay), satellite communications, and also security screening. As part of a RAN, MMW can also be used for backhauling in place of fiber cables. There are already commercial systems deployed. For example, CableFree® with Gb/s MMW

links is fast to deploy, flexible, and has lower cost than fibers [38]. Research works are also reported for similar application with high capacity and long distance [39, 40].

However, challenges attributed to the characteristics of MMW radio exist in these applications, especially in wireless access. Firstly, MMW communication quality is sensitive to environmental conditions. Obstacles in the LoS link may cause complete transmission failure, especially for frequencies that have low penetrability such as the 60-GHz band [41]. Secondly, the density of cells increases as the cell size decreases, and consequently the chance of ICI goes up and the utilization of each cell goes down, leading the network less efficient and more sensitive to user distributions [42]. Thirdly, the high frequencies of MMW radio require state-of-the-art microwave components for MMW generation, distribution, and processing. The quality of these components may have impact on system-wide stability, synchronization, and complexity [43].

1.2.3 Fiber-wireless centralization

Fiber-wireless centralization is a design that shifts the functionality of a RAN from the wireless access site to a centralized unit over the fiber connections between them. The concept of fiber-wireless centralization is promoted by the architecture of centralized or cloud RAN (C-RAN) [44].

In traditional distributed RANs, as shown in Fig. 2(a), each base station (BS) has its own baseband processing power and hardware. These BSs are located at cell sites and are connected to the core that has the function of S-GW through digital backhaul. For small cells, the BSs are either connected to the core through backhaul or a macrocell BS through midhaul. As the cell size reduced and the cell amount increased in future mobile networks, it will be too expensive to build, upgrade, or operate the network, as each cell needs its own BS at the cell site, even though the BS utilization rate is low. Therefore, it is necessary to centralize baseband functions and eliminate the BSs, and allow users and services to share the baseband functions.

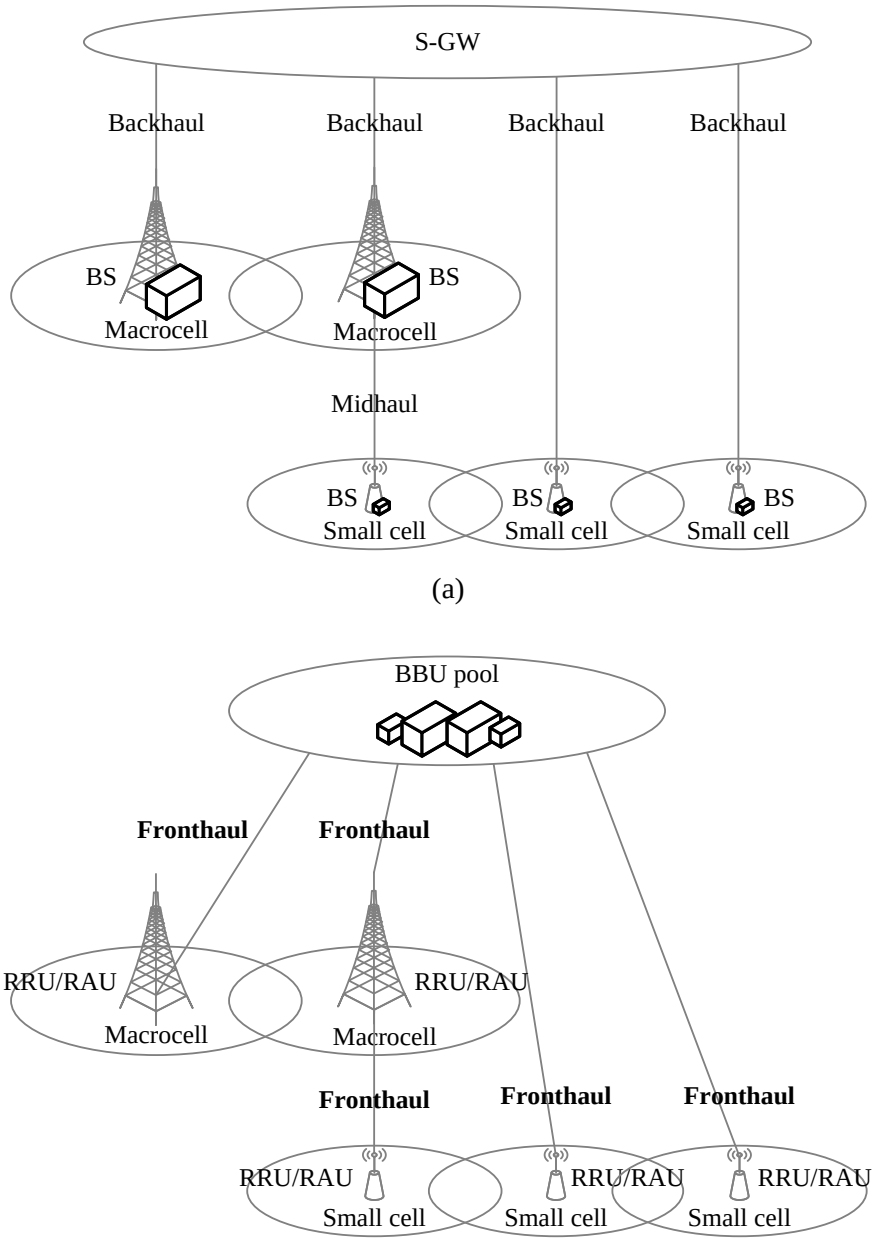

Fig. 2. Architectures of (a) distributed RAN and (b) C-RAN.

On the contrary, Fig. 2(b) shows the architecture of a C-RAN. In this architecture, the baseband units (BBUs) as part of the BS are shifted from the cell sites to a BBU pool. Only limited functions reside at cell sites as the remote radio units (RRUs). The connections between the BBU pool and the RRUs (for both macrocells and small cells)

are called mobile fronthaul [18]. This C-RAN architecture provides a solid solution for high-throughput MMW access with aspects of superiorities.

1) The RRUs are well simplified, which reduces the cell site room, power consumption, and demands for technical support, being promising for cell densification.
2) The number of BSs (not the number of cells) can be reduced several folds by virtualization and BBU sharing among RRUs.
3) It is more friendly for centralized operations and maintenance (O&M), upgrade, open platform, and smooth service expansion and evolution.
4) It enables more flexible RRM that makes the network more adaptive to various movement and distribution of UEs and achieves more efficient ICIC.
5) It enables centralized processing for CoMP, especially JP.
6) Most of inter-cell communications occur inside the BBU pool with minimized delay.
7) The most important, this centralized RAN architecture can realize resource sharing, including hardware, signaling, user data, channel state information, as well as peripheral infrastructure.

Different degrees of fiber-wireless centralization are possible in C-RANs. For example, Layer 2 and 3 and O&M are located within the BBU pool while Layer 1 is located within RRUs [44]; this is a partial centralization scheme. [45] and [46] also talk about how to split within Layer 1 for different degrees of partial centralization. A full centralization scheme is achieved when all layers and all baseband functions are located within the BBU pool. Different degrees of centralization have different line rates over the fronthaul and also outperform in different scenarios. Full centralization outperforms other partial centralization in CoMP scenarios [47]. To realize full centralization, waveforms

for UEs are generated at the BBU pool and are delivered over fronthaul, in either digital or analog formats.

Digital fronthaul solutions such as common public radio interface (CPRI) and open base station architecture initiative (OBSAI) are straight-forward, high-fidelity, and robust approaches to fulfill basic LTE bandwidth needs [48, 49]. They digitize the baseband LTE waveforms into an on-off key (OOK) stream to transmit over fronthaul. CPRI and OBSAI are popularly used in current distributed RANs as interfaces for fronthaul that connects BSs at the bottom of or near cell sites with RRUs or remote radio heads (RRHs) at the top of cell sites. However, their low efficiency will require unaffordable high-speed transceivers and limit any further bandwidth improvement when they are applied in future RANs. In CPRI, as an example, a 20-MHz LTE signal takes up to 10-Gb/s fronthaul rate [50]. When a 5-channel CA is applied, a 50-Gb/s speed will eventually consume all transceiver capacity. Moreover, in both CPRI and OBSAI, their digital interfaces causing unavoidable delay and jitter are unfriendly to high-speed services that require precise synchronization such as CoMP and CA.

Radio over fiber (RoF) is an analog solution to realize full fiber-wireless centralization and has even a higher degree of centralization than the digital solutions [51, 52]. RoF generates and optically modulates ready-to-radiate radio signals inside a central office (CO) that also accommodates the BBU pool, and transmits the signals over fiber links to cell sites. At cell sites, optical signals are detected to radio signals and directly radiated. The unit that realizes these analog functions at a cell site is called remote antenna unit (RAU), to be differentiated from RRUs in partial centralization schemes or digital full centralization solutions. On top of the seven aspects of the superiorities of C-RAN aforementioned, a C-RAN with RoF-based full centralization has the following advantages.

1) It minimizes the complexity of RAUs and avoids the excessive use of multi-Gb/s digital transceivers.

2) It maximizes resource sharing.
3) Compared with digital solutions, it supports multiplexed bands (e.g. bands for multi-antenna) and the coexistence of multiple access technologies [53, 54].
4) It outperforms in high-capacity access systems by allowing optical multiplexing such as dense wavelength-division multiplexing (DWDM) [55].
5) All inter-cell communications occur inside the BBU pool with minimized delay.
6) It guarantees the inherent synchronization among RAUs on both frequency and time.
7) Its fiber-optic platform simplifies the generation and distribution of homogeneous MMW signals [56], provides a friendly interface for optical processing, and enables the equalization of MMW wireless channel matrices from the optical domain [57].

In Section 4.1 we will look into more details of RoF technology for full fiber-wireless centralization.

1.3 Logic of Dissertation

The objective of this research is to study CoMP transmission and corresponding architectures and methods that improve reception quality in MMW wireless communications. The main technical areas involve MMW wireless communications, CoMP, digital signal processing, fiber-wireless technologies, and optical fiber communications.

The logic of this dissertation follows the diagram in Fig. 3. Each block is a topic that this dissertation is going to study in order to provide potential solutions to objective problems. The highlighted parts are the proposed core concept and corresponding methods.

In Chapter 1 (C1 in Fig. 3), we have introduced the motivation, advantages, and consequent problems of the application of MMW wireless communications in future HetNets and also other related background knowledge. In Chapter 2 (C2 in Fig. 3), we will study MMW CoMP as a potential research direction to solve the problems in MMW wireless communications such as LoS propagation, ICI, and low network efficiency. Gains of MMW CoMP are theoretically analyzed in two downlink modes. Problems of MMW CoMP are also observed. In Chapter 3 (C3 in Fig. 3), we will focus on one of the problems of MMW CoMP, synchronization problem, by giving both simulation and experimental study results that verify the importance and rigor of synchronization in MMW CoMP. Not being able to find an effective solution for synchronization in MMW CoMP from current technologies for lower frequencies, this dissertation proposes a concept of centralized MMW CoMP in Chapter 4 (C4 in Fig. 3). This is the core contribution and novelty of the dissertation. We will experimentally validate the fiber-wireless architecture that provides centralization and then verify the feasibility of centralized MMW CoMP both theoretically and experimentally. The proposed concept not only provides synchronization but also facilitates MMW signal generation and eases backhauling requirements. In Chapter 5 (C5 in Fig. 3), we will propose and experimentally study three techniques based on the concept of centralized MMW CoMP, including cell grouping for small-cell design, radio bundling for mobile fronthaul, and optical processing. At last, we will summarize this work and propose potential future research in Chapter 6.

Some notations are hereby explained. In the following part of the dissertation, we will use the term “MMW” to represent microwaves with frequencies between 30 and 300 GHz, and the term “high frequency (HF)” to generally represent frequencies below 6 GHz (note that this is different from the HF defined by ITU between 3 and 30 MHz). Also, in all experimental works we only use frequencies around 60 GHz because of

license issues. Consequently, the frequency range experimentally verified by this work is narrower than what the theory of this dissertation may apply.

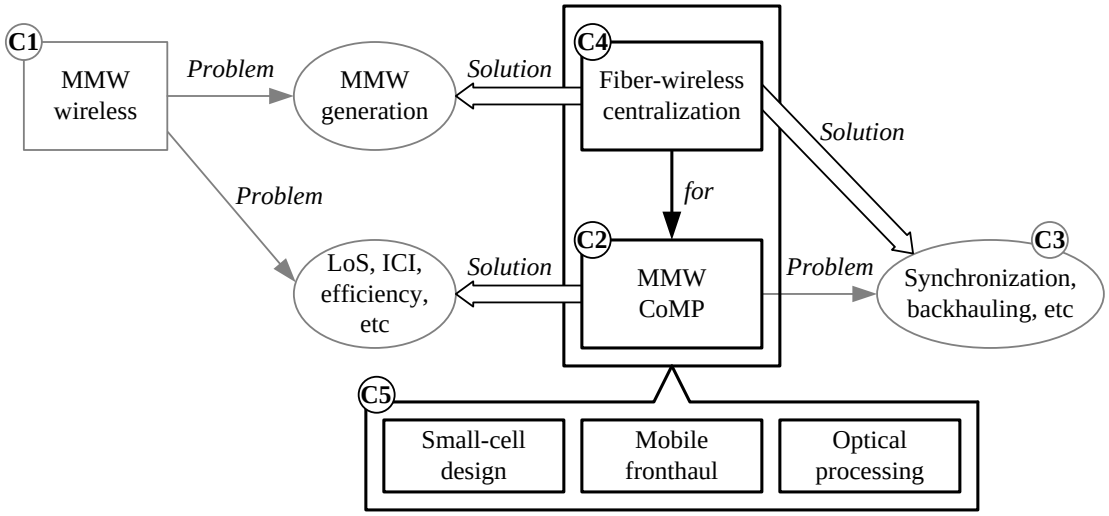

Fig. 3. Flow chart of dissertation logic.

CHAPTER 2 MMW CoMP TRANSMISSION

In MMW wireless small cells, problems attributed to the characteristics of MMW wireless signals exist. The quality of MMW communications is sensitive to environmental conditions. Obstacles in the LoS link may cause complete transmission failure, especially for frequencies that have low penetrability such as the 60-GHz band. Therefore, multiple LoS links are needed for redundant paths. In addition, cell densification leads to decreased utilization and cell sizes, making the network less efficient in terms of infrastructure investment. As a result, the coordination of MMW cells is necessary mechanism to reduce ICI, increase the chance of LoS, and improve network efficiency.

In this chapter, we will introduce CoMP transmission into the domain of MMW communications. Downlink transmission is highlighted with two downlink CoMP modes, space-frequency block coding (SFBC) and BF. We will study the gains that they can provide in MMW CoMP.

The main differentiator between the study of MMW CoMP and HF CoMP is the completely different channel characteristics of MMW. Actually, both SFBC and BF need channel state information (CSI) for either decoding or precoding. In HF wireless communications, the CSI represents the combined effect of, for example, scattering, fading, and power attenuation and changes over both time and frequency. However, in MMW, the channel is fairly flat with very slow change, which will be verified in Section 4.1. This allows us to represent the channel response in a much simpler form as stated in Section 2.3.

In the following of this chapter, we will use a very basic 2×1 MMW CoMP model as shown in Fig. 4 to study the realization, feasibility, and downlink gains of MMW CoMP based on SFBC and BF.

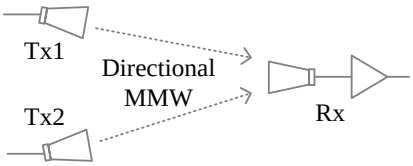

Fig. 4. Basic downlink 2×1 MMW CoMP transmission model.

2.1 Block Coding for MMW CoMP

SFBC is an Alamouti block coding method [58, 59]. It applies coding over the subcarriers in an orthogonal frequency-division multiplexing (OFDM) symbol. It is used as a coding scheme for diversity mode in LTE [60].

Table I. Subcarrier allocation in SFBC

	Subcarrier L	Subcarrier R
Tx1	x_1	x_2
Tx2	$-x_2^*$	x_1^*

In a 2×1 CoMP transmission scenario in Fig. 4, both Tx1 and 2 start transmitting coded OFDM symbols containing the same information at a certain time. Table I shows a coding pattern of SFBC, in which Tx1 has quadrature amplitude modulation (QAM) symbols x_1 and x_2 on two adjacent OFDM subcarriers (denoted by L and R) in a coding block while Tx2 has their (negative) conjugates on the same subcarrier pair. At Rx, received symbols y_L and y_R at subcarriers L and R are represented as

$$\begin{cases} y_L = h_{1,L}x_1 - h_{2,L}x_2^* + noise \\ y_R = h_{1,R}x_2 + h_{2,R}x_1^* + noise \end{cases} \quad (1)$$

or

$$\begin{pmatrix} y_L \\ y_R^* \end{pmatrix} = \begin{pmatrix} h_{1,L} & -h_{2,L} \\ h_{2,R}^* & h_{1,R}^* \end{pmatrix} \begin{pmatrix} x_1 \\ x_2^* \end{pmatrix} + \mathbf{N} = \mathbf{HX} + \mathbf{N}, \tag{2}$$

where $h_{i,j}$ is the channel response from Tx-i (i = 1 or 2) to Rx at subcarrier j (j = L or R) at the time of current OFDM symbol and **N** is the noise vector.

When zero-forcing (ZF) equalizer is used [61], the original symbols are recovered as

$$\hat{\mathbf{X}} = \hat{\mathbf{H}}^{-1} \begin{pmatrix} y_L \\ y_R^* \end{pmatrix} = \hat{\mathbf{H}}^{-1}\mathbf{HX} + \hat{\mathbf{H}}^{-1}\mathbf{N}, \tag{3}$$

where $\hat{\mathbf{H}}$ is the estimate of **H**. If the channel is considered flat, which *is* the practical case as we will see in Section 4.1, then $\hat{\mathbf{H}}$ can be simplified to

$$\hat{\mathbf{H}} = \begin{pmatrix} \hat{h}_1 & -\hat{h}_2 \\ \hat{h}_2^* & \hat{h}_1^* \end{pmatrix}. \tag{4}$$

There are also other decoding methods for different equalization criteria and performance under different system scenarios [62, 63]. However, in the following study we will always use the decoding in (3) so that observations on the condition number of **H** are also included.

Table II. Symbol allocation in STBC

	Symbol k	Symbol k+1
Tx1	x_1	x_2
Tx2	$-x_2^*$	x_1^*

Compared with space-time block coding (STBC), whose 2×1 example is expressed in Table II, SFBC is more suitable for multi-subcarrier systems that have flat channel but fast fading [64]. The analysis of gains in 2.3.2 can similarly apply on STBC but with different representation and outcomes. Besides the consideration of the

compatibility to LTE, the flatness of the channel of MMW transmission is also the motivation and precondition of using SFBC rather than STBC to provide CoMP gains.

2.2 Beamforming for MMW CoMP

Single-cell beamforming (BF) is a multi-antenna technique that uses multiple co-located transmitters to enhance signal reception at dedicated mobile users and at the same time null or weaken that signal at other users. In a single-cell single-user scenario, the realization of BF is to keep signals from all transmitters in-phase and constructive at the receiver.

In CoMP transmission, single-cell BF within each cell is well scheduled to reduce ICI. This behavior is categorized as the CS/CB class, in which the core computation, in fact, is still single-cell. It is to minimize the interference between cells but does not have coherent transmission behaviors between transmitters from different cells and, as a result, information and data exchange between different transmitters located at different locations are minimized.

In MMW applications, single-cell BF is essential to provide power gain at the receiver, and CS/CB can still be used to avoid ICI (although may not be as efficient or effective as the case in HF considering the highly directional beams and large propagation loss of MMW). On top of them, to solve problems such as NLoS, multi-cell BF from multiple points is proposed to be used in this dissertation. For a single user, multi-cell BF establishes multiple radio paths to enhance the chance of LoS. Transmitters from these multiple points send identical data and coherent radio to this UE and maintain the in-phase relation at the receiver. Data and channel information for this UE have to be shared among all transmitters for JP. For multiple users, JP based on all UEs' data and channel information is established involving all the transmitters from the CoMP cooperating set.

Although we use the name "BF", but the BF mode that we will be mentioning for the rest of this dissertation is actually multi-cell BF and cannot be categorized into the CS/CB class. It is actually a coherent scheme under the JT sub-category introduced in 1.2.1 with full sharing of data, channel information, and processing among transmitters.

Noting that directional beams are applied for MMW, a multi-user scenario can still be treated as an overlay of the single-user BF scenario aforementioned from each UE's view. As a result, we will still use the directional 2×1 model shown in Fig. 4.

To realize BF, both Tx1 and 2 start transmitting symbol x over a certain subcarrier at a certain time. Denoting h_i as the channel response from Tx-i (i=1 or 2) to Rx at the subcarrier frequency at the time of current OFDM symbol and $\hat{h}_i$ as the estimate of h_i, a simple way to make sure that the two signals are in-phase at the receiver without changing the Tx power is to pre-code x into $\hat{h}_i^* x / |\hat{h}_i|$ at Tx-i when $\hat{h}_i \neq 0$. Therefore, the received BF signal is

$$y = \left(\frac{\hat{h}_1^* h_1}{\left|\hat{h}_1\right|} + \frac{\hat{h}_2^* h_2}{\left|\hat{h}_2\right|} \right) x + noise. \tag{5}$$

If we want to pre-code on only one Tx, e.g. Tx-2, then we can transmit x at Tx1 and $\hat{h}_1 \hat{h}_2^* x / |\hat{h}_1 \hat{h}_2|$ at Tx2 ($\hat{h}_i \neq 0$), and the received signal is

$$y = \left(h_1 + \frac{\hat{h}_1 \hat{h}_2^* h_2}{\left|\hat{h}_1 \hat{h}_2\right|} \right) x + noise. \tag{6}$$

Both (5) and (6) have the same received power over the subcarrier.

Different from SFBC, BF does not need decoding at the receiver. Instead, it needs the feedback of CSI from the receiver to the transmitters to establish pre-coding.

2.3 Gains of MMW CoMP

By using CoMP, either SFBC or BF, we essentially raise the channel capacity by adding more uncorrelated links, decrease error rate by improving SNR performance, and improve the stability of SNR by reducing variation. In the analysis of traditional HF wireless communications, microwave propagation is usually modeled as Rayleigh, Rician, or Nakagami fading channels [65, 66]. However, the channels in MMW small cells, especially the ones with directional beams, are completely different as a result of the characteristics of MMW propagation. Therefore, whether coordination gains exist, and how significant they are, are both questions to discuss. In this section, we theoretically derive gains from MMW CoMP transmission.

Since only 2×1 CoMP can achieve rate-one by SFBC [67], we use the 2×1 model shown in Fig. 4 to estimate gains that a MMW CoMP system can attain in both SFBC and BF modes. Some assumptions and facts are listed as follows for theoretical analysis.

1) Each of the two links is considered as an additive white Gaussian noise (AWGN) channel and the noise at the receiver side dominates.
2) Only LoS link can successfully communicate. Links are sensitive to obstacles in MMW propagation, and any NLoS scenario drops the throughput to zero.
3) No multipath effect is considered as directional transmission and high reflection loss in MMW frequencies. The coherent bandwidth of MMW wireless channels is much wider than signal bandwidths.
4) The transmitting power at each transmitter is normalized to 1 and the total transmitting power is 2 (this is different from single-cell multi-antenna systems where the total transmitting power is normalized).
5) Signals from two transmitters are well synchronized at the receiver in terms of both time and frequency.

In these assumptions, 1 to 3 are approximations to reality, among which 3 will be verified in the experiment in Section 4.1, 4 is a fact for multi-cell coordination scenarios, and 5 will be discussed in Chapter 3. Considering 2 and 3, the two channels are modeled as independent Bernoullian, i.e.,

$$h_i = a_i \exp(j\varphi_i) \mathrm{B}(1, 1-p) \quad (i=1 \text{ or } 2), \tag{7}$$

where $a_i > 0$ is the attenuation and $0 < \varphi_i < 2\pi$ is the phase of channel i, regardless of frequency within the signal band, and $0 < p < 1$ is the probability of NLoS (zero throughput) in each channel.

2.3.1 Single-point transmission

2.3.1.1 SNR

When there is only one of the two transmitters, Tx-i (i=1 or 2), transmitting with normalized power, the received SNR is

$$SNR_i = \frac{|h_i|^2}{N} = \begin{cases} 0 & \text{with NLoS probability of } p \\ a_i^2/N & \text{with LoS probability of } 1-p \end{cases}, \tag{8}$$

where N is the noise power at the receiver. Let us denote the LoS SNR as

$$\rho_i = a_i^2/N \tag{9}$$

for the following analysis.

2.3.1.2 Average capacity

To derive the capacity, the signal is assumed to be Gaussian. Without doing multi-point transmission, the average capacity (in bit/s/Hz) for single-point transmission over the link from Tx-i to Rx is

$$\begin{aligned} C_i &= \Pr(\mathrm{LoS}) \cdot C_{LoS}(\rho_i) \\ &= (1-p)\log_2(1+\rho_i), \end{aligned} \tag{10}$$

where $\Pr(\cdot)$ is the probability of an event, $C_{LoS}(\rho_i) = \log_2(1+\rho_i)$ is the LoS channel capacity as a function of LoS SNR.

2.3.1.3 BER performance

In LoS single-point transmission, for 16-QAM OFDM as an example, the bit error rate (BER) is approximately

$$P_{b,LoS}(\rho_i) = \frac{3}{4} Q\left(\sqrt{\frac{\rho_i}{5}}\right) - \frac{9}{16} Q^2\left(\sqrt{\frac{\rho_i}{5}}\right), \tag{11}$$

where $Q(\cdot)$ is the complimentary error function [68]. If LoS is not guaranteed and lost bits are counted as errors, the average BER is

$$\begin{aligned} P_b(\rho_i) &= \Pr(\text{NLoS}) \cdot 1 + \Pr(\text{LoS}) \cdot P_{b,LoS}(\rho_i) \\ &= p + (1-p) P_{b,LoS}(\rho_i), \end{aligned} \tag{12}$$

which has an error floor of p.

2.3.1.4 Stability of SNR

The coefficient of variation (CV) of SNR is used to measure the (un)stability of transmission [69]. For single-point transmission, from (8), the expectation of the received SNR from Tx-i is

$$\mathrm{E}(SNR_i) = (1-p)\rho_i \,. \tag{13}$$

The standard deviation of this SNR is

$$\begin{aligned} \sigma(SNR_i) &= \sigma\left(|h_i|^2 / N\right) \\ &= \frac{1}{N} \sqrt{\mathrm{Var}\left(|h_i|^2\right)} \\ &= \frac{1}{N} \sqrt{p(1-p) a_i^{\,4}} \\ &= \rho_i \sqrt{p(1-p)} \,, \end{aligned} \tag{14}$$

where $\mathrm{Var}(\cdot)$ is the variance of a random variable. Then the CV of SNR is

$$\mu(p) = \frac{\sigma(SNR_i)}{\mathrm{E}(SNR_i)} = \sqrt{\frac{p}{1-p}} \,. \tag{15}$$

2.3.2 Gains in SFBC mode

By doing 2×1 CoMP transmission, we increase the SNR, the capacity, the BER performance, and the stability by combining two channels. In the following, we will analyze the gains in both SFBC and BF modes with respect to the single-point transmission analysis above.

Based on assumption 3, from each transmitter, the two adjacent subcarriers in a coding block experience the same channel response. Therefore, the transfer function of (2) can be rewritten as

$$\begin{pmatrix} y_L \\ y_R^* \end{pmatrix} = \mathbf{HX} + \mathbf{N} = \begin{pmatrix} h_1 & -h_2 \\ h_2^* & h_1^* \end{pmatrix} \begin{pmatrix} x_1 \\ x_2^* \end{pmatrix} + \mathbf{N}. \tag{16}$$

Since the transmitting power from each transmitter is normalized to 1, x_i has power of $1/n_c$, where n_c is the number of OFDM subcarriers. Also, since the power of the noise at the receiver is N, the power of $\mathbf{N}$ is $2N/n_c$.

2.3.2.1 SNR

Still assuming the transmitting power is 1 at each transmitter and the noise power at the receiver is N, from (16), the received SNR is

$$SNR_{SFBC} = \frac{|h_1|^2 + |h_2|^2}{N} = \begin{cases} 0 & \text{with probability of } p^2 \\ \rho_1 & \text{with probability of } p(1-p) \\ \rho_2 & \text{with probability of } p(1-p), \\ \rho_{SFBC} & \text{with probability of } (1-p)^2 \end{cases} \tag{17}$$

where

$$\rho_{SFBC} = \frac{a_1^{\,2} + a_2^{\,2}}{N} = \rho_1 + \rho_2 \tag{18}$$

is the SNR at the receiver when both links are LoS.

2.3.2.2 Average capacity

To derive the capacity, the signal is assumed to be Gaussian. With all the assumptions aforementioned, the average capacity for SFBC mode is

$$\begin{aligned} C_{SFBC} &= \Pr(\text{both NLoS}) \cdot 0 \\ &\quad + \Pr(\text{Tx1 LoS \& Tx2 NLoS}) \cdot C_{LoS}(\rho_1) \\ &\quad + \Pr(\text{Tx1 NLoS \& Tx2 LoS}) \cdot C_{LoS}(\rho_1) \\ &\quad + \Pr(\text{both LoS}) \cdot C_{LoS}(\rho_{SFBC}) \\ &= p(1-p)\log_2(1+\rho_1) + p(1-p)\log_2(1+\rho_2) \\ &\quad + (1-p)^2 \log_2(1+\rho_1+\rho_2). \end{aligned} \tag{19}$$

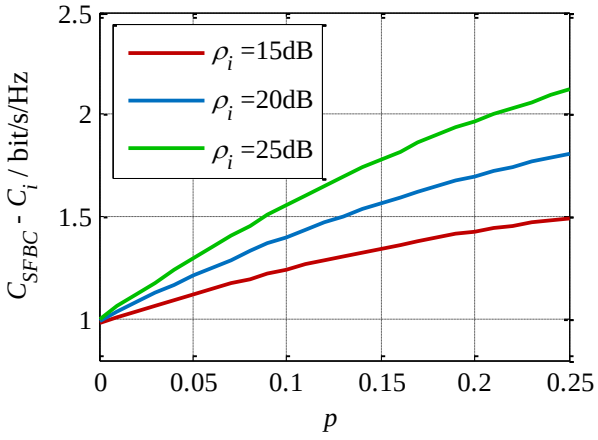

(a)

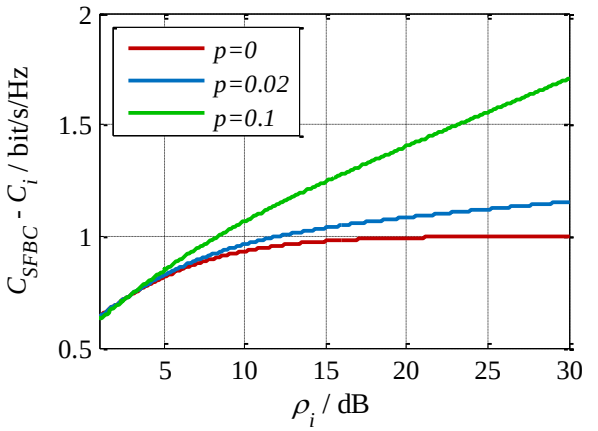

(b)

Fig. 5. Average capacity gain (in bit/s/Hz) versus (a) NLoS probabilities and (b) LoS SNR.

By subtracting (10) from (19), we get the capacity gain of using SFBC mode. As an example, when the two transmitters have the same transmitting power and the two channels are i.i.d., the two single-point transmission links have the same expression, i.e. $\rho_1 = \rho_2$ and $C_1 = C_2$. In this case, Fig. 5 shows the average capacity gain, i.e. $C_{SFBC} - C_i$, as a function of p and ρ_i.

In large ρ_i and zero p region, SFBC mode has an approx. 1-bit/s/Hz gain attributed to the 3-dB SNR gain of CoMP transmission. This gain increases when NLoS probability gets larger. This is due to the higher probability of receiving the signal via either one of the two paths.

2.3.2.3 BER performance

By using CoMP transmission, we improve the performance by having SNR gains and reducing the error floor caused by NLoS shadowing. For SFBC mode and 16-QAM OFDM, the average BER is

$$\begin{aligned} P_{b,SFBC}(\rho_1,\rho_2) &= \Pr(\text{both NLoS})\cdot 1 \\ &\quad + \Pr(\text{Tx1 LoS \& Tx2 NLoS})\cdot P_{b,LoS}(\rho_1) \\ &\quad + \Pr(\text{Tx1 NLoS \& Tx2 LoS})\cdot P_{b,LoS}(\rho_2) \\ &\quad + \Pr(\text{both LoS})\cdot P_{b,LoS}(\rho_{SFBC}) \\ &= p^2 + p(1-p)\left(P_{b,LoS}(\rho_1)+P_{b,LoS}(\rho_2)\right) \\ &\quad + (1-p)^2 P_{b,LoS}(\rho_1+\rho_2)\ , \end{aligned} \tag{20}$$

which has an error floor of p^2.

As an example, when ρ_2 is fixed to 15 dB, Fig. 6 shows the BER as a function of ρ_1. From the curves we can see that SFBC mode has lower BER with respect to single-point transmission. When $p \neq 0$, the error floor in SFBC mode is twice lower (in dB) than the case in single-point transmission.

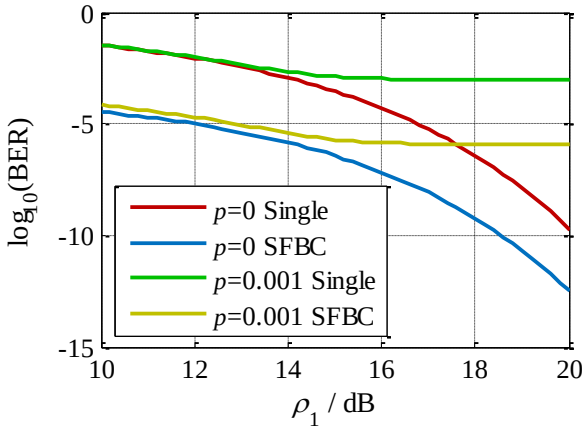

Fig. 6. BER versus ρ_1 for single-point transmission and SFBC mode at different NLoS probabilities when ρ_2 = 15 dB.

2.3.2.4 Stability of SNR

In the following we show that by using CoMP transmission and under the assumptions above, the CV of SNR can be reduced so that stability can be improved compared with single-point transmission.

From (17), we have

$$\mathrm{E}(SNR_{SFBC}) = (1-p)\rho_1 + (1-p)\rho_2 = (1-p)(\rho_1+\rho_2), \tag{21}$$

and

$$\begin{aligned}\sigma(SNR_{SFBC}) &= \sigma\left(|h_1|^2/N + |h_2|^2/N\right) \\ &= \frac{1}{N}\sqrt{\mathrm{Var}\left(|h_1|^2 + |h_2|^2\right)}.\end{aligned} \tag{22}$$

Because the two links are independent, we have

$$\begin{aligned}\sigma(SNR_{SFBC}) &= \frac{1}{N}\sqrt{\mathrm{Var}\left(|h_1|^2\right) + \mathrm{Var}\left(|h_2|^2\right)} \\ &= \frac{1}{N}\sqrt{p(1-p)a_1^{\,4} + p(1-p)a_2^{\,4}} \\ &= \sqrt{p(1-p)}\sqrt{\rho_1^{\,2} + \rho_2^{\,2}}\,.\end{aligned} \tag{23}$$

Then, we have

$$\mu_{SFBC}(p;\rho_1,\rho_2) = \frac{\sigma(SNR_{SFBC})}{\mathrm{E}(SNR_{SFBC})} = \sqrt{\frac{p}{1-p}}\,\frac{\sqrt{\rho_1^2+\rho_2^2}}{\rho_1+\rho_2} = \frac{\sqrt{\rho_1^2+\rho_2^2}}{\rho_1+\rho_2}\,\mu(p)\ , \tag{24}$$

and from the coefficient in (24) we can see that for any p, $\mu_{SFBC}(p;\rho_1,\rho_2)$ is always smaller than $\mu(p)$ as ρ_1, $\rho_2 > 0$, which means SFBC mode always has smaller CV than single-point transmission for given p. Also, the coefficient is independent of p or whether power is normalized.

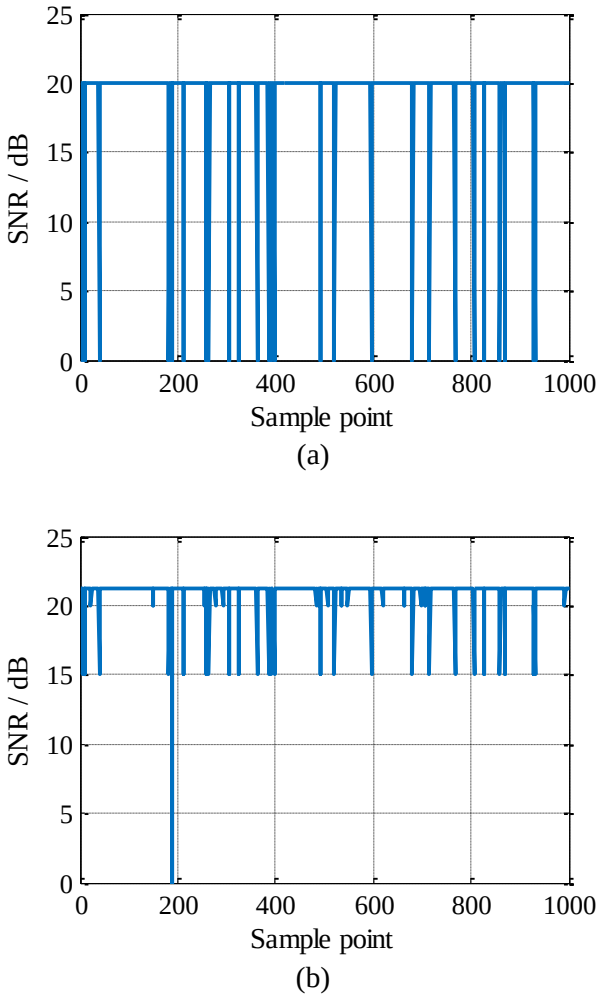

Fig. 7. Variation of received SNR in (a) single-point transmission and (b) SFBC mode.

In Fig. 7, we give a simulation example to demonstrate the variation of received SNR when ρ_1 = 20 dB, ρ_2 = 15 dB, and p = 0.02. When Tx1 transmits singly, the SNR has large variation and completely loses signals very frequently, as shown in Fig. 7(a). On the other hand, when we use SFBC mode, the SNR variation is mostly limited within a small range and the signal is dropped at only one sample point out of 1,000 total points, as shown in Fig. 7(b).

2.3.3 Gains in BF mode

2.3.3.1 SNR

From (5) and (6), assuming the power at each transmitter is 1 and the noise power at the receiver is N, the received SNR is

$$SNR_{BF} = \frac{\left(|h_1| + |h_2|\right)^2}{N} = \begin{cases} 0 & \text{with probability of } p^2 \\ \rho_1 & \text{with probability of } p(1-p) \\ \rho_2 & \text{with probability of } p(1-p), \\ \rho_{BF} & \text{with probability of } (1-p)^2 \end{cases} \tag{25}$$

where

$$\rho_{BF} = \frac{\left(a_1 + a_2\right)^2}{N} = \rho_1 + \rho_2 + 2\sqrt{\rho_1 \rho_2} \tag{26}$$

is the SNR at the receiver when both links are LoS.

2.3.3.2 Average capacity

To derive the capacity, the signal is assumed to be Gaussian. With all the assumptions aforementioned, the average capacity for BF mode is

$$\begin{aligned} C_{BF} = {} & p(1-p)\log_2(1+\rho_1) + p(1-p)\log_2(1+\rho_2) \\ & + (1-p)^2 \log_2\left(1+\rho_1+\rho_2+2\sqrt{\rho_1\rho_2}\right). \end{aligned} \tag{27}$$

The derivation of (27) is similar to that of (19). By subtracting (10) from (27), we get the capacity gain of using BF transmission. As an example, when the two transmitters have

the same transmitting power and the two channels are i.i.d., the two single-point transmission have the same expression, i.e. $\rho_1 = \rho_2$ and $C_1 = C_2$, and (27) is simplified to

$$C_{BF} = 2p(1-p)\log_2(1+\rho_i) + (1-p)^2 \log_2(1+4\rho_i). \tag{28}$$

In this case, Fig. 8 shows the average capacity gain, i.e. $C_{BF} - C_i$, as a function of p and ρ_i.

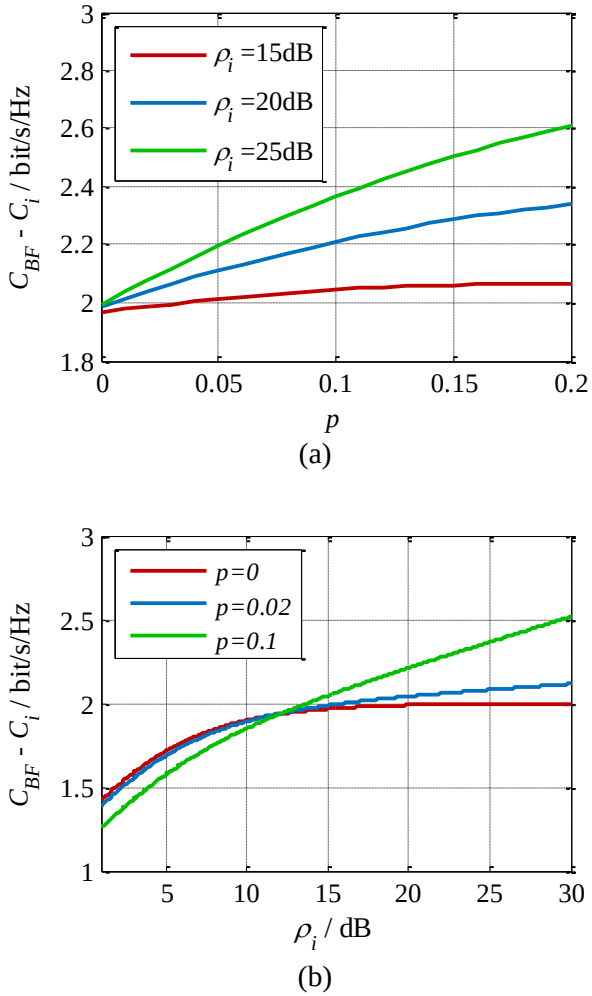

Fig. 8. Average capacity gain (in bit/s/Hz) versus (a) NLoS probabilities and (b) LoS SNR.

In large ρ_i and zero p region, CoMP transmission has an approx. 2-bit/s/Hz gain attributed to the 6-dB SNR gain of CoMP transmission. This gain increases when NLoS

probability gets larger. This is due to the higher probability of receiving the signal via either one of the two paths.

2.3.3.3 BER performance

For BF mode and 16-QAM OFDM, similar to (20), the average BER is

$$P_{b,BF}(\rho_1,\rho_2) = p^2 + p(1-p)\left(P_{b,\mathrm{LoS}}(\rho_1) + P_{b,LoS}(\rho_2)\right) + (1-p)^2 P_{b,LoS}\left(\rho_1 + \rho_2 + 2\sqrt{\rho_1\rho_2}\right), \quad (29)$$

which has an error floor of p^2.

As an example, when ρ_2 is fixed to 15 dB, Fig. 9 shows the BER as a function of ρ_1. From the curves we can see that BF mode has lower BER with respect to single-point transmission. When $p \neq 0$, the error floor in BF mode is twice lower (in dB) than the case in single-point transmission.

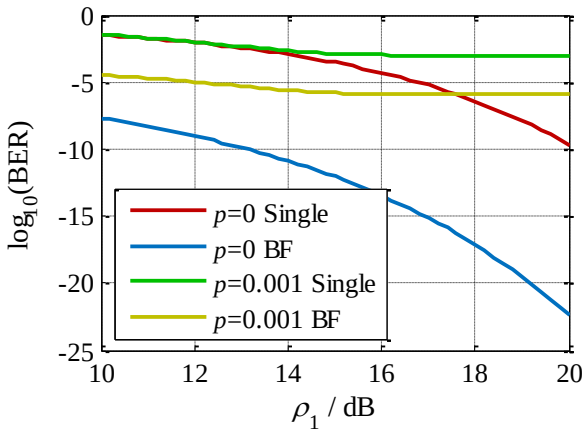

Fig. 9. BER versus ρ_1 for single-point transmission and BF mode at different NLoS probabilities when ρ_2 = 15 dB.

2.3.3.4 Stability of SNR

In Fig. 10, we use the same simulation example as in 2.3.2.4 to demonstrate the variation of received SNR when ρ_1 = 20 dB, ρ_2 = 15 dB, and p = 0.02. When we use BF mode, the SNR variation is mostly limited within a small range and the signal is dropped

at only one sample point out of 1,000 total points, compared with single-point transmission shown in Fig. 7(a).

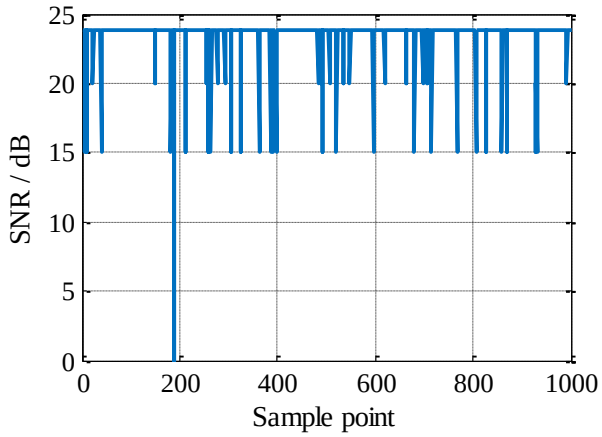

Fig. 10. Variation of received SNR in BF mode.

2.4 Challenges of MMW CoMP

2.4.1 Frequent feedback for beamforming

From the analysis above, we can see that BF has higher gain than SFBC mode. However, it does not imply that we always prefer BF mode to SFBC mode in every scenario. Other than the gains, a main difference between the two modes is that the transmitters need feedback from the receiver to estimate the channel for BF coding, which SFBC does not need. The variation of the channel over time determines how often we need to pass the feedback from the receiver to the transmitters. On the one hand, the coherent time in MMW systems is usually much larger than the one in HF systems because of the directional beam and high propagation loss. On the other hand, the short wavelength of MMW determines that the channel phases, which are the key information for channel estimation and directly determine the performance of BF, are very sensitive to the relative movement between the transmitters and the receiver. As a result, for a

MMW mobile network, the relative movement defines the upper bound of feedback period.

A worse case that we have to take into consideration is when the receiver is located in the middle of two transmitters with equal power and moving toward one of the transmitters. In this case, the SNR gain from BF as a function of time is

$$\gamma = 2 + 2\cos\left(4\pi vft / c\right), \tag{30}$$

where v is the velocity of the receiver, f is the MMW frequency, and c is the speed of light. Based on this relationship, Fig. 11 shows how often we need to send feedback for BF precoding in a 60-GHz system in order to maintain a required SNR gain when the receiver has a peak velocity of 1 m/s [70]. From the figure we can see that the criterion is to send feedback at least every 0.83 ms. Lower than this rate will cause the BF being inferior to single-point transmission. Therefore, choosing between BF and SFBC is not only about signal gain, but also the specific implementation of the bi-directional system.

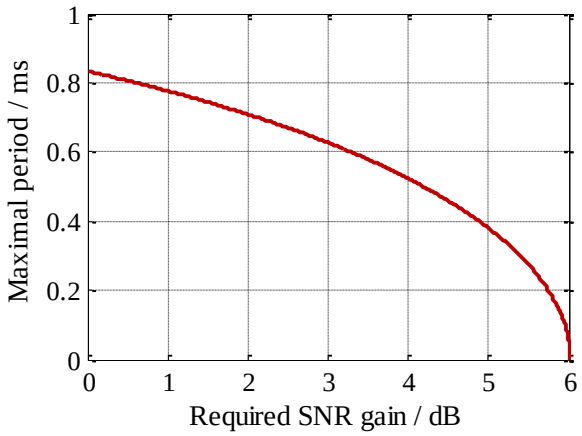

Fig. 11. Maximal period of sending feedback vs. required SNR gain of BF in a 60-GHz system with peak receiver velocity of 1 m/s.

2.4.2 Overhead traffic for joint processing in CoMP

As mentioned in Chapter 1, CoMP in a traditional distributed RANs involves communications across backhaul or midhaul and requires precise cooperation. It generates significant overhead traffic to enable CoMP, especially JP, and also imposes stringent requirements on capacity, delay, and synchronizations over backhaul/midhaul [15]. This is the common problem for CoMP operating at any frequency. In HF CoMP on 10-MHz LTE-A, the coordination generates overhead traffic over the X2 logical links by up to 4 Gb/s with latency requirement of 1 ms and is mainly accomplished in a digital and distributed manner. Considering the bandwidth of MMW communications may go up to multi-GHz, the overhead consumption for MMW CoMP will consequently go incredibly high. The high carrier frequency of MMW CoMP will also make the requirement of delay and synchronization more stringent.

In addition, the wiring between MMW small cells can be locally organized or user-deployed. In a worse case, some of the MMW coverage may come from a home network through a HGW. The coordination between these MMW small cells and other cells that are provided by operators may have to go across networks belonging to different services, if coordination is expected. All these unpredictable facts of backhauling in distribute MMW CoMP tell us that we have to minimize the overhead traffic or bring up new backhauling solutions.

2.4.3 Distributed generation of MMW

MMW circuits are costly to design and have low power efficiency [71]. The application of CoMP requires the MMW transmitters have more stable and identical performance than what a single-point communication system requires. With each distributed transmitter generating its own MMW frequency in a densified network, the system has low power and infrastructure efficiency and the downlink CoMP transmission suffers from the inconsistent MMW frequencies.

2.4.4 Asynchronization

In Section 2.3, we have assumed that the CoMP signals are well synchronized, which is the precondition to have the gains. However, in practical systems, the synchronization is not always guaranteed. Free-running transmitters or transmitters that are not perfectly synchronized will have timing offset (TO), carrier frequency offset (CFO), and sampling frequency offset (SFO). In uplink these offsets can be compensated and leave little impairment while in downlink the compensation is extremely difficult as the dimension of receivers is lower than the one of transmitters.

In downlink CoMP transmission, TO contributes to both the relative group delay and the relative carrier phase shift between the signals from different transmitters and therefore leads to power fading. Because of the high frequency, the fading in MMW CoMP is more sensitive to TO compared with HF CoMP.

CFO and SFO both contribute to inter-subcarrier interference of the OFDM signals in downlink CoMP transmission. In existing eNBs, the carrier frequency and the sampling clock are derived from the same frequency source [72], and thus CFO and SFO have the same error source. In MMW CoMP, CFO has much larger impact than SFO since the carrier frequency is much larger than the signal bandwidth.

In fact, synchronization is considered as the most critical issue in MMW CoMP and also the main motivation to propose the concept of centralized MMW CoMP in this dissertation. Therefore, in Chapter 3, we will use the whole chapter to analyze this issue in MMW CoMP.

CHAPTER 3 SYNCHRONIZATION IN MMW CoMP

In this chapter, we will study the importance of synchronization in downlink MMW CoMP transmission, in other words, how asynchronization between the two CoMP transmitters may affect the downlink reception of MMW OFDM signals in the model of Fig. 4. Both SFBC and BF modes are included, and both CFO and TO between the two transmitters are considered.

3.1 Synchronization in SFBC Mode

SFBC is designed to be immune from the common phase difference between the CoMP signals. However, CFO and TO cause other issue such as inter-subcarrier interference and loss of orthogonality that impair the decoding of SFBC.

3.1.1 Simulation

We first look at some simulation results for SFBC mode. We assume the two MMW transmitters have the same power, the noise at the receiver dominates, and SNR is defined as the ratio between the signal power received from *each* transmitter and the noise power from the receiver.

Fig. 12 shows the simulation result of how CFO may affect the CoMP transmission in SFBC mode in terms of the error vector magnitude (EVM) of a signal with 15-kHz subcarrier spacing. ZF decoding is used here. The EVM increases linearly as the CFO does and has a slope of 9%/kHz.

Although we cannot detect this impairment until the two coordinated signals are received at the receiver, we can treat this impairment as an inherent one from the transmitter side. To meet the 12.5% EVM requirement (16-QAM) on the transmitter side [73], we need to limit the CFO below 1.4 kHz. Although the result in Fig. 12 is regardless

of carrier frequency, the 1.4-kHz CFO criterion corresponds to a 23ppb error if we use 60 GHz as the carrier frequency. To maintain such a low frequency error for such a high carrier frequency is both challenging and costly for current MMW circuits and generation solutions. Let alone we always need some margin for the CFO, considering the noise and distortion from the transmitter side.

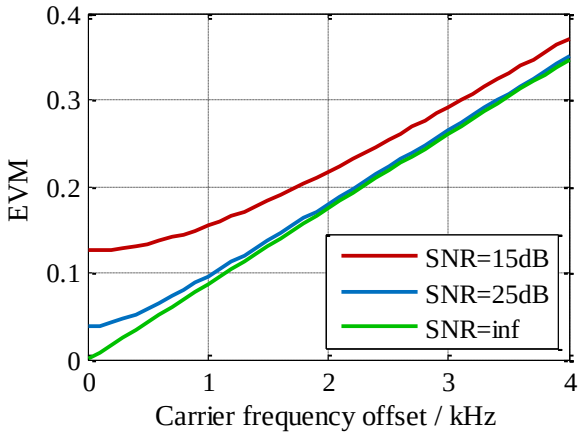

Fig. 12. EVM vs. CFO under different SNR values in SFBC mode with 15-kHz subcarrier spacing regardless of bandwidth or carrier frequency.

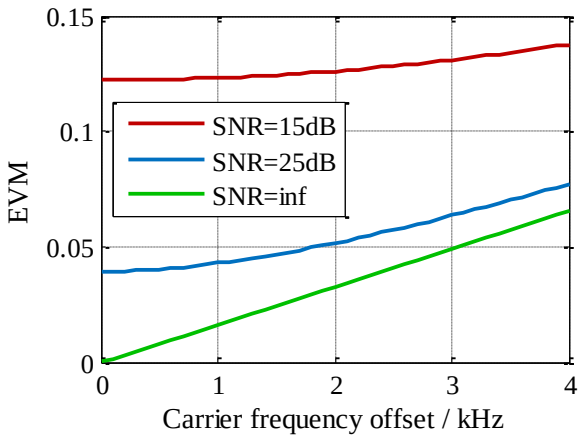

Fig. 13. EVM vs. CFO under different SNR values in SFBC mode with 75-kHz subcarrier spacing regardless of bandwidth or carrier frequency.

Of course, we may relieve this requirement on MMW frequency error by increasing the subcarrier spacing. Fig. 13 shows the CFO effect when the signal has a subcarrier spacing of 75 kHz [74]. Proportionally, the slope of the CFO-EVM curve is 1/5 of the one that 15-kHz subcarrier spacing is applied. However, this does not mean that we can simply increase the subcarrier spacing of OFDM signals for the sake of CoMP. On the one hand, as we have seen, large subcarrier spacing has proportionally large tolerance against CFO. On the other hand, subcarrier spacing is also inversely proportional to the duration of each OFDM symbol which has proportional contribution to the robustness against TO.

TO between the two CoMP signals may cause inter-symbol interference (ISI) at the receiver. To avoid ISI, cyclic prefix (CP) is added on each OFDM symbol. Although we also use CP to combat ISI caused by multipath effect and dispersion in single-point OFDM transmission and getting rid of CP is also feasible if we do inter-symbol processing [75], the CP in multi-point transmission is more significant and getting rid of it is less recommended as the impairment caused by ISI is more difficult or even impossible to mitigate in multi-point transmission. Therefore, the CP length has to be larger than the TO to avoid ISI, and as such, the maximal efficiency we can achieve is

$$\frac{\text{symbol duration}}{\text{symbol duration} + \text{TO}} \tag{31}$$

or

$$\frac{1}{1 + \text{TO} \times \text{subcarrier spacing}}, \tag{32}$$

which agrees with our statement above that subcarrier spacing cannot be arbitrarily large.

ISI is not the only concern of TO in SFBC. Even if the CP is large enough to avoid ISI, TO still has impact on the coordination as it destructs the orthogonality provided by SFBC. This loss of orthogonality causes two consequences.

Firstly, to provide an accurate estimate of the matrix including the linear phase shift caused by TO, one more of the entries in matrix (4) will become independent from others, and as such, more overhead will be needed for channel estimation. Ignoring this phase shift and keeping the old matrix will cause dramatic EVM increase even if the TO is only several nanoseconds. Fig. 14 shows the impact from TO after ZF decoding with only the compensation of common phase difference but without any estimation of the linear phase shift. Note that the CP length is sufficiently larger than the TO.

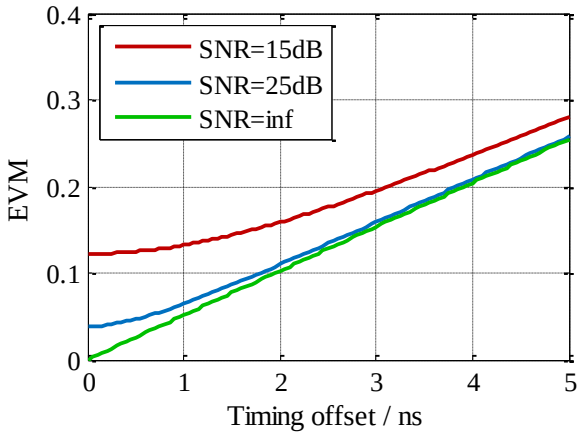

Fig. 14. EVM vs. TO under different SNR values in SFBC mode with 15-kHz subcarrier spacing and 20-MHz bandwidth, after common phase difference removed but without estimation of linear phase shift, regardless of carrier frequency.

Secondly, certain TO may lead to a large condition number of the matrix **H** in (2). The increase of condition number causes poor tolerance to noise during SFBC decoding even if the linear phase shift is considered. Fig. 15 shows the impact of TO after ZF decoding with a perfect estimate of the matrix including the linear phase shift terms. Note that the CP length is sufficiently larger than the TO. In a microsecond level of TO, the noise enlargement from the loss of orthogonality is severe over certain TO regions where the matrix has large condition numbers.

Comparing Fig. 14 and Fig. 15, we increase the tolerance to TO from a nanosecond level to a microsecond level by including the phase shift in the estimate and achieve error free transmission when there is no noise, which implies that the extra overhead and phase shift estimation are critical to overcome TO.

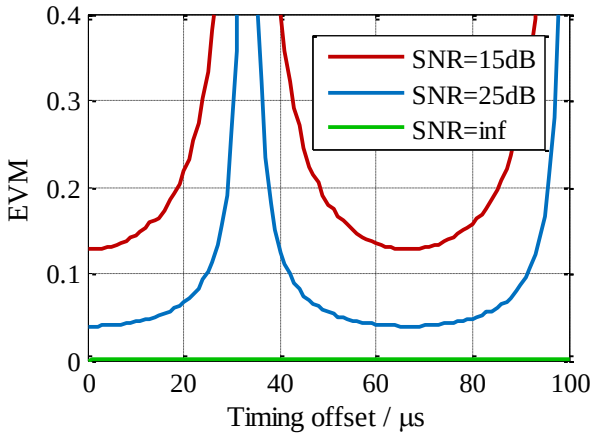

Fig. 15. EVM vs. TO under different SNR values in SFBC mode with 15-kHz subcarrier spacing and with estimation of phase shifts, regardless of bandwidth or carrier frequency.

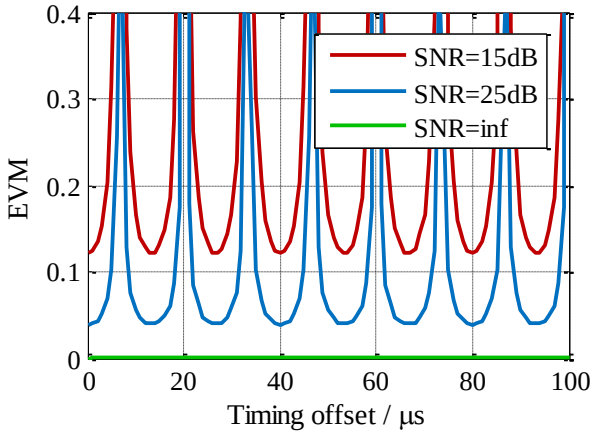

Fig. 16. EVM vs. TO under different SNR values in SFBC mode with 75-kHz subcarrier spacing and with estimation of phase shifts, regardless of bandwidth or carrier frequency.

Because TO is linear phase shift over frequency domain, increasing the subcarrier spacing causes higher sensitivity to TO and more dramatic change of condition number. As shown in Fig. 16, by increasing the subcarrier spacing from 15 kHz to 75 kHz, we have a four times higher incidence of an infinitely large condition number which leads to large EVM.

To further see the relationship between the condition number of the channel matrix and the EVM fluctuation, we have the condition number-versus-TO curves in Fig. 17. Both the cases of 15-kHz and 75-kHz subcarrier spacing match the trend in Fig. 15 and Fig. 16 and thus imply that the TO should be limited within a few microseconds to maintain a low condition number.

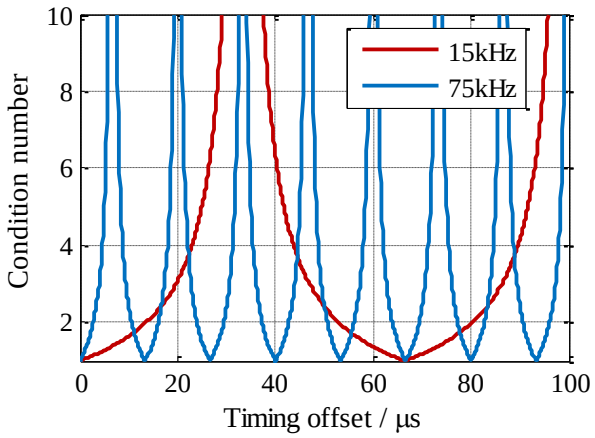

Fig. 17. Condition number of channel matrix vs. TO under different subcarrier spacing, regardless of bandwidth or carrier frequency.

3.1.2 Experimental analysis

In this section, we will further experimentally verify the conclusions that we just derived from the simulation analysis. In the testing, the subcarrier spacing is 15 kHz and the bandwidth of the 60-GHz OFDM signal is 20 MHz. The CP length is long enough to avoid ISI.

In Fig. 18, we give the EVM-versus-CFO curves. The significant rise of EVM over a few kHz reveals the high sensitivity of CoMP transmission to CFOs, although the slope is different from the one in Fig. 12 because of the practical testbed imperfection.

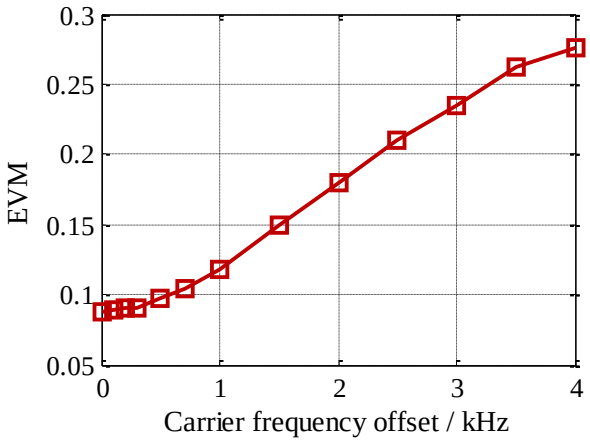

Fig. 18. EVM vs. CFO tested in SFBC mode with 15-kHz subcarrier spacing.

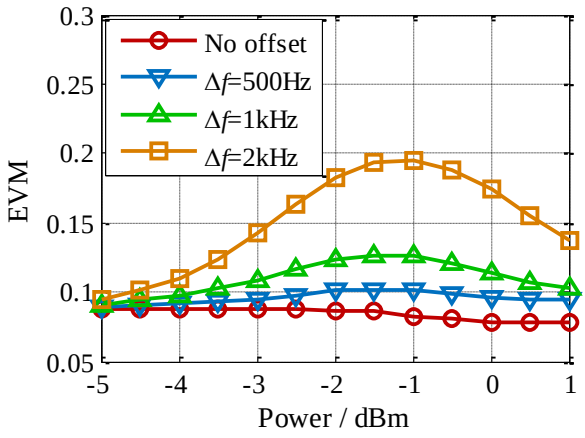

Fig. 19. EVM vs. power tested under different CFO (Δf) in SFBC mode with 15-kHz subcarrier spacing.

Fig. 19 gives the EVM-versus-power curves under different CFOs. As we change power at one of the two transmitters, a certain CFO has the strongest impact on EVM

when the two transmitters have balanced power and has less impact when the two transmitters have larger power difference.

In Fig. 20 we give the EVM-versus-TO curves. 25% CP is added which is equivalent to 16.7 μs. The significant rise of EVM over a few μs reveals the high sensitivity of CoMP transmission to TO.

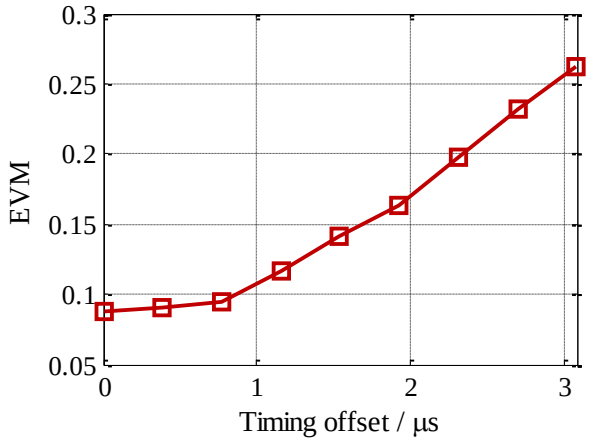

Fig. 20. EVM vs. TO tested in SFBC mode with 15-kHz subcarrier spacing.

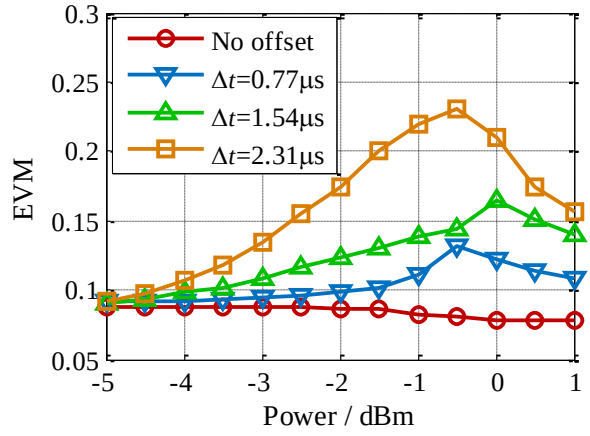

Fig. 21. EVM vs. power tested under different TO (Δt) in SFBC mode with 15-kHz subcarrier spacing.

Fig. 21 gives the EVM-versus-power curves under different time offsets. As we change power at one of the two transmitters, a certain offset has the strongest impact on EVM when the two transmitters have balanced power and has less impact when the transmitters have larger power difference.

3.2 Synchronization in BF Mode

In this section we look at some simulation results showing the importance of synchronization in BF mode. We still assume the two MMW transmitters have the same power, the noise at the receiver dominates, and SNR is defined as the ratio between the signal power received from *each* transmitter and the noise power from the receiver.

In BF, CFO changes the phase relationship between the two transmitters. For a CFO of Δf, the two transmitters have to update their carrier phases in every $1/2\Delta f$ at least before they become completely out-of-phase and cancel each other. Correspondingly, the system has to embed overheads for feedback in its uplink in every $1/2\Delta f$. Considering a 10ppb error of a 60-GHz oscillator, this requires a feedback at least every 0.8 ms, which can generate unnecessary overhead and require further synchronization and delay. Nevertheless, to maintain an intended BF gain, we have to send feedback in a much higher rate. Fig. 22 shows the relationship between required SNR gain and the maximal interval of sending feedback for channel estimation. Note that this relationship is regardless of the modulation format or the MMW carrier frequency of the signal. The OFDM symbol period has to be sufficiently smaller than the feedback period (i.e. the subcarrier spacing be sufficiently larger than the CFO).

Even if we use large subcarrier spacing and enough overhead to keep the two transmitters close to in-phase, CFO can still cause signal degradation through inter-subcarrier interference. Fig. 23 shows the simulation result of how CFO may affect the BF mode in terms of the EVM of a signal with 15-kHz subcarrier spacing. The EVM increases linearly as the CFO does and has a slope of 6%/kHz. To meet the 12.5% EVM

requirement (16-QAM) at the transmitter side, we need to limit the CFO below 2 kHz, corresponding to a 33ppb error of the 60-GHz carrier frequency. Considering that the simulation range of 4 kHz is well below 15 kHz, the combination of the two OFDM symbols is mainly in the in-phase region. Therefore, the degradation is mainly contributed by inter-subcarrier interference rather than out-of-phase cancellation.

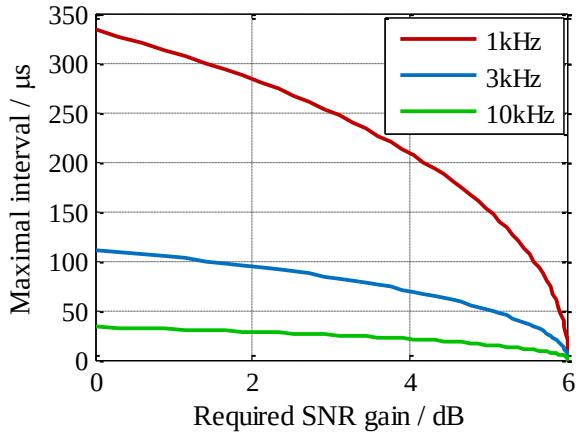

Fig. 22. Maximal interval of sending feedback vs. required SNR gain in BF mode with different CFO between two transmitters, regardless of bandwidth or carrier frequency.

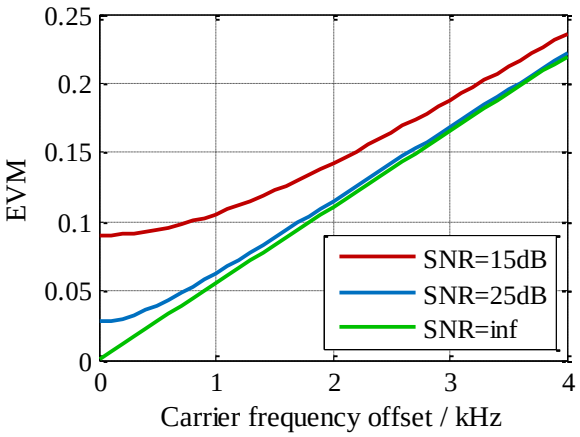

Fig. 23. EVM vs. CFO under different SNR values in BF mode with 15-kHz subcarrier spacing, regardless of bandwidth or carrier frequency.

Fig. 24 shows the CFO effect when the signal has a subcarrier spacing of 75 kHz. Proportionally, the slope of CFO-EVM curve is 1/5 of the one that 15-kHz subcarrier spacing is applied, attributed to lower inter-subcarrier interference and higher SNR from in-phase constructiveness of shorter OFDM symbols.

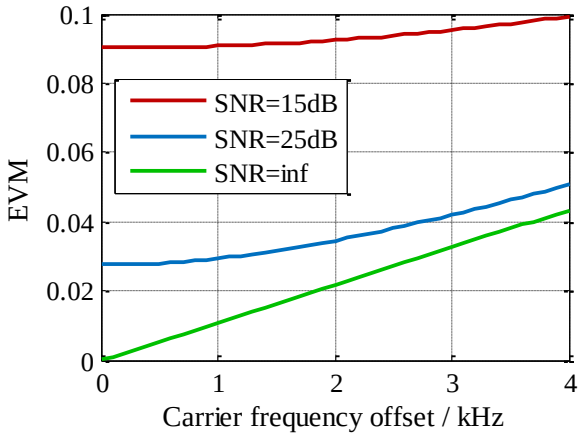

Fig. 24. EVM vs. CFO under different SNR values in BF mode with 75-kHz subcarrier spacing, regardless of bandwidth or carrier frequency.

TO attributes to both phase delay and group delay, corresponding to common phase shift on carrier frequency and linear phase shift on in-band signal, respectively. On account of the short MMW carrier period, this TO requirement for an in-phase relationship contributing to the common phase shift is extremely small in BF mode, in the level of picosecond. Assuming the in-phase relationship is guaranteed by the BF and modulation mechanism and only linear phase shift exists, Fig. 25 shows the impact of this linear phase shift. For a 20-MHz bandwidth, the TO has to be less than 4 ns to meet the EVM requirement, which is challenging. The TO acts similarly to a multipath effect which causes frequency-selective fading. By doing frequency-domain equalization (FDE) at the receiver, we can mitigate this impairment. As shown in Fig. 26, we can relieve the TO requirement after FDE and achieve error free transmission when there is no noise. However, the nanosecond-level requirement is still stringent in practice.

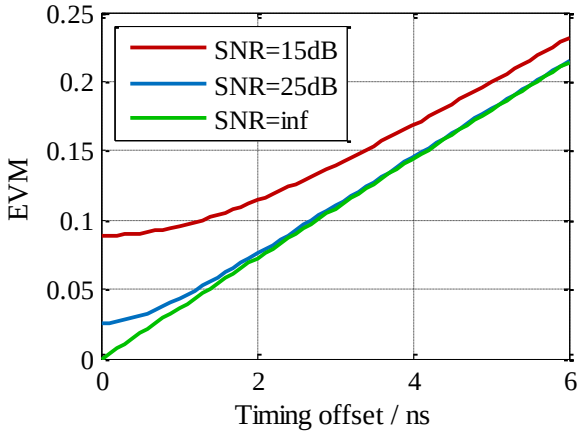

Fig. 25. EVM vs. TO under different SNR values in BF mode with 20-MHz bandwidth after common phase difference removed but without FDE, regardless of subcarrier spacing or carrier frequency.

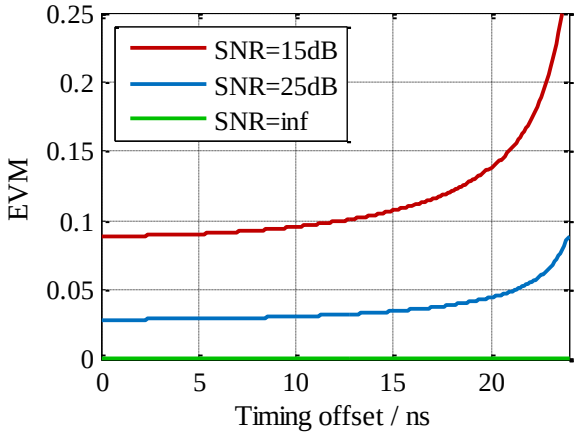

Fig. 26. EVM vs. TO under different SNR values in BF mode with 20-MHz bandwidth after common phase difference removed and FDE, regardless of subcarrier spacing or carrier frequency.

3.3 Current Techniques for Synchronization

Synchronization is critical in both SFBC and BF modes. To provide synchronization between MMW CoMP transmitters, we can refer to current technologies in LTE eNBs. In LTE-A CoMP, the requirement on clock error is lower than 50 ppb in frequency and 500 ns in time according to the specification [72, 76]. In most eNBs, global navigation satellite system (GNSS), e.g. global positioning system (GPS), is used

as the primary reference source (priority may differ by FDD and TDD). When GNSS signals fail, the system may switch to packet-based network synchronization mechanisms such as synchronous Ethernet (SyncE). When all synchronization sources fail, the system will fall back to local clock source to provide holdover with requirements to achieve target holdover specifications [77].

GPS signal receivers used in GNSS disciplined oscillators are not off-the-shelf GPS chips [78]. They require expensive antennas, high-quality holdover oscillators, and their delicate installation and tuning, costing several thousands of dollars [76]. In addition, this approach does not apply to small cells that are designed for indoor communications or for where GNSS signal cannot be received. In fact, indoor radio access is a very important application of MMW frequencies. Therefore, using GNSS as an external synchronization reference is not a practical solution for MMW CoMP.

Packet-based network synchronization methods include SyncE from ITU, precision time protocol (PTP) from IEEE, and network time protocol (NTP) from IETF [79, 80, 81]. The maximum errors in SyncE and NTP are 4.6 and 15 ppm, respectively [82, 81]. These errors are larger than the requirement from our analysis. Furthermore, these reference signals are delivered from the backhaul. Regardless of the backhaul consumption which is inefficient, the baseband frequency in the backhaul is much lower than the MMW frequency. Up-conversion to MMW frequencies adds noise and burden to the succeeding frequency multiplication circuits.

A straightforward way is to use local high-quality frequency source to provide frequency and clock information. Off-the-shelf quartz crystal oscillators working at MHz frequencies have frequency error ranging from 5 ppm to 100 ppm [83]. According to our analysis aforementioned, the CFO has to be in the level of several ppb, much lower than what an off-the-shelf crystal oscillators oscillator can support, to achieve a low EVM in MMW CoMP. Let alone temperature sensitivity and aging are the two major problems for crystal oscillators to maintain the error level. Better than crystal oscillators, atomic

oscillators can provide a much lower error level. Rubidium clocks are widely used in holdover oscillators in current LTE eNBs [84]. However, they are too heavy and costly to be implemented in small-cell applications. What is worse, much larger error, manufacture difficulty, vulnerability, and higher cost will be observed in MMW frequency sources to reach merely the same precision level as HF oscillators.

An alternative way other than to synchronize is to rely on digital signal processing (DSP) techniques that estimate and compensate asynchronizations. In this case, the UE estimates the CFO and TO from the received downlink CoMP signals. Since the receiver dimension is smaller than the transmitter dimension, it is unlikely to correct the offset from the UE side without severe degradation [13]. Instead, the UE has to send feedback to the eNBs, so that the compensation is then fulfilled by the transmitters. In multi-antenna transmission, using constant-amplitude zero-autocorrelation (CAZAC) sequence can estimate CFO [85]. However, most of these CAZAC-based methods need large training sequences [86]. Blind equalization is also proposed, but with tedious computation [87]. The equalization also occupies resources with signal degradation. Considering the potential CFO in MMW bands can be larger than the one in HF bands, the CFO compensation will become challenging. The high sensitivity to TO in MMW CoMP also raises the standard of TO compensation outcome.

In summary, current technologies for synchronization in HF CoMP have their limitations. Introducing them into MMW CoMP cannot be effective solutions.

3.4 Conclusions

Both SFBC and BF modes are sensitive to CFO and TO. To maintain a high-quality coordination, the frequency error of the MMW radio source has to be as low as several ppb and the timing error of the clock has to be as low as nanoseconds. In addition, CP has to be added to avoid ISI, which reduce the efficiency. There are some parameters that determine the vulnerability of the coordination against CFO and TO, including

carrier frequency, bandwidth, and subcarrier spacing. The former two are defined by the service and application. For subcarrier spacing, on the one hand, we want it to be large to reduce inter-subcarrier interference and to reduce OFDM symbol duration. On the other hand, we want subcarrier spacing to be small to provide higher CP efficiency and lower condition number. It is difficult to optimize these parameters, and doing so provides very limited improvement. Therefore, synchronization in both frequency and time should be guaranteed for MMW CoMP. However, current technologies for synchronization in HF CoMP have their limitations. Adopting them into MMW CoMP is not an effective solution.

CHAPTER 4 CENTRALIZATION FOR MMW CoMP

The conclusions from Chapter 3 tell us that we have to provide precise synchronization for MMW CoMP in a new effective approach. A straightforward thinking is to let coordinated transmitters share the same signaling resource providing identical time and frequency information. Noting that those coordinated transmitters belong to different cells and are physically separated as multi-point, the only option to do so is to shift the functionality of the transmitters to a centralized location. In Section 1.2, we have introduced fiber-wireless centralization and RoF. In this chapter, we will study and experimentally examine the performance of RoF links as the realization of fiber-wireless centralization. Then we will theoretically and experimentally validate the feasibility of MMW CoMP as the benefited of fiber-wireless centralization. At last we will conclude that centralization is not only an effective solution for the synchronization problem, but also other problems stated in Section 2.4.

4.1 Fiber-Wireless Centralization

RoF is a solution for full fiber-wireless centralization. As shown in Fig. 27, at the upstream end of a RoF system, the CO centralizes all baseband processing and radio signal modulation for all RAUs. These RAUs share the same timing clock and the same frequency source at the CO which guarantee the synchronization and coherency between RAUs doing downlink CoMP transmission. Also as a result of the centralization and all-analog transmission over fiber links, no baseband or digital processing exists between the CO and UE for both uplink and downlink. This further simplifies the function of RAUs. Besides cost and management savings, this simplification leads to an important property that the propagation delay is only determined by the RoF length. For example, a UE that

is 1 km away from the CO and covered by a small cell with 2-km RoF fronthaul (including 1 km of detour) has a fixed time offset of 6.7 μs without any jitter. This is a promising improvement from traditional distributed systems where digital processing causes variable delays. Most importantly, in a RoF system, latencies are predictable, stable, and easily compensable at the CO so that precise time synchronization can be guaranteed for both uplink and downlink CoMP transmission, even if the RAUs doing CoMP transmission experience very different RoF link lengths.

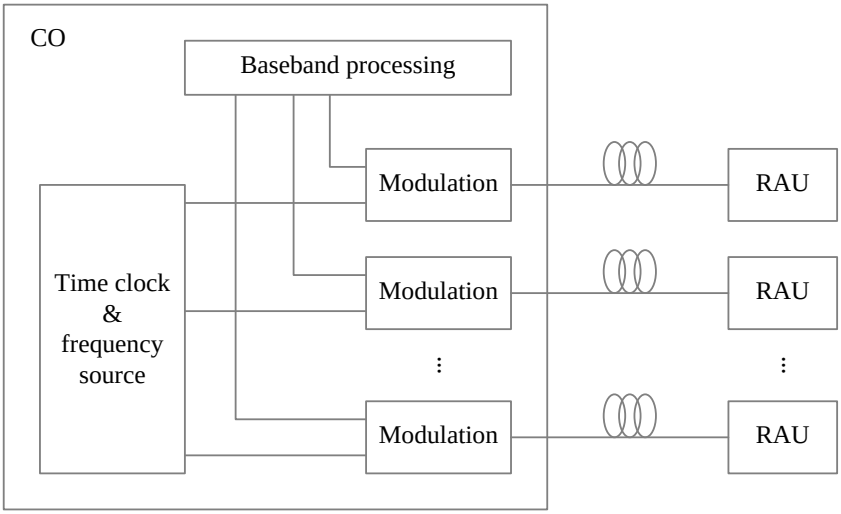

Fig. 27. RoF system for full fiber-wireless centralization.

4.1.1 RoF links

To better understand the functionality of RoF for fiber-wireless centralization, some RoF links are abstracted in Fig. 28 with the relative locations of elements between CO and RAUs. Schematic spectra for corresponding links are also attached at the bottom. Three types of RoF links are included, a MMW RoF link for our following study on centralized MMW CoMP, a multi-section RoF link introduced for the CoMP method proposed in Section 5.2, and a more typical HF RoF link as a reference and for comparison.

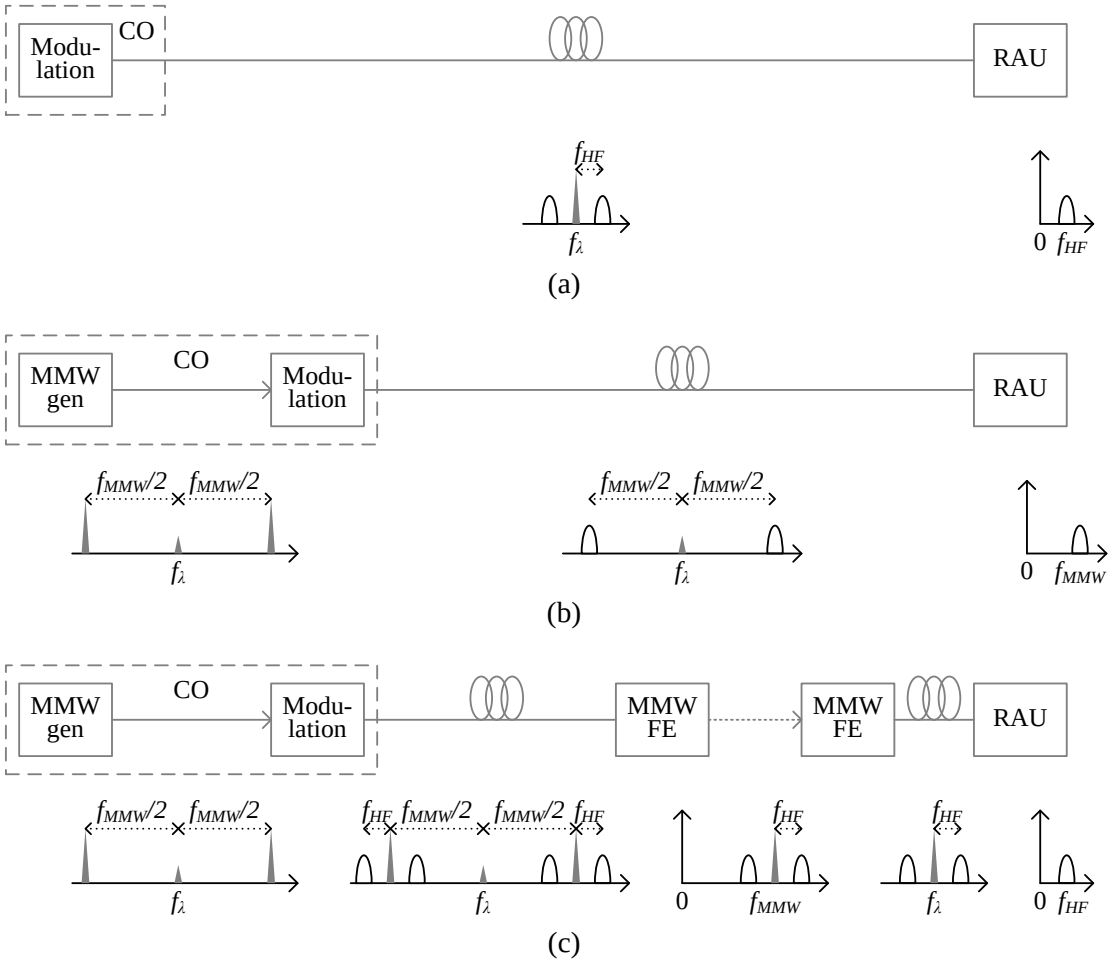

Fig. 28. Downlink and corresponding spectra of (a) HF RoF link, (b) MMW RoF link, and multi-section RoF link.

HF RoF link is the most straight-forward form of a fiber-wireless system with high level of complexity centralization and RAU simplicity. In a HF RoF link, HF signals with a frequency of f_{HF} are carried by a lightwave with a frequency of f_λ, as shown in Fig. 28(a), and directly detected at the RAU to recover HF signals. The whole optical system including modulation, demodulation, and fiber propagation can be seen as transparent in terms of the delivery of HF signals. For uplink, reverse procedure is followed.

In a MMW RoF link, as shown in Fig. 28(b), the MMW carrier is generated by an optical MMW generation module at the CO. By using microwave photonics (MWP), there are various methods to generate MMW carriers in a fiber-wireless system, including

methods based on optical nonlinear effects, methods based on external modulation and filtering, and methods based on optical subcarrier multiplexing (OSCM) [88]. Optical nonlinear affects, such as four-wave mixing (FWM), usually need high-power optical source and precise criteria. Therefore, their feasibility is limited in practical small cell applications. In Table III we list three methods that are mostly used. Among them, OSCM has the simplest setup when the system does not have branch links or require the coherency between RAUs. Optical carrier suppression (OCS) and optical frequency comb (OFC) are both external modulation methods. Compared with OSCM, OCS and OFC can better maintain the coherency of optical MMW carriers and therefore allow better MMW CoMP. In the following parts of this proposal, we will adopt OFC as the MMW generation method because it has higher modulation stability than OCS. Details of OFC are introduced in [88].

Table III. Optical MMW generation in a fiber-wireless system

	OSCM	OCS	OFC
Laser source per MMW	2	1	1
Optical modulation	Not needed	Intensity	Phase
Optical filtering	Not needed	Not needed	Interleaver preferred
Microwave source	Not needed	Half of MMW freq	Depends on filtering
MMW phase noise	Laser linewidth	Microwave phase noise	Microwave phase noise
Carrier-to-noise ratio	Good	Modulation index and bias	Filtering
Stability	Good	Bias drifting	Good
MMW coherency	No	Yes	Yes

After the optical MMW carrier is generated, the signal is applied onto the carrier either in baseband or in a band-mapping scheme to enable multiple services simultaneously carried over MMW bands [89]. Over the MMW RoF section close to the

CO's side, optical MMW frequency $f_\lambda \pm f_{MMW}/2$ is generated to carry the signal, as shown in Fig. 28(b). At the RAU, downlink optical signals are photo-detected to f_{MMW} for wireless transmission. In uplink, the MMW signal from UE is either carried onto lightwave as-is or after down-converted to an intermediate frequency (IF).

A multi-section RoF link meets environmental requirement in urban areas as continuous wiring between the CO and cell sites sometimes can be impossible or cost-prohibit. At the same time, it maintains a centralized structure and all-analog transmission consisting of MMW RoF, MMW wireless, and HF RoF sections, as shown in Fig. 28(c). From UEs' view, a multi-section RoF link is no different from a HF RoF link and is also transparent to HF signals though it involves multiple sections and MMW frequency conversions. Over the MMW RoF section close to the CO's side, optical MMW frequency $f_\lambda \pm f_{MMW}/2$ is generated to carry HF signals. At the MMW wireless frontend (FE), downlink optical signals are photo-detected to f_{MMW} for wireless transmission. After the MMW wireless transmission, HF signals are extracted from received MMW signals and optically modulated for HF RoF transmission. Then the following process is the same as in a HF RoF link. It is also worth noting that multiple RAUs can be supported by the high bandwidth of RoF and MMW transmission though only one RAU is demonstrated here for simplicity. For uplink, the two RoF sections function as HF RoF links while the MMW wireless section up-converts the uplink signal to f_{MMW} by using either electrical circuits or MWP approaches at the transmitting MMW FE and down-convert to HF or baseband at the other FE.

4.1.2 Experimental setup and results

End-to-end downlink transmissions over the three types of RoF links are experimentally demonstrated in this section. The setup consists of a CO, a HF RoF link connecting RAU1, a multi-section RoF link connecting RAU2, a MMW RoF link connecting RAU3, and a set of UE, as shown in Fig. 29.

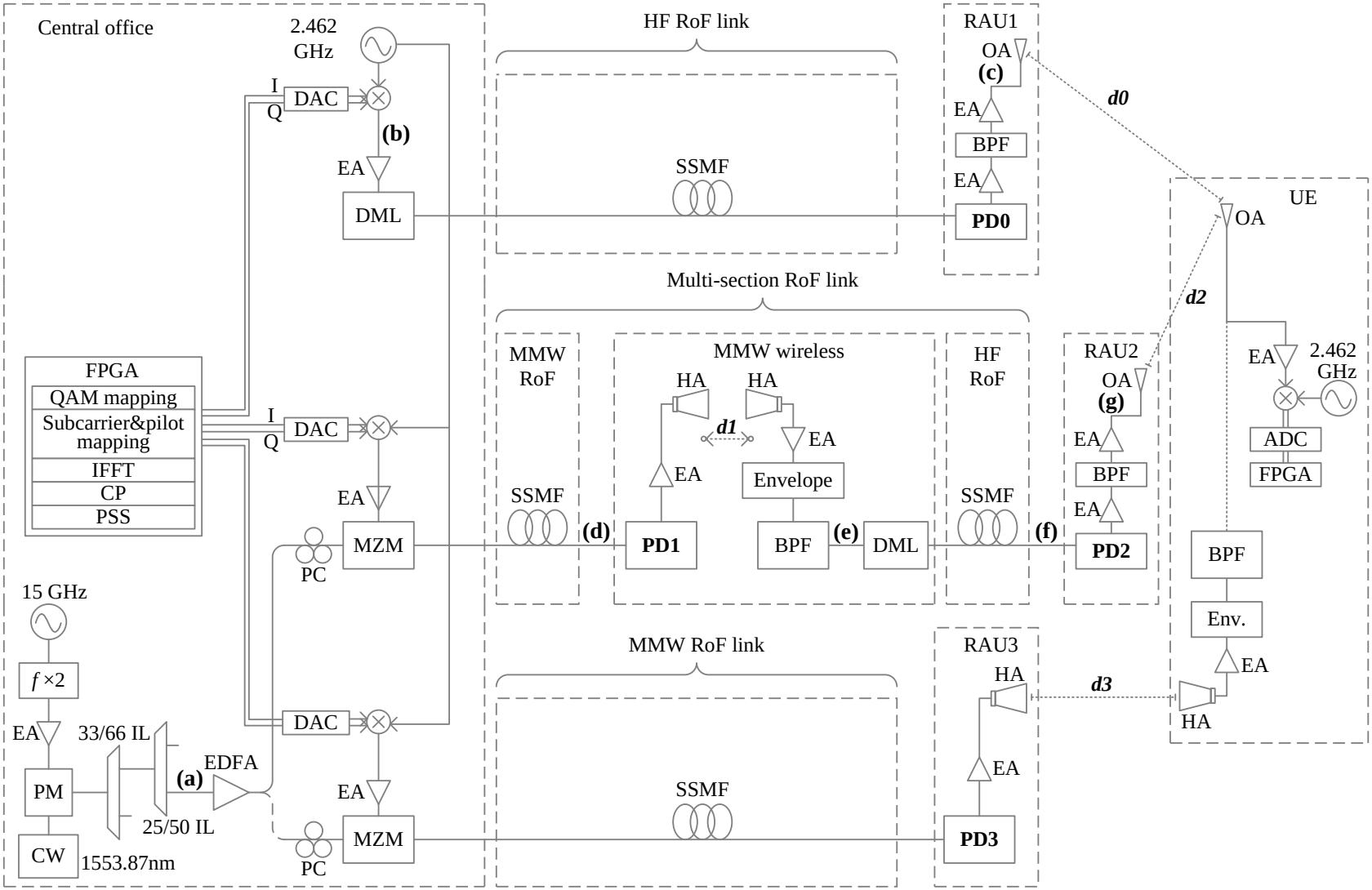

Fig. 29. Experimental setup of downlink transmission over centralized RoF links.

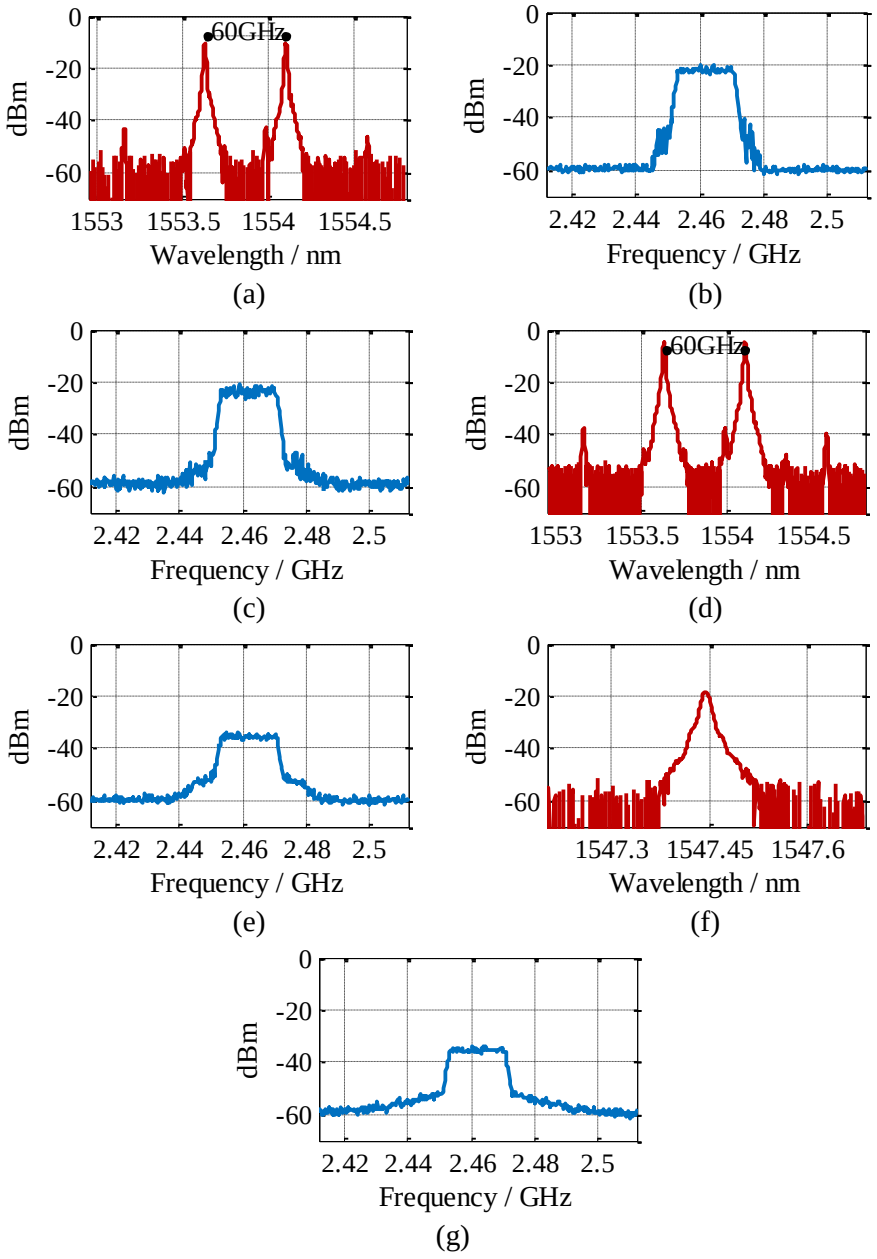

Fig. 30. Optical and electrical spectra at different measured points as labelled in Fig. 29.

4.1.2.1 Central office

The CO centralizes all baseband processing and shared signaling functions. LTE-U signals are generated by a Vertex FPGA chip, digital-to-analog converters (DAC), and up-converters. The FPGA used for the generation of base-band LTE-A signals establishes

real-time 16-QAM mapping and OFDM modulation. The OFDM signals follow the format of LTE-A -- a 20-MHz bandwidth, 1,200 subcarriers with spacing of 15 kHz, 200 out of 1,200 subcarriers set as pilots, an IFFT/FFT size of 2,048, 512 CP points (extended CP mode), and 60 OFDM symbols as a half frame with the 6th used as a primary synchronization symbol (PSS). After DACs and shared frequency up-conversion, the LTE-U signals have a central frequency of 2.462 GHz (IEEE 802.11 WLAN channel 11). The LTE-U signals are modulated onto lightwave and transmitted through different RoF links.

Another function of the CO is to generate shared optical MMW carriers. As shown in Fig. 29, an optical signal from a continuous-wave (CW) distributed feedback (DFB) laser at a wavelength of 1,553.87 nm is applied to a 40-GHz phase modulator (PM). The PM is driven by a 30-GHz tone, which is double the 15-GHz microwave source, creating MMW combs. After passing two inter-leavers (ILs) of 33/66 GHz and 25/50 GHz, a 60-GHz optical MMW carrier whose optical spectrum is plotted in Fig. 30(a) is formed. This MMW carrier generation procedure is the OFC method mentioned in 4.1.1. After amplification by an erbium doped fiber amplifier (EDFA), the optical MMW carrier is fed into Mach-Zehnder modulators (MZMs) to be intensity-modulated by the LTE-U signals for different RoF links.

4.1.2.2 HF RoF link

The first RoF structure we setup is the HF RoF link. The LTE-U signal whose electrical spectrum is shown in Fig. 30(b) is carried onto lightwave by using a directly modulated laser (DML) after an electrical amplifier (EA). The DML has fixed output power of 6 dBm.

The lightwave signal is transmitted for 20 km over a standard single mode fiber (SSMF). At RAU1, the LTE-U signal is detected by a 2.5-GHz photo detector (PD), filtered by a band-pass filter (BPF), and amplified by a low-noise amplifier and a power

amplifier. The spectrum of the signal before the antenna is shown in Fig. 30(c). A pair of 3-dBi omnidirectional antennas (OAs) is used for wireless transmissions. The wireless distance between RAU1 and UE is noted as *d0* and subject to change.

4.1.2.3 Multi-section RoF link

The multi-section RoF link shown in Fig. 29 consists of a MMW RoF section, a MMW wireless section, and a HF RoF section over the link. After intensity modulation (IM) at the CO, the optical MMW carrier carrying the LTE-U signal is launched into the multi-section RoF link. After MMW RoF transmission over a curl of 15-km SSMF, the measured optical spectrum is plotted in Fig. 30(d). For MMW wireless transmission, the signal is detected by a 60-GHz PD, amplified by an EA, and then radiated by a V-band horn antenna (HA) with a 15-dBi gain and a 24° half-power beamwidth. The MMW wireless distance between the HA pair is noted as *d1* and subject to change. The received MMW signal is amplified and down-converted to the 2.462-GHz band by using a 60-GHz envelope detector. After a BPF the HF signal whose spectrum is plotted in Fig. 30(e) drives a DML, which has fixed output power of 6 dBm and a wavelength of 1,547.44 nm.

The succeeding link including RAU2 has the same setup as in HF RoF link. The measured optical spectrum after HF RoF transmission over 5-km SSMF is plotted in Fig. 30(f). The electrical spectrum before the OA of RAU2 is plotted in Fig. 30(g), and the wireless distance between RAU2 and UE is noted as *d2* and subject to change.

4.1.2.4 MMW RoF link

The third RoF structure in the setup is a MMW RoF link that provides a MMW small-cell coverage. The link setup along with RAU3 has the same configuration as the MMW RoF section and the transmitter side of the MMW wireless section in the multi-section RoF link. The wireless distance between RAU3 and UE is noted as *d3* and subject to change.

4.1.2.5 User equipment

At the UE side, for HF RoF signals, the UE down-converts the amplified LTE-U signal from 2.462 GHz to baseband. After analog-to-digital converters (ADC), the baseband signal is processed in an FPGA chip, functionally including synchronization, OFDM demodulation, and equalization. Real-time EVM values of equalized symbols are shown in a real-time manner. For MMW RoF signals, a V-band down-converter is used to recover the LTE-U signal from the 60-GHz carrier so that succeeding processing can be carried on in the same way as in HF RoF link. The V-band down-converter has the same setup as the receiver side of the MMW wireless section in the multi-section RoF link.

4.1.2.6 Experimental results

We first use the setup to verify assumption 3 from Section 2.3. The channel characteristics of the end-to-end 60-GHz MMW RoF transmission through RAU3 are estimated as shown by the blue curve in Fig. 31. Flat channels are observed with coherent bandwidth much larger than the signal bandwidth (20 MHz). During the test, the blue curve has negligible variation over time or environmental movement. For comparison, we also give the channel estimate of 2.462-GHz HF RoF transmission through RAU1. As shown by the red curve, different from MMW RoF, obvious frequency-selective fading affects the flatness of the magnitude of subcarriers. Therefore, MMW RoF has flat channel response, which implies the flatness of MMW wireless transmission, i.e. assumption 3.

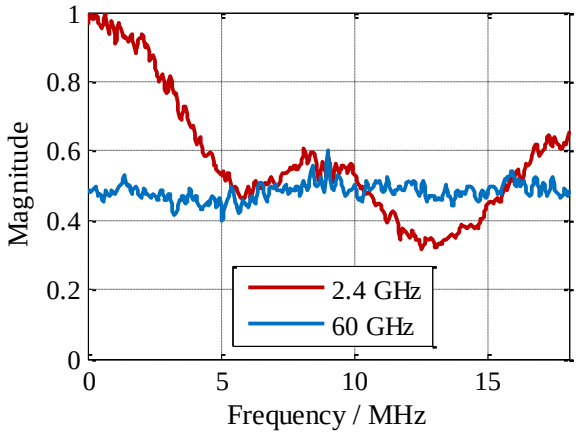

Fig. 31. Channel estimate of 2.462-GHz and 60-GHz band through RAU1 and 3, respectively.

In the following, EVM results are measured from the RoF links, including received-optical-power performance, distance performance, and stability. All results are derived from real-time capture without offline processing.

We first test received-optical-power performance by adding an attenuator and changing optical power before PD0, PD1, PD2, and PD3 separately. For HF RoF link, Fig. 32(a) shows EVM curves under the change of received optical power at PD0. The HF wireless distance is fixed to *d0* = 2 m. As shown in Fig. 32 (a), 20-km fiber transmission induces an approx. 0.3-dB power penalty with respect to back-to-back (BTB) transmission.

For multi-section RoF link, Fig. 32(b) shows EVM curves under the change of received optical power at PD1. The HF wireless distance is fixed to *d2* = 2 m, and the optical power at PD2 is at 2 dBm during the test. As shown in Fig. 32(b), 15-km + 5-km fiber transmission induces an approx. 0.5-dB power penalty with respect to BTB transmission. As the MMW wireless transmission is part of the link, we give results at *d1* = 2.5 m as well as 5 m. In both BTB and 15-km + 5-km fiber transmission, the power penalty caused by doubling *d1* is lower than 0.7 dB, which reveals the feasibility of centralized MMW generation. Similarly, Fig. 32(c) shows EVM curves under the change

of received optical power at PD2. The HF wireless distance is fixed to *d2* = 2 m, and the optical power at PD1 is fixed to 0 dBm during the test. According to the curves, 15-km + 5-km fiber transmission also has an approx. 0.5-dB power penalty with respect to BTB transmission, which is constant with the case in Fig. 32(b). The power penalty caused by doubling MMW wireless distance is approx. 1 dB, which is higher than the case in (b), because of the succeeding HF RoF transmission. Comparing Fig. 32(a) and (c), the MMW parts in multi-section RoF link induce impairment including approx. 1.5-dB and 2-dB power penalties with respect to HF RoF link when *d1* is 2.5 m and 5 m, respectively. These penalties decrease when received optical power at PD0 and PD2 is reduced.

For MMW RoF link, Fig. 32(d) shows EVM curves under the change of received optical power at PD3. The MMW wireless distance is fixed to *d3* = 2.5 m. As shown in Fig. 32(d), 20-km fiber transmission also induces an approx. 0.5-dB power penalty with respect to BTB transmission. By comparing the BTB curves in Fig. 32(b) and (d), we can find that the succeeding link after MMW wireless in multi-section RoF link induces a 0.5-dB power penalty on average with respect to MMW RoF link.

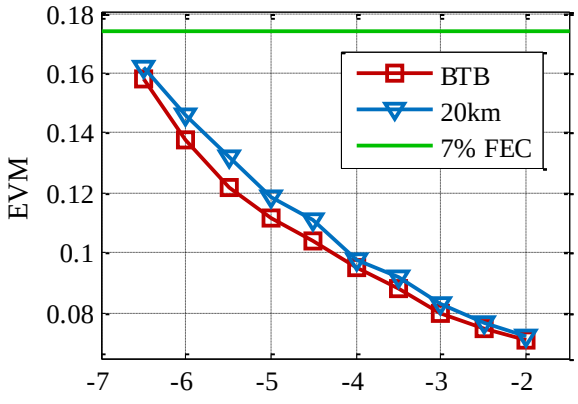

(a)

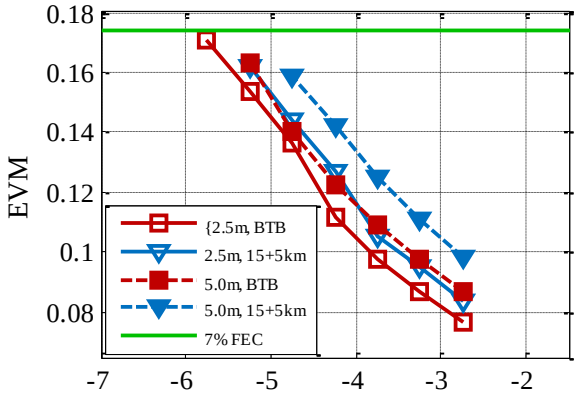
0.18
0.16
0.14
0.12
0.1
0.08
EVM
{2.5m, BTB
2.5m, 15+5km
5.0m, BTB
5.0m, 15+5km
7% FEC
-7
-6
-5
-4
-3
-2
Received Optical Power @ **PD1** / dBm

(b)

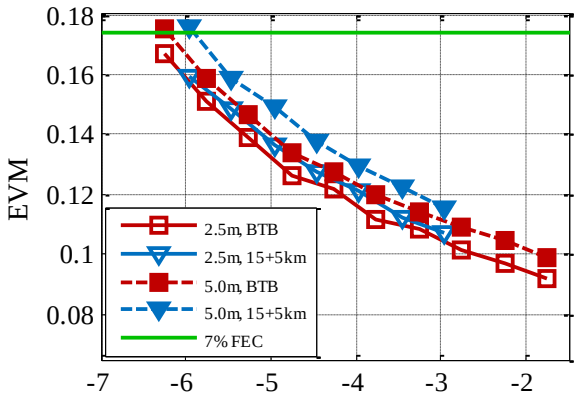
0.18
0.16
0.14
0.12
0.1
0.08
EVM
2.5m, BTB
2.5m, 15+5km
5.0m, BTB
5.0m, 15+5km
7% FEC
-7
-6
-5
-4
-3
-2
Received Optical Power @ **PD2** / dBm

(c)

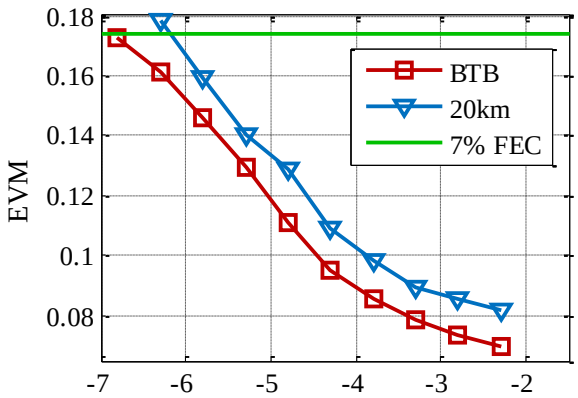
0.18
0.16
0.14
0.12
0.1
0.08
EVM
BTB
20km
7% FEC
-7
-6
-5
-4
-3
-2
Received Optical Power @ **PD3** / dBm

(d)

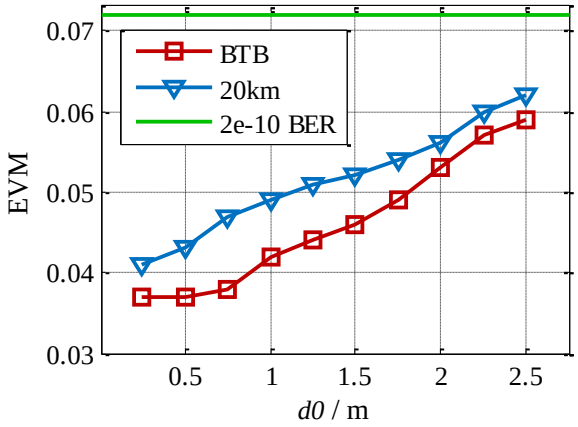
0.07
0.06
0.05
0.04
0.03
EVM
BTB
20km
2e-10 BER
0.5
1
1.5
2
2.5
d0 / m

(e)

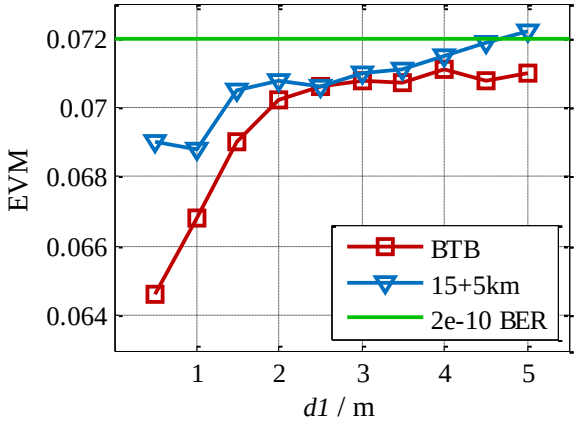
0.072
0.07
0.068
0.066
0.064
EVM
BTB
15+5km
2e-10 BER
1
2
3
4
5
d1 / m

(f)

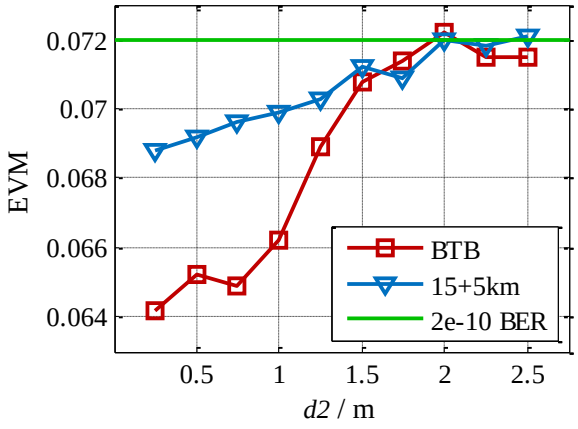
0.072
0.07
0.068
0.066
0.064
EVM
BTB
15+5km
2e-10 BER
0.5
1
1.5
2
2.5
d2 / m

(g)

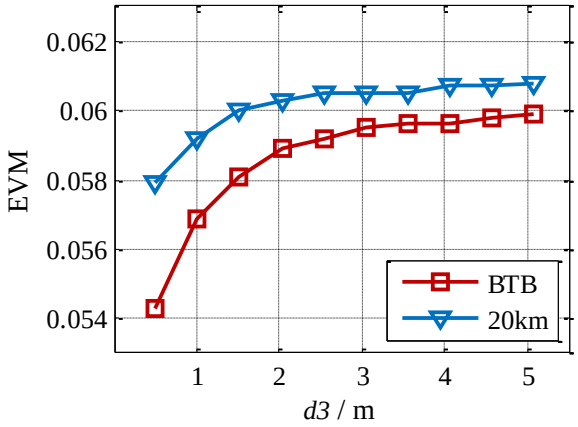

(h)

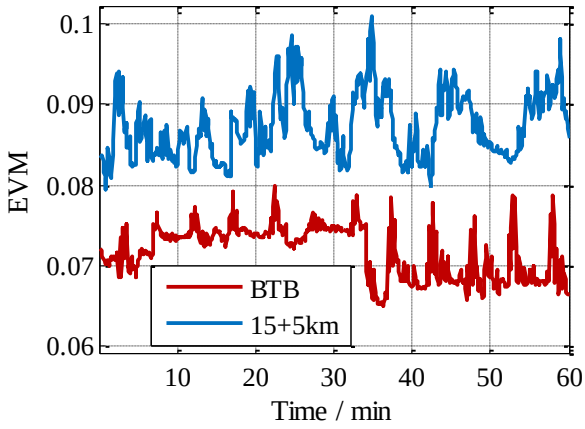

(i)

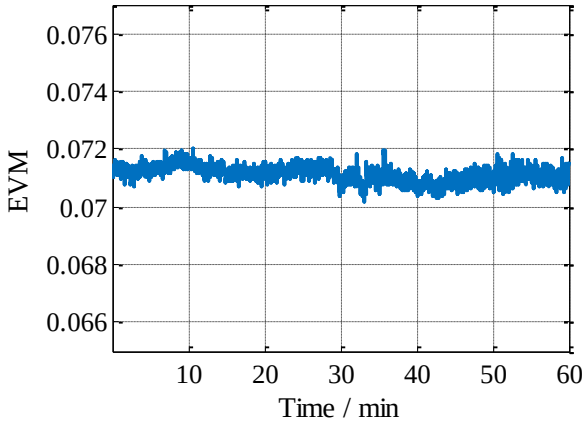

(j)

Fig. 32. Measured EVM values of 16-QAM signals under various received optical power at (a) PD0, (b) PD1, (c) PD2, and (d) PD3, and various wireless transmission distances of (e) *d0*, (f) *d1*, (g) *d2*, and (h) *d3*. Real-time recorded EVM values in a 1-hour long-run test through (i) RAU2 and (j) RAU3.

Secondly, we execute distance tests by changing wireless distances *d0*, *d1*, *d2*, and *d3* separately. EAs in RAUs and UE are optimized at each distance measure point in order to emulate automatic gain control (AGC). EAs in MMW wireless links are only optimized when *d1* is changed. In RAU1 and 2 the highest equivalent isotropically radiated power (EIRP) is limited within 8 dBm.

During the test over *d0*, the received optical power at PD0 is fixed to 2 dBm. As shown in Fig. 32(e), the EVM of 20-km fiber transmission has a 0.01-per-meter slope within the test range. Compared with BTB transmission, 20-km fiber transmission has an EVM penalty less than 0.01 and this penalty decreases as *d0* increases. This reveals the insensitivity of the centralized system to RoF link length.

For the test over *d1* and *d2*, we fix the received optical power to 0 dBm and 2 dBm at PD1 and PD2, respectively. The maximum distance of *d1* we can reach is limited by the laboratory size. As shown in Fig. 32(f), the variation of EVM over a 5-m distance range is within 0.004 for 15-km + 5-km fiber transmission, which reveals the insensitivity of the centralized system to MMW wireless distance change. In Fig. 32(g), similar EVM variation is observed over a HF wireless distance range of 2.5 m. By comparing the BTB curves in Fig. 32(e) and (g), one can notice that MMW parts in multi-section RoF link induce impairment causing EVM penalty from 0.012 to 0.028 over the distance range. This impairment dominates EVM deterioration when HF distance *d2* is small, while HF has higher impact when *d2* increases.

For MMW RoF link, Fig. 32(h) shows that the variation of EVM over a 5-m distance range is within 0.003 for a 20-km fiber transmission and the penalty becomes mild when *d3* is beyond 2 m.

Overall, in most cases shown in Fig. 32(e)-(h), the EVM values are small enough to retain low error rate. We give the EVM level corresponding to 7% forward error correction (FEC) threshold (BER = 3.8×10^{-3}) in the figures as a reference, and most measure points are beneath this level. Furthermore, BTB transmission can get lower

EVM over short distance regions. However, as distances increase, this difference between BTB and fiber transmissions becomes unobservable. This is due to the dominance of wireless transmissions in terms of signal quality deterioration. In addition, according to the trends of curves, HF wireless transmissions are more sensitive to distance change compared with MMW wireless, as a result of omni-directional transmission and limited amplifier power.

Lastly, we examine the stability of the system by recording the instantaneous average EVM value of each OFDM symbol over a continuous 1-hour transmission. For multi-section RoF link, received optical power at PD1 and PD2 is fixed to 0 dBm. The wireless distances are *d1* = 4 m and *d2* = 2 m. Fig. 32(i) plots the recorded EVM values of both BTB and 15-km + 5-km fiber transmission. As one can observe, both transmission scenarios have EVM variation within 0.02. For BTB transmission, the upper and lower bounds of EVM are 0.08 and 0.066, which correspond to BER values of 8.5×10^{-9} and 4.6×10^{-12}, respectively. For 15-km + 5-km fiber transmission, the upper and lower bounds are 0.01 and 0.08, which corresponds to BER values of 2.9×10^{-6} and 8.5×10^{-9}, respectively. The main reasons that cause the fluctuation come from the HF wireless transmission, including interference from WiFi networks, fading caused by environmental movement and multi-paths. To verify, we also give the stability test result for MMW RoF link in Fig. 4(j). Different than multi-section RoF link, the EVM variation is within 0.002 over the whole testing period. This observation somehow also supports assumption 3.

4.2 Fiber-Wireless Centralized MMW CoMP

By realizing centralization based on the MMW RoF link in Section 4.1, we actually change the downlink model in Fig. 4 to a new model as shown in Fig. 33 by adding a section of RoF link as part of the channel. In this section, we will validate the feasibility of downlink MMW CoMP transmission after adding the RoF link. Although

RoF has much larger coherent bandwidth and time, we have to take RoF channel parameters such as delay and dispersion into consideration to see their impact on the performance of MMW CoMP.

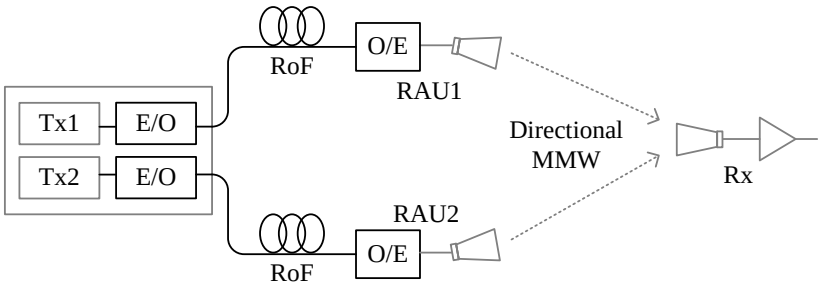

Fig. 33. Centralized downlink 2×1 MMW CoMP transmission model.

In fact, most of the signal variation caused by RoF channel can be mitigated by FDE. The pre-coding and pre-equalization in BF mode have already included this FDE procedure against the wireless transmission. As a result, the RoF channel is transparent in BF mode and cause no essential change on the procedure.

Different from BF, SFBC normally does not have a pre-equalization procedure against the channel response, and it has to guarantee the orthogonality at the receiver. This determines the vulnerability of SFBC to the channel. Adding the RoF link may affect its feasibility. In the following, we will analyze this issue.

In (3), the characteristics of matrix **H** affect the quality of symbol recovery. **H** has to have a condition number as small as possible to tolerate noise. In other words, we hope that the matrix is orthogonal or close to orthogonal. When orthogonality holds, regardless of the estimation error, we can have the gains that we derived in Section 2.3 under the five assumptions. In other words, we need to verify that the RoF link can provide and retain the orthogonality at the receiver.

Firstly, as demonstrated in Section 4.1, the coherent bandwidth of MMW RoF is much larger than the bandwidth of the coded block. With no frequency-selective fading within one coded block, we have $|h_{i,L}| \approx |h_{i,R}|$, or $a_{i,L} \approx a_{i,R}$.

Secondly, we need to consider chromatic dispersion in fiber transmission and relative time delay between two links in terms of phase change. With $a_{i,L} \approx a_{i,R}$, the relationship between $h_{i,L}$ and $h_{i,R}$ can be expressed as

$$h_{i,R} = h_{i,L} \cdot \exp(j\varphi_{CD} + j\varphi_d), \tag{33}$$

where φ_{CD} and φ_d denote phase shifts caused by chromatic dispersion (CD) and relative delay, respectively.

We use LTE-U as an example. Current LTE signals have subcarrier spacing of 15-kHz, and we use a 1,550-nm wavelength for downlink. 17-ps/nm/km dispersion causes a 1.92×10^{-13}-rad/km phase shift factor on average, which implies that φ_{CD} is negligible.

Because of the inherent synchronization of the centralized coordination and the compensable fixed length of fiber links, with regard to the estimation of φ_d, we measure only wireless links. The difference between the lengths of two MMW wireless links contributes to a 3.1×10^{-4}-rad/m (= $2\pi\times15$ kHz / 3×10^8 m/s) phase shift. Typically, this difference is limited by the MMW propagation range that is normally shorter than 10 m for small-cell applications, and thus $\varphi_d < 3.1\times10^{-3}$ rad, which is negligible.

Therefore, (33) approximates $h_{i,R} = h_{i,L} = h_i$, and $\mathbf{H}$ is simplified as

$$\mathbf{H} = \begin{pmatrix} h_1 & h_2 \\ h_2^* & -h_1^* \end{pmatrix}, \tag{34}$$

which has orthogonal complex vectors and hence a constant condition number of 1 when h_1 and h_2 are not both zero. This orthogonality guarantees the recovery of original symbols without enlarged penalty, and therefore an equivalence of (16) that guarantees the gains.

4.3 Experimental Evaluation

In this section we demonstrate a real-time end-to-end 60-GHz experimental setup distributed in a building to further validate the feasibility of the fiber-wireless centralization for downlink MMW CoMP transmission. As can be seen in the setup, the application of fiber-wireless centralization benefits MMW generation, enhances throughput, centralizes processing, and perfectly synchronizes coordination. Only SFBC mode is evaluated here according to the reason stated in Section 4.2. However, BF mode will be experimentally demonstrated in Section 5.2 in one of the methods.

The experimental setup for evaluation is depicted in Fig. 34. The CO inside the Lab Room centralizes optical MMW signaling, frequency conversion, and all baseband processing. The two RAUs share the same wavelength of 1,553.11 nm from a CW laser source. To generate optical MMW carriers, we use optical PM driven by a 29.24-GHz microwave tone. The microwave source at 14.62 GHz determines the MMW frequency and the coherency between the two RAUs. ILs of 33/66 GHz and 25/50 GHz are used to shape the 58.48-GHz optical MMW carrier shown in Fig. 34(a). After an EDFA, the optical MMW carrier is shared by two links for the two transmitters.

A software defined radio (SDR) platform including a Vertex FPGA chip, DACs, and up-converters is used for the centralized generation of the IF signals. The IF signals follow the LTE-A physical layer parameters for 20-MHz channels – 1200 subcarriers with spacing of 15 kHz, an IFFT/FFT size of 2048, 400 out of 1200 subcarriers set as zeros and pilots, and 512 CP points. The FPGA used for baseband processing establishes real-time 16-QAM mapping, SFBC, OFDM modulation, Zadoff-Chu (ZC) sequence generation, and CP. After 30.72-MSa/s DACs and up-conversion, the IF signals whose electrical spectrum is shown in Fig. 34(b) have a central frequency of 740 MHz. The IF signals are intensity-modulated onto the optical MMW carrier by using a MZM on each link with an output spectrum plotted in Fig. 34(c).

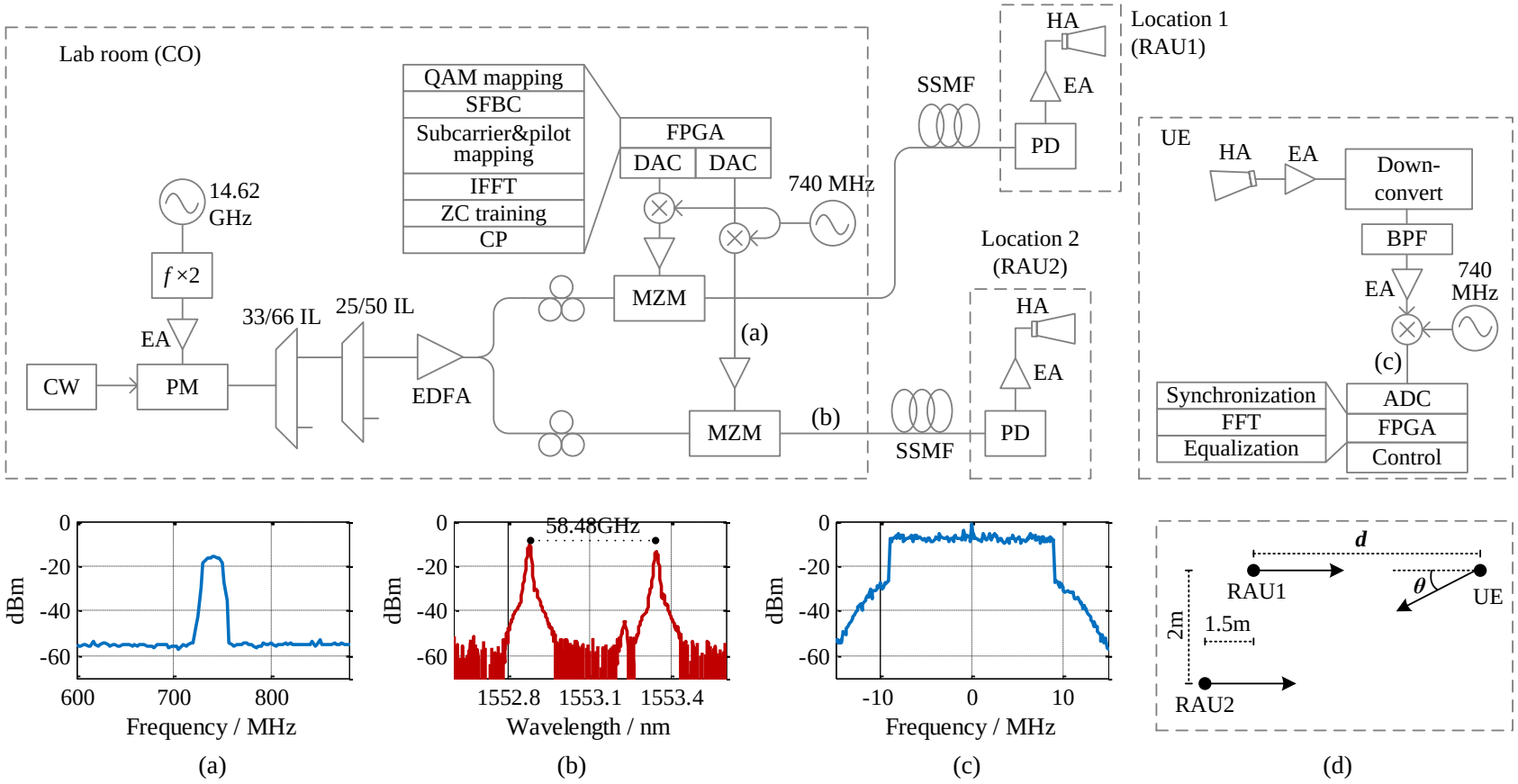

Fig. 34. Experimental setup of a centralized MMW CoMP system supporting two RAUs. Insets: Spectrum of (a) transmitted IF signals, (b) 58.48-GHz optical signals, and (c) received baseband signals; (d) distance and angle configuration.

The two RAUs are approx. 50 m away from the CO. Considering detouring, the fiber links are between 50 m and 100 m. The RAUs have simplified complexity consisting of 60-GHz PDs and EAs. Directional 15-dBi HAs are used for MMW wireless transmission. The distance between the two RAUs is 2.5 m with each one having a 24° half-power beam width for coverage.

On the UE side, after antenna reception and MMW amplification, signals are down-converted to IF by using an envelope detector. Another SDR platform consisting of ADCs and a custom FPGA chip is used for real-time baseband processing including timing and frequency synchronization between CO and UE, OFDM demodulation, SFBC decoding, and equalization. The spectrum of recovered baseband LTE-A signals is plotted in Fig. 34(d). The layout of the RAUs and the UE is sketched in Fig. 34(e) regarding the distance d and angle θ in the following part.

We first execute received-optical-power versus BER test by changing optical power at RAU-1 while fixing the equivalent EIRP at RAU-2 to a small value. The distance between RAU-1 and UE, d, as illustrated in Fig. 34(e), is fixed to 5 m. The EAs at Rx are tuned to a low level to reveal more visible BER trends. As shown in Fig. 35(a), CoMP transmission is more tolerant to power reduction compared with single-point transmission. This is due to the existence of multiple RAUs and the increased SNR. In the high power region, the contribution of CoMP is not significant enough to outperform, and the MMW phase mismatch between two RAUs induces power penalties. However, the curves basically follow the trend of the curves under $p = 0$ in Fig. 6 except the right shift of the curve of the CoMP transmission as a result of the succeeding components after PDs. The highest SNR gain compared to single-point transmission at a BER of $10^{-3.4}$ is approximately 3 dB.

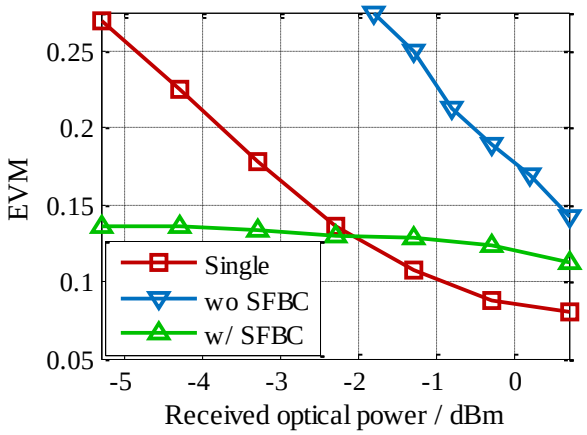
0.25
0.2
0.15
0.1
0.05
EVM
Single
wo SFBC
w/ SFBC
-5
-4
-3
-2
-1
0
Received optical power / dBm

(a)

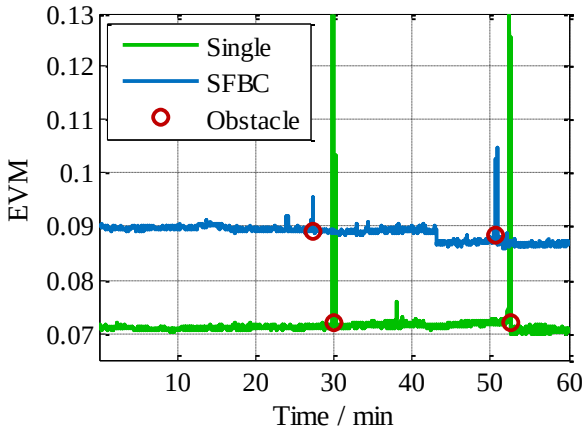
0.13
0.12
0.11
0.1
0.09
0.08
0.07
EVM
Single
SFBC
Obstacle
10
20
30
40
50
60
Time / min

(b)

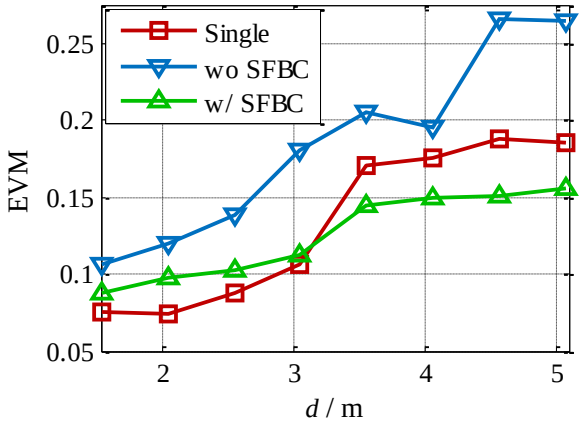
0.25
0.2
0.15
0.1
0.05
EVM
Single
wo SFBC
w/ SFBC
2
3
4
5
d / m

(c)

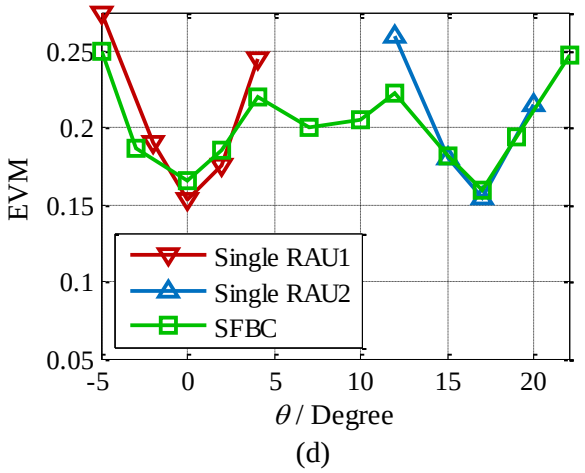

(d)

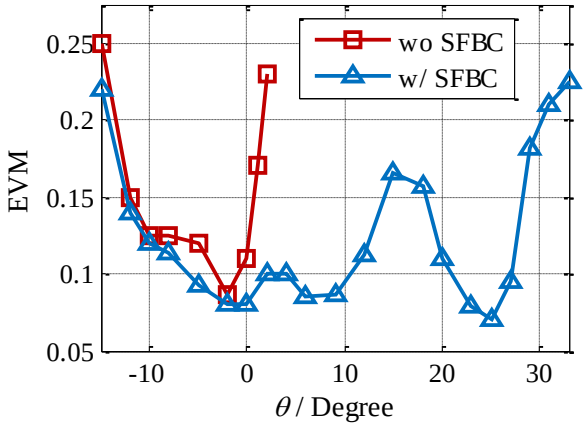

(e)

Fig. 35. Measured BER or EVM of signals under various (a) received optical power, (b) time, (c) distances between RAU-1 and UE, and steering angle with (d) low and (e) high EIRP.

Secondly, we examine the stability of the two transmission schemes by measuring the average EVM value of each OFDM symbol over a continuous 1-hour transmission. The received optical power is fixed to 2 dBm at RAUs, and the distance between RAU-1 and UE, *d* is fixed at 5 m. As shown in Fig. 35(b), the CoMP transmission has smaller variation of EVM over the 1-hr period especially when there are obstacles passing through the MMW wireless link or links. This is consistent with our analysis in section 2.3.2.4 that the CoMP transmission has smaller CV and is also consistent with the simulation shown in Fig. 7.

To better understand the benefits from CoMP transmission, we also establish distance tests by changing the parameter *d*. The received optical power is fixed to 2 dBm at RAUs, and the EIRP from both RAUs is fixed to a low power level so that dramatic BER change can be observed within the limited tested distance range. As shown in Fig. 35(c), CoMP transmission outperforms single-point transmission in long distance region. This is due to the increased received power and capacity of CoMP transmission at distant locations. In short distance where noise is low enough to reveal the impairment caused by MMW phase mismatch, CoMP gain is not obvious. Similar to the case in received-optical-power test, results in Fig. 35(c) basically match the theoretical curves (horizontally flipped) in Fig. 6.

Lastly, one may notice that besides the CoMP gains, the expansion of coverage is another benefit of using CoMP transmission in directional MMW coverage. To verify, we run angle tests by changing the parameter θ as illustrated in Fig. 34(e). The received optical power is fixed to 2 dBm at RAUs, and *d* is fixed to 5 m. In low EIRP tests without ICI, as shown in Fig. 35(d), the CoMP transmission achieves a continuous coverage between two primary directions, while single-point transmission can only provide separated small coverages. In high EIRP tests with ICI, as shown in Fig. 35(e), the CoMP transmission achieves a continuous coverage over 40°, while the interfered transmission can only communicate over the edge area.

4.4 Conclusions

MMW CoMP is feasible in a fiber-wireless centralized architecture. MMW RoF link as a full fiber-wireless centralization solution centralizes network hardware and functions, reduces the complexity of RAUs, and optically provides high-quality and transparent delivery of analog MMW signals. The highly centralized architecture facilitates the JP and resource sharing of CoMP. In fact, fiber-wireless centralization upgrades the conventional distributed CoMP based on backhaul and midhaul to a

centralized version based on the concept of fronthaul as we have introduced in Section 1.2.

Fiber wireless centralization also centralizes all data and information and their processing power into the CO, leaving the cell sites no distributed intelligence for inter-cell communications. This completely avoids any form of overhead traffic thus overcomes the problem stated in 2.4.2.

Through MWP techniques enabled by fiber-wireless centralization, homogeneous MMW signals are optically generated and distributed to RAUs. The centralized generation of MMW also increases the overall power and infrastructure efficiency. This overcomes the problem stated in 2.4.3.

Most importantly, fiber-wireless centralization allows CoMP transmitters to share the same signaling resource at the CO that provides identical time and frequency information and therefore guarantees inherent synchronization on both time and frequency. The delay over RoF links are also stable and minimized with compensable delay difference. This overcomes the problem stated in 2.4.4 and analyzed in Chapter 3.

CHAPTER 5 TECHNIQUES OF CENTRALIZED MMW CoMP

In this chapter we propose and study three techniques based on fiber-wireless centralized MMW CoMP. The first is for small-cell design, in which the method of cell grouping is proposed to enhance MMW coverage and inter-cell handoff in MMW wireless networks. The second is the application of centralized MMW CoMP in multi-section mobile fronthaul, for which we propose the method of radio bundling to improve the fronthaul performance. The third is to discuss the perspective of the application of photonics and optical processing for centralized MMW CoMP.

5.1 Small-Cell Design for Centralized MMW CoMP

Whereas the sufficient available bandwidth of MMW radio makes it a promising candidate for small-cell coverage, its high frequency brings strict criteria on network design for signal coverage [90, 91]. Therefore, an optimized coverage planning is important to provide users robust wireless links in a densified HetNet [92]. In Section 4.3, we have seen that SFBC-based centralized MMW CoMP provides high-quality reception and tolerant MMW links for a UE. Based on this advantage, we will in this section develop the coordination to a network-wide level. We propose a MMW cell grouping method jointly based on the fractional frequency reuse (FFR) concept and the centralized MMW CoMP study in order to provide users globally optimized coverage with robust MMW wireless links.

5.1.1 Operation principle

In a conventional co-channel coverage method where adjacent cells share the same frequency channel, interference exists in cell edge areas, as shown in Fig. 36(a). By using FFR where adjacent cells use different and non-overlapped frequency channels, one

can effectively avoid co-channel interference [93]. However, without coordination, drawbacks induced by the physical property of MMW, such as small coverage sizes and LoS propagation, limit the performance of UEs in cell edge areas, experience bad handoff experience, and increase the sensitivity to shadowing.

Different from the two conventional network plans, MMW cell grouping coordinates a certain frequency channel from each group of adjacent access units. With the centralized coordination for each group of access units, the system-wide coordination improves the performance by providing more continuous coverage and higher chance of LoS in a FFR scheme compared with conventional methods.

Fig. 36(b) shows an example of the proposed MMW cell grouping method, in which each cell group contains two adjacent RAUs and at each RAU two frequency channels are used for FFR. Three of the RAUs are illustrated here. The lower frequency channels from RAU1 and 2 simultaneously bring signal A and its coded form A^* to the union coverage area. The constructiveness of simultaneous transmission is guaranteed by the centralized SFBC and processing enabled by the fiber-wireless architecture. This joint coverage from RAU1 and 2, treated as an integral cell, has larger size than the cells in conventional FFR. For RAU2 and 3, the same method spans a joint coverage providing signal B over the upper frequency channel. The overlapped area of the two new integral cells, i.e. the intersection under RAU2, is the handoff area where UEs communicate singly with RAU2 and can use either frequency channel. It is easy to see that the size of the handoff area is no smaller than the size of the interference-free area in the conventional co-channel method, which guarantees smooth handoffs and continuity. In addition, by using cell grouping, a UE communicates with multiple RAUs when it is outside handoff areas. This decreases the chance of complete NLoS, i.e. all communicating RAUs are obscured, and provides more robust wireless links. It is also worth noting that the grouping method does not increase the number of RAUs or transmitting power although the coverage is improved.

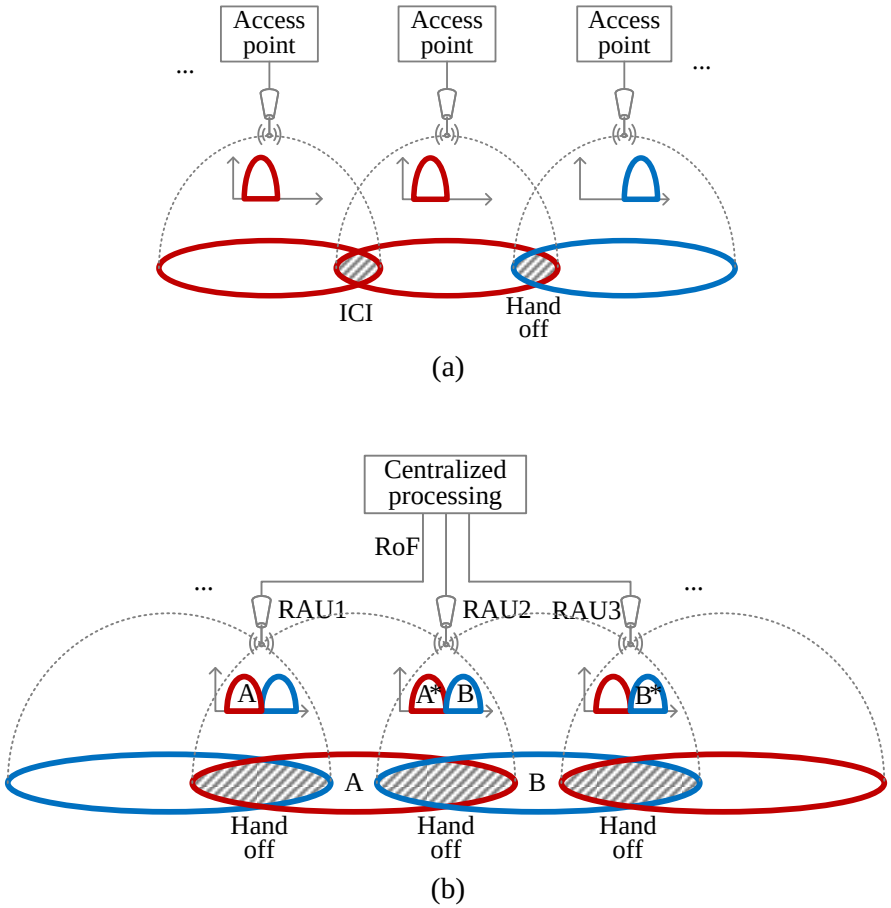

Fig. 36. (a) Conventional network with co-channel and FFR small cells. (b) MMW cell grouping with improved coverage, continuity, and wireless links based on centralized MMW CoMP on two frequency channels.

5.1.2 Experimental setup and results

The setup of a field test with three RAUs for cell grouping is depicted in Fig. 37. At the CO located inside the Lab Room, a CW optical source from a DFB laser at a wavelength of 1,554.67 nm is first applied to a 40-GHz PM. The PM is driven by a 28.75-GHz microwave source, creating MMW combs. After passing an IL of 33/66 GHz, a 57.5-GHz optical MMW carrier whose optical spectrum is plotted in inset (a) is formed. After amplification by an EDFA, the optical link is split into three branches modulated by baseband signals from three arbitrary waveform generator (AWG) outputs.

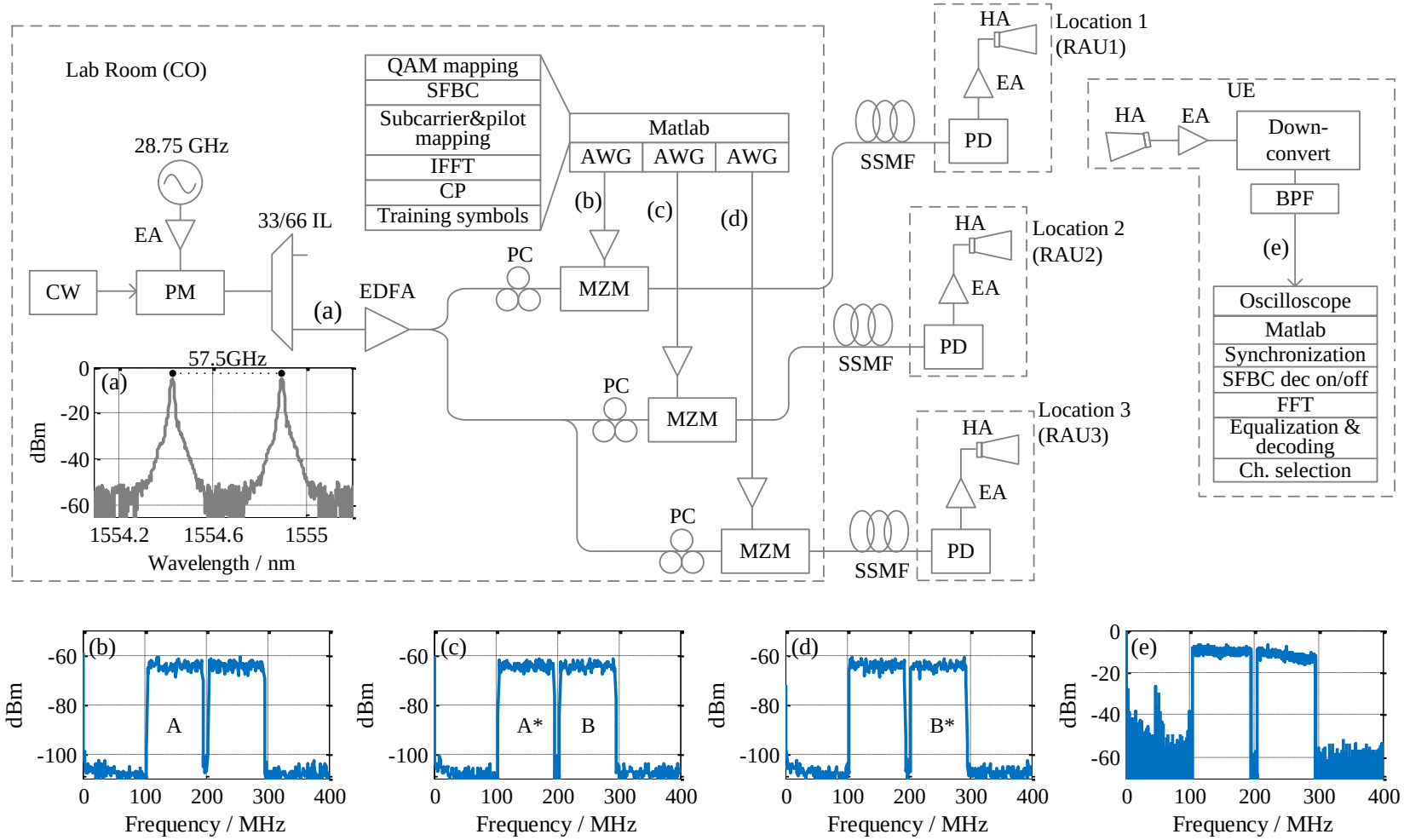

Fig. 37. Experimental setup of cell grouping among three RAUs over two frequency channels in a 57.5-GHz centralized MMW CoMP system. Inset: (a) optical spectrum of 57.5-GHz carrier; (b)-(d) spectra of three AWG outputs; (e) spectrum of received baseband signals.

The baseband signal on each branch consists of a lower channel from 105 MHz to 195 MHz and an upper channel from 205 MHz to 295 MHz. Each channel is modulated as 16-QAM-OFDM with a 15-kHz subcarrier spacing (LTE). The measured spectra of the three AWG outputs are plotted in inset (b)-(d). The coordination scheme is the same as illustrated in Fig. 36(b), where the subcarriers in the lower channel of RAU2 are coded by SFBC with respect to the ones of RAU1 while the subcarriers in the higher channel of RAU3 are coded with respect to the ones of RAU2. The coordination based on SFBC is achieved by the fact that baseband processing for all RAUs takes place within the CO. The electrical signals are fed into three MZMs to modulate the optical MMW carrier by using intensity modulation.

After fiber distribution to three RAUs located approximately 50 m away from the Lab Room, signals are detected by three 60-GHz PDs and amplified by EAs. The 57.5-GHz MMW signals are radiated by HAs with a 15-dBi gain and a 24° half-power beamwidth.

On the UE side, the FE consists of an HA, an EA, and a V-band envelope detector for frequency down-conversion. In the baseband processing, correlation is first done to extract timing and signal strength information. Based on this information, the system decides whether SFBC decoding is to be applied. In other words, the system decides if UE is located under a joint coverage from two RAUs or under a coverage primarily from one RAU. After OFDM demodulation, the channel with higher signal quality is chosen as the serving channel and its data are recorded.

The configuration layout is illustrated in Fig. 38. The spacing of the three RAUs is fixed at 3.5 m. The location of UE, expressed as (x_U, y_U) in meters, is subject to change regarding the following tests. The steering angle of UE with respect to minus x-axis is denoted as θ in degrees.

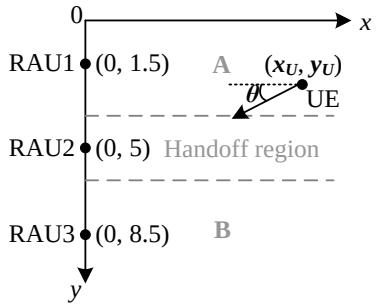

Fig. 38. Experimental configuration of RAUs and UE.

We first test the coverage performance in terms of error EVM by changing y_U while fixing x_U = 6 m and θ = 0°. The steering angle of the three RAUs is fixed at the *x*-axis direction. The received optical power at all RAUs is fixed at -1.5 dBm. Fig. 39(a) gives the results over a 10-m test range for conventional co-channel, conventional FFR, and proposed cell grouping methods. In co-channel transmission where all three RAUs transmit over the lower channel, signals cannot be recovered in overlapped areas because of strong co-channel interference. Although FFR can mitigate co-channel interference, the EVM curve still has obvious increase near cell edges, i.e. y_U = 3.25 m and y_U = 6.75 m. This is mainly due to the power decrease when UE is away from primary RAU positions, i.e. y_U = 1.5, 5, and 8.5 m. Different from the two conventional methods, cell grouping keeps the signal quality more stable over the whole test range. Specifically, cell grouping has a 3.5-dB reduction in EVM in cell edge areas compared with the FFR method.

We second test the coverage performance by changing the steering angle θ while fixing the position of UE at (x_U=6, y_U=5). The steering angle of the three RAUs is fixed at the UE direction. Other configurations are the same as previous. Fig. 39(b) gives the results in a 90° test range. As shown by the curves, the co-channel method can only recover in very limited angle ranges because of interference; the FFR method has deterioration when biased from primary RAU directions; cell grouping has constantly low EVM over the whole range. A 3.5-dB EVM reduction is also observed at edge angles.

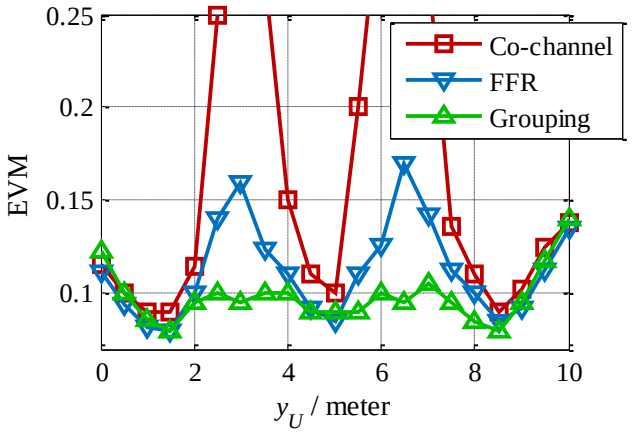

(a)

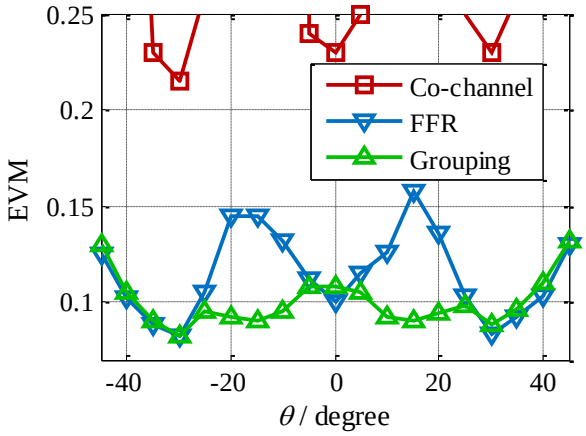

(b)

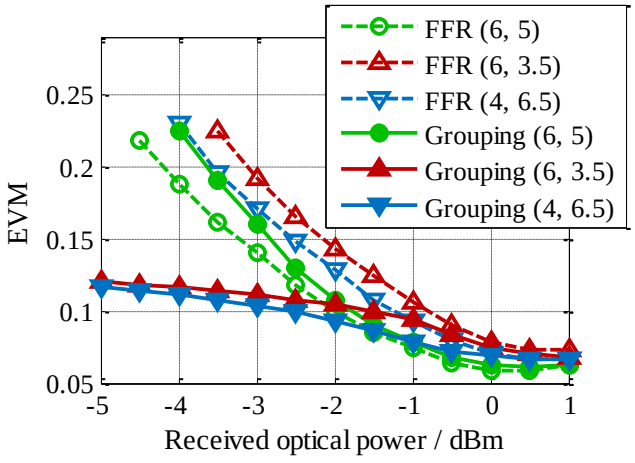

(c)

Fig. 39. EVM tested under different (a) UE positions, (b) steering angles, and (c) received optical power.

Thirdly, we test the power performance by changing the received optical power at RAU2 while fixing the power at RAU1 and 3 at -1.5 dBm. The steering angle of UE is fixed at $\theta = 0°$ and the one of RAUs is fixed at the x-axis direction. Other configurations are the same as previous. Three positions are tested with curves shown in Fig. 39(c). When UE is located at (x_U=6, y_U=3.5) or (x_U=4, y_U=6.5), SFBC decoding is automatically on and cell grouping is tolerant to optical power loss at RAU2. Compared with the conventional FFR method, cell grouping has up to 3.5-dB improvement when EVM is 0.12. When UE is located at (x_U=6, y_U=5), RAU2 is dominant and received wireless power from RAU1 and RAU3 is low. In this case, SFBC decoding is automatically off and the receiving performance is equivalent to the FFR method.

We also test the tolerance of the system to NLoS scenarios by setting obstacles, including cloth, paper board, and human body, between RAU2 and UE. The received optical power is fixed at -1.5 dBm. Other configurations are the same as previous. As shown in Table IV, in both two tested positions, cell grouping shows smaller increase in EVM compared with the FFR method under different NLoS scenarios. When the MMW radio between RAU2 and UE is obscured by human body, the EVM of cell grouping is still under 0.12 while the FFR method completely loses its signals.

Table IV. EVM under different NLoS shadowing

	LoS	Cloth	Paper	Body
FFR (6, 3.5)	0.124	0.150	0.180	X
FFR (4, 6.5)	0.108	0.129	0.140	X
Grouping (6, 3.5)	0.100	0.110	0.112	0.118
Grouping (4, 6.5)	0.086	0.092	0.098	0.101

5.2 Mobile Fronthaul based on Centralized MMW CoMP

In this section, we propose a reconfigurable MMW radio bundling method to improve system efficiency and transmission reliability in multi-section fiber-wireless mobile fronthaul. A multi-point multi-section experiment demonstrates improved signal quality and reliability.

5.2.1 Application scenario

Mobile fronthaul is the last chain that provides proximity facing mobile users. The exponential growth of users' demands directly drives the expansion of mobile fronthaul. A solid fronthaul design is the key approach to build efficient channels from centralized BBU pool to users [94]. As cell amount increases, a huge amount of fronthaul links are needed to distribute high-density, high-frequency, and high-performance small cells. These require the fronthaul design be high-capacity, light-weight, flexible, and transparent to services. Furthermore, fronthaul deployment also faces challenges from different environmental conditions. In urban areas, for example, continuous wiring between the BBU pool and distant RAUs sometimes can be impossible or cost-prohibit. In this case, MMW wireless links can function as a relay section and provide more adaptive connections than fiber cables. By cascading MMW relays and optical fiber links, a multi-section RoF link as introduced in Section 4.1 can support high capacity and high flexibility at the same time [95, 96]. However, a point-to-point MMW relay may become the bottleneck of the entire link as it is vulnerable to power loss, antenna misalignment, and NLoS propagation.

On top of the agility of multi-section RoF fronthaul, we propose to unite independent MMW relays and assemble them into a reconfigurable MMW radio bundle working as the middle joint of a fronthaul network, as shown in Fig. 40. By creating a MMW radio bundle, we increase the overall capacity of the fronthaul network, as the bundling provides higher SNR, higher diversity and tolerance to NLoS propagation,

compared with single point-to-point transmission. Moreover, by combining independent fronthaul links, we can increase the infrastructure utilization, especially the utilization of MMW FEs. This research is scenario-oriented with experimental evaluation in the context of multi-section mobile fronthaul that experiences RoF transmission both before and after the MMW relay.

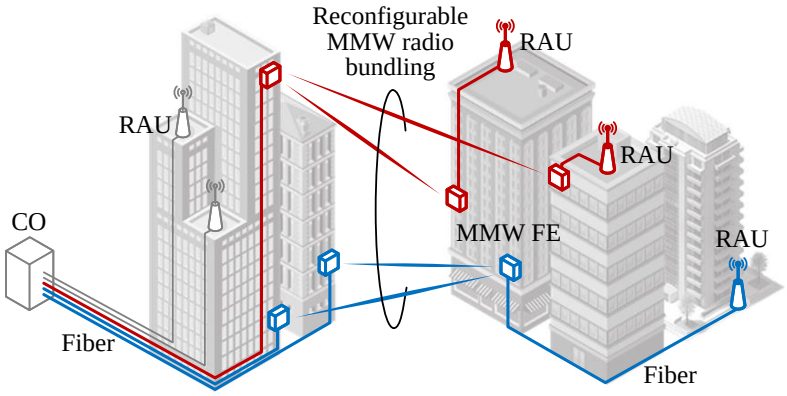

Fig. 40. Reconfigurable MMW radio bundling in multi-section fiber-wireless mobile fronthaul and uplink and downlink of 2×1 transmission.

5.2.2 Multi-point transmission in MMW radio bundling

By assembling independent MMW wireless relays to a reconfigurable MMW radio bundle, we can improve infrastructure utilization and signal reliability as it changes single point-to-point transmission into multi-point transmission. A MMW radio bundle consists of two types of multi-point transmission – 1×N and N×1 transmission. We are not considering M×N (M, N > 1) here, which achieves a multi-cell MIMO scenario from the view of access sites, because the realization of multi-cell MIMO is unlikely to rely on the MMW radio bundle and the density of MMW relays is still too low to achieve multi-cell MIMO transmission. For 1×N, as colored red in Fig. 40, the structure is equivalent to a distributed antenna system (DAS) that enlarges its coverage by connecting one BBU to N RAUs (N=2 in Fig. 40). For N×1, as colored blue in Fig. 40, the structure can provide

signal improvement only if pre- and post-processing are implemented in downlink and uplink, respectively. In uplink, post-processing such as maximal ratio combining (MRC) can be applied after two different copies of the signal are received at the CO [97, 98]. In downlink, N×1 transmission can provide the gains that we have discussed in Section 2.3 if pre-processing such as SFBC or BF is implemented at the CO. SFBC guarantees the (quasi-)orthogonality between multiple transmitted wireless signals while BF provides a constructive phase relationship between the signals by channel estimation and pre-equalization.

5.2.3 Experimental setup and results

We experimentally evaluate the downlink of MMW radio bundling in a multi-section RoF fronthaul system. The setup is depicted in Fig. 41. At the CO, a CW optical signal from a DFB laser at a wavelength of 1,553.84 nm is first applied to a 40-GHz PM driven by a 28.75-GHz tone to create MMW combs. A 57.5-GHz optical MMW carrier whose optical spectrum is plotted in Fig. 41(a) is formed by passing a 33/66-GHz IL. After amplification through an EDFA, the optical link is split into two branches to be modulated by HF signals. The HF signals from an AWG are fed into two MZMs to modulate the optical MMW carrier by using IM. The spectra of the AWG outputs are depicted in Fig. 41(b) and (c) for SFBC mode and BF mode, respectively. They both have 16-QAM-OFDM formats with a 100-MHz bandwidth and a 75-kHz subcarrier spacing. The HF signal has a central frequency of 700 MHz.

After 25-km and 20-km SSMF transmission over the two links, respectively, the signals are detected by two PDs and amplified by EAs at the two MMW FEs. The 57.5-GHz MMW signals are radiated by two HAs with a 25-dBi gain. The spacing between the two transmitting MMW FEs is 1 m. The MMW wireless distance between the transmitting FEs and their receiving counterpart is subject to change from 1.5 m to 4.5.

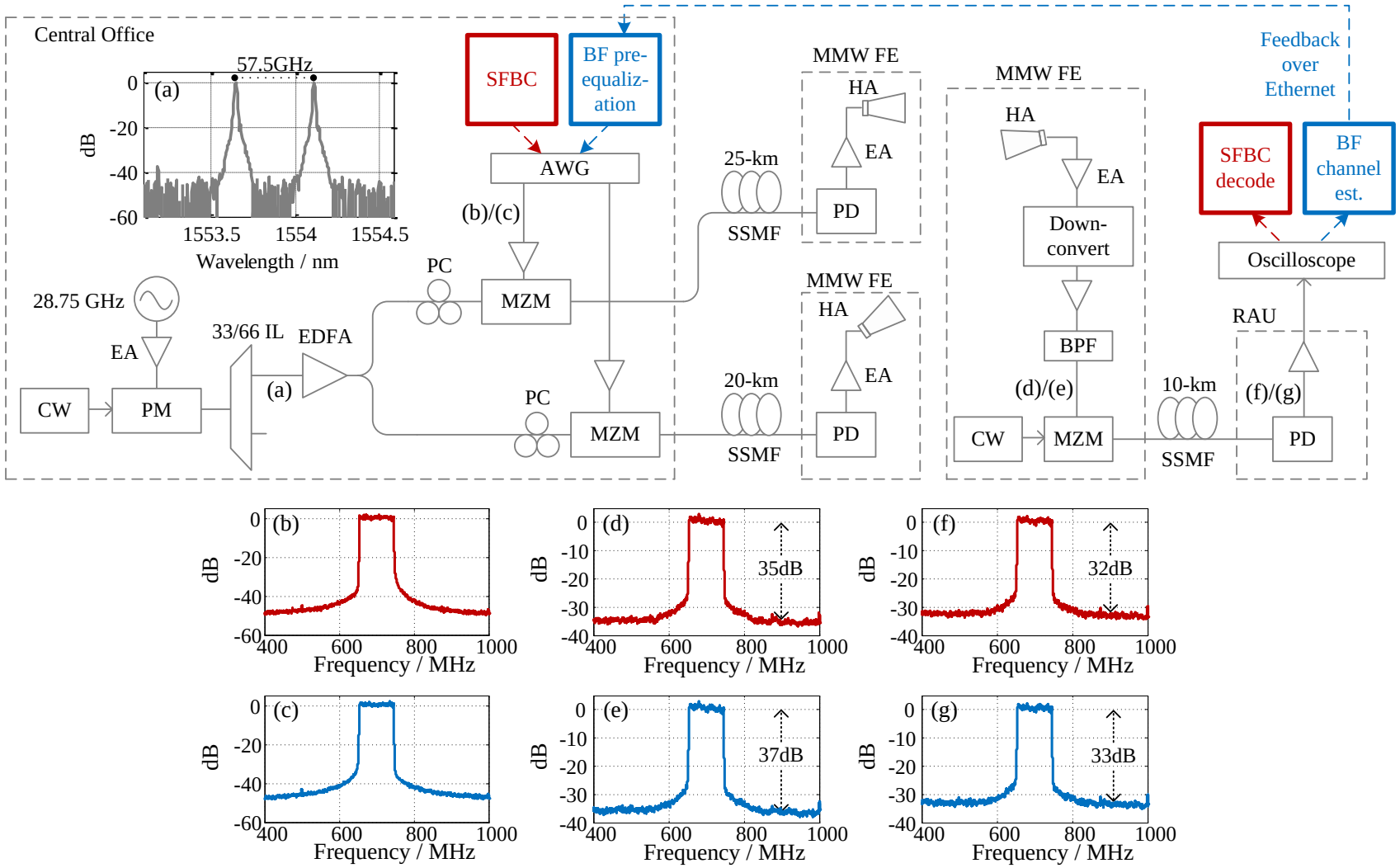

Fig. 41. Experimental setup for downlink transmission of MMW radio bundling in multi-section fiber-wireless mobile fronthaul and normalized spectrum at different locations.

The received MMW signal is amplified and down-converted by using a V-band envelope detector. After an EA and a BPF the HF signal has a maximal SNR of 35 dB in SFBC mode and a maximal SNR of 37 dB in BF mode as shown in Fig. 41(d) and (e), respectively. Another stage of IM is applied to the HF signal for the second section of fiber transmission after the MMW relay.

At the RAU after 10-km SSMF, the 700-MHz signal is detected by a 2.5-GHz PD. A maximal SNR of 32 dB in SFBC mode and a maximal SNR of 33 dB in BF mode are measured as shown in Fig. 41(f) and (g), respectively. The HF signal is analyzed after captured by an oscilloscope. When BF is applied, the feedback mechanism is realized over an Ethernet connection between the scope, the AWG, and a computer for channel estimation.

We first test received-optical-power performance by changing the optical power at the MMW FE of the 25-km RoF link and measuring the EVM at the RAU. The MMW wireless distance is fixed to 1.5 m during the test. As shown in Fig. 42(a), two bundling methods have lower EVM and are less sensitive to power change compared with conventional single point-to-point transmission because of SNR gain. Comparing SFBC and BF, the latter has slightly lower EVM because of higher SNR gain from the channel estimation and pre-equalization. In addition, 25/20+10-km fiber transmission induces less than 1-dB penalty compared with BTB transmission. Over the entire power range, EVM maintains below 10% when MMW radio bundling is adopted. Similar results are observed when EVM values are measured at the receiving MMW FE, as shown in Fig. 42(b). The second section of RoF transmission induces a 1~2% EVM increase by comparing Fig. 42(a) and (b).

Secondly, we execute distance test by changing the MMW wireless distance. The received optical power is fixed to 1 dBm at the two transmitting FEs and -1 dBm at the RAU. As shown in Fig. 42(c), at 12.5% EVM level [73], two bundling methods have at least 22% distance extension compared with single transmission.

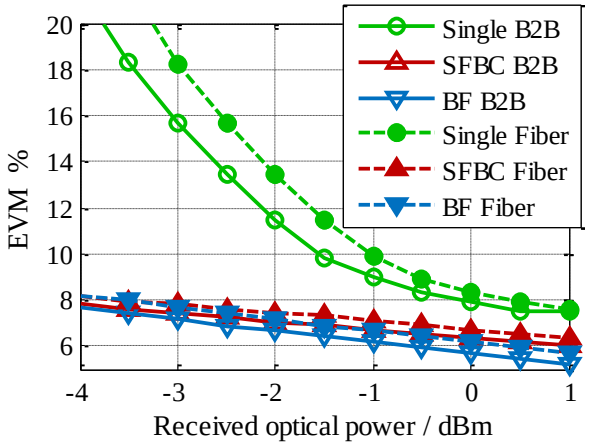
Single B2B
SFBC B2B
BF B2B
Single Fiber
SFBC Fiber
BF Fiber
EVM %
Received optical power / dBm

(a)

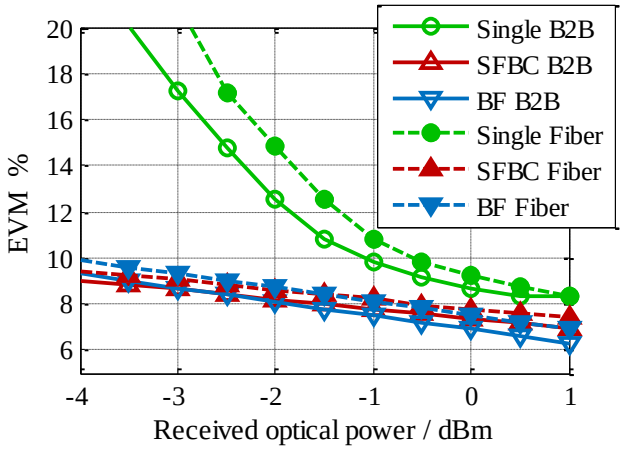
Single B2B
SFBC B2B
BF B2B
Single Fiber
SFBC Fiber
BF Fiber
EVM %
Received optical power / dBm

(b)

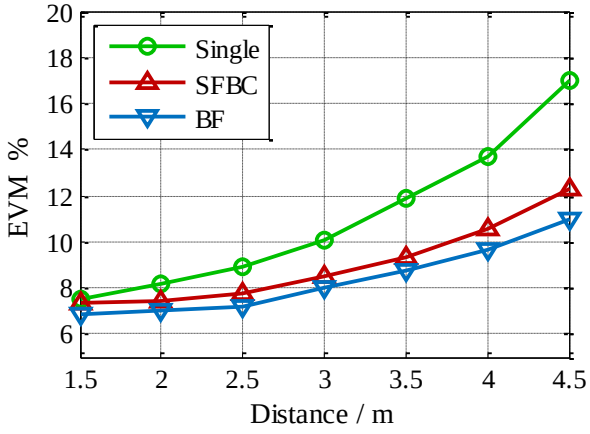
Single
SFBC
BF
EVM %
Distance / m

(c)

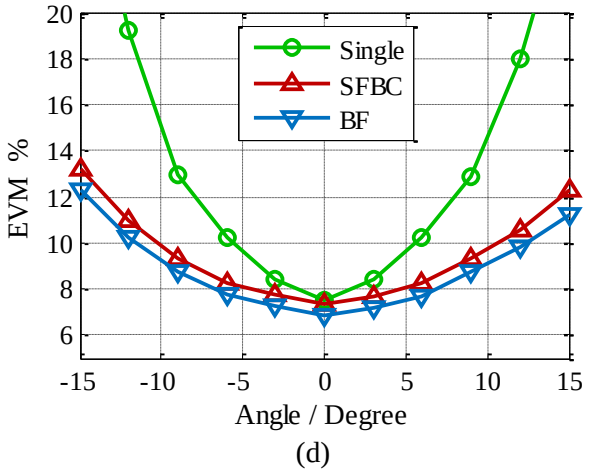

Fig. 42. EVM of 16-QAM symbols measured at (a) RRAU and (b) receiving MMW FE under various received optical power. EVM of 16-QAM symbols measured at RAU under various (c) MMW wireless distances, (d) antenna steering angles, and (e) NLoS shadowing.

Thirdly, we establish angle test by changing the steering angle of one of the two transmitting FEs. The angle is measured with respect to the elevation plane of the receiving antenna. The setup of optical power follows previous test. The MMW wireless distance is 1.5 m. As shown in Fig. 42(d), at 12.5% EVM level, two bundling methods have at least 76% higher tolerance to angle misalignment. This is due to the simultaneous transmission and consequently larger coverage angle from the two MMW FEs.

Lastly, we consider NLoS scenarios in the MMW radio bundle and examine the diversity of the system and the tolerance to partial shadowing of MMW wireless links. The setup of optical power and wireless distance follows previous test. Fig. 42(e) plots the results. As we increase the shadowing of the LoS path, two bundling methods maintain a high signal quality while single transmission drops signal (EVM > 12.5%) when more than 40% of the LoS path is obscured. At 100% NLoS, SFBC and BF become single transmission and have the same performance of 11% EVM that is determined by the unblocked MMW link.

5.3 Optical Processing for Centralized MMW CoMP

In the previous coordination methods, we have been using coding and equalization to provide orthogonality or constructiveness, and both of them are realized in electrical domain. In fact, another benefit of doing fiber-wireless centralization is that its optical platform potentially enables all-optical signal processing.

All-optical and MWP processing has been under popular research thanks to its "unlimited" bandwidth and fast speed [99, 100]. For centralized MMW CoMP, there are three potential advantages of using all-optical processing. First, it can take good advantage of the flat channel of MMW as the processing in optical domain is also tend to be flat. Second, coordination is to eventually solve the problems in wireless transmission. The fiber-wireless architecture maintains the coherency between the optical signals and the wireless signals, in other words, the coherency between the CO and the RAUs. This theoretically allows us to realize wireless coordination at the RAUs via the operation of optical coordination at the CO. Third, all-optical processing provides fundamental basis for future silicon photonics or III-V integration which is the super-high-speed alternative for current electrical solutions [101, 102]. Therefore, we propose the method of optical coordination in this section based on the centralized MMW CoMP concept.

Although optical coordination is based on the centralized platform and also the theory of MMW CoMP, it is independent realization and different from the SFBC and BF modes that we have been studying. As a result, the application scenarios are also different. In the following, we will use optical interference cancellation (OIC) and optical cooperative MIMO as two examples to demonstrate how optical coordination works.

5.3.1 Optical interference cancellation

5.3.1.1 Application scenario

We depict a most simple case of OIC based on a fiber-wireless centralized system in Fig. 43 and will use this case for further analysis. In the system, UE1 is communicating with RAU1 while UE2 is communicating with RAU2. Somehow, UE2 receives interference from RAU1. To cancel the interference, RAU2 include a component in its transmitted signal that can counteract the interference from RAU1. To realize this, one optical MMW generation module is shared by all transmitters at the CO to guarantee the coherency of MMW signals during both optical and wireless transmission. After independent modulation and processing at transmitters, the output optical signals are jointly processed inside an optical coordination module over the fiber links at the frontend of the CO. The module realizes amplitude and/or phase adjustment on each link and its branches. The branches enable optical signal exchange across the fiber links if ICI exists. This structure realizes OIC through analog approaches after CSI feedback is retrieved from UEs.

5.3.1.2 Optical coordination

In directional low-power small-cell applications, the communication channel over MMW bands can be considered as flat and therefore can be processed through optical channels which are also flat. Based on this, the coordination realized by the optical module can completely emulate and compensate the MMW wireless channels. The

process inside the optical module is according to the phase and magnitude relationship during optical-to-electrical (O/E) conversion. We hereby study this relationship between the optical domain and the electrical domain, and the relationship of optically coupled MMW signals.

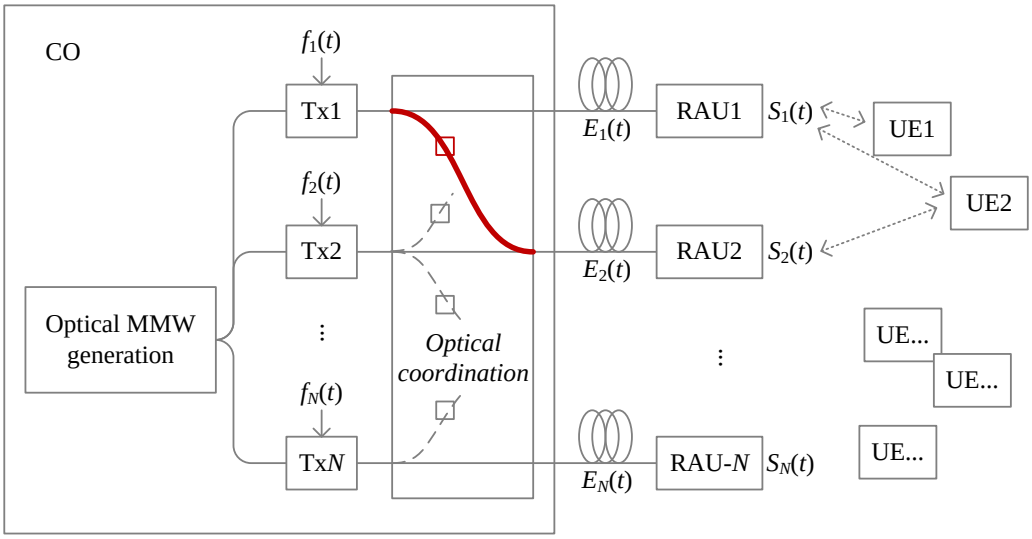

Fig. 43. Functional blocks of a MMW OIC system based on RoF.

First consider the case without coupling. As shown in Fig. 43, over the fiber link corresponding to RAU1, a complex baseband signal $f_1(t)$ is carried by an optical MMW carrier with respect to the central wavelength. The optical field can be expressed as

$$E_1(t) = \exp(j2\pi \frac{ct}{\lambda_1}) + f_1(t)\exp\left(j(2\pi \frac{ct}{\lambda_1} + \Omega_{\mathrm{MMW}} t + \varphi_1)\right), \tag{35}$$

where c, λ_1, Ω_{MMW}, and φ_1 are the speed of light, the central wavelength for RAU1, the MMW frequency, and the phase shift of the MMW carrier for RAU1, respectively. The wireless MMW signal, i.e., the photo detection output at RAU1 after BPF is

$$S_1(t) = \mathrm{BPF}[|E_1(t)|^2] = 2 f_1(t)\cos(\Omega_{\mathrm{MMW}} t + \varphi_1), \tag{36}$$

where the complex envelope $f_1(t)$ and the MMW phase φ_1 are both preserved from optical to electrical signals.

After wireless transmission, the interference received by UE2 from RAU1 is

$$y_1(t) = |h_1| f_1(t) \cos(\Omega_{\mathrm{MMW}} t + \varphi_1 + \varphi_{h1}), \tag{37}$$

where the h_1 is the wireless channel response from RAU1 to UE2.

To realize OIC, signals are optically coupled inside the optical coordination module. The optical signal $E_1(t)$ in the fiber link to RAU1 is coupled into the fiber link to RAU2 after magnitude and phase adjustment on both links, as shown by the red branch in Fig. 43. At transmitters Tx1 and Tx2, the two corresponding signals, $f_1(t)$ and $f_2(t)$, are carried on two different wavelengths carrying identical MMW carriers generated by the same optical MMW generation module. The optical signal inside the fiber link to RAU2 after the coupling can be written as

$$\begin{aligned} E_2(t) = {} & k \exp(j2\pi ct/\lambda_1) + k f_1(t) \exp(j2\pi ct/\lambda_1 + j\Omega_{\mathrm{MMW}} t + j\varphi_2) \\ & + \exp(j2\pi ct/\lambda_2 + j\psi) + f_2(t) \exp(j2\pi ct/\lambda_2 + j\Omega_{\mathrm{MMW}} t + j\psi). \end{aligned} \tag{38}$$

In the equation, k is the magnitude of the optical MMW signal getting coupled; λ_2 is the central wavelength of the optical signal for RAU2; ψ is the relative phase difference between the two central wavelengths. The photo detection beats out heterodynes containing the MMW frequency. Considering the wavelength spacing

$$|2\pi c/\lambda_1 - 2\pi c/\lambda_2| >> \Omega_{\mathrm{MMW}}, \tag{39}$$

the wireless MMW output after BPF at RAU2 is

$$\begin{aligned} S_2(t) &= \mathrm{BPF}[|E_2(t)|^2] \\ &= 2k^2 f_1(t) \cos(\Omega_{\mathrm{MMW}} t + \varphi_2) + 2 f_2(t) \cos(\Omega_{\mathrm{MMW}} t), \end{aligned} \tag{40}$$

where φ and k, i.e. the magnitude and phase relationships, are all preserved from the optical domain to the electrical domain.

After wireless transmission, the interference received by UE2 from RAU2 is

$$y_2(t) = |h_2| k^2 f_1(t) \cos(\Omega_{\mathrm{MMW}} t + \varphi_2 + \varphi_{h2}) + |h_2| f_2(t) \cos(\Omega_{\mathrm{MMW}} t), \tag{41}$$

where the h_2 is the wireless channel response from RAU2 to UE2.

According to the relationship we have derived, the coordination of MMW

wireless signals can be realized by changing optical parameters, φ_2 and k, on optical links inside the module following

$$k^2 = |h_1| / |h_2| \tag{42}$$

and

$$\varphi_2 = \varphi_1 + \varphi_{h1} - \varphi_{h2} \tag{43}$$

so that the interference from RAU1 is neutralized and OIC is realized.

5.3.1.3 Experimental setup and results

Fig. 44 shows the experimental setup of the MMW OIC method based on a fiber-wireless system. In this setup, one CO, two RAUs through 20-m fiber links and two sets of UE associated with two small cells are evaluated. At the CO, two CW lasers at different wavelengths, 1564.2 nm and 1554.6 nm, are used for coarse wavelength-division multiplexing (CWDM) [103]. They are simultaneously phase-modulated by a 30-GHz tone doubled from a 15-GHz source to generate OFC centered at the two wavelengths. After a 30/60-GHz IL and optical filters at corresponding wavelengths, two 60-GHz optical MMW carriers at the two wavelengths are formed and amplified over the two links. The carriers are then intense-modulated by two channels of 1-Gb/s OOK signals using MZMs (it is worth noting that this approach is not limited to binary or scalar signals, but also complex modulation formats such as QAM and OFDM). Corresponding optical spectra are shown in insets (a) and (b). At the front end of the CO, an optical module is implemented for realizing the OIC between the fiber links heading to two cell sites. Inside the module, attenuation and delay (to cause linear phase shifting) are implemented according to the feedback from UEs. A portion of the signal in one link is coupled into the other link corresponding to the cell serving the interfered UE. This structure enables the cancellation to switch between two one-sided interference scenarios. In the scenario of this experiment, the downlink interference is from RAU1 to UE2, determining a coupling direction as shown in the figure. The directions of the horn

antennas, whose directional pattern with a 24° half-power beamwidth effectively emulates the beamforming features though with different mechanisms, are steered to corresponding UE locations. Three line-of-sight pairs are formed here: RAU1-UE1, RAU2-UE2, and the interference path RAU1-UE2. Relying on the signal relationship between optical and wireless signals as indicated in (38) and (40), we tune the attenuator and the delay line in the module so that the interference from RAU1 to UE2 can be eliminated. Thus, pure signals from Data2 can be directly retrieved at UE2 without any interference component.

To validate the feasibility of this approach, in Fig. 45 we spread out the eye diagrams after different configurations for end-to-end transmissions. As references, Fig. 45(a) and (b) show signals received by UE2 with only RAU1 or RAU2 transmitting, respectively. In Fig. 45(c), the eye diagrams illustrate the composite signal received by UE2 simultaneously from two RAUs with phase differences sketched as the colored vectors. Since no CoMP is used, the combination of the two interfering OOK signals forms four levels with two digits each, marked beside the diagrams, representing the data dedicated to UE1 and UE2, respectively. In this plot, one cycle of the eye diagram transmutation corresponds to a 5-mm wireless link movement of the antenna at RAU1. According to (37) and (42), the *relative* attenuation k can be estimated from the four levels. Fig. 45(d) shows the interaction between the interference component from RAU1 and the cancellation component from RAU2 at UE2 when CW2 and the succeeding EDFA are shut down. One cycle of the eye diagram transmutation corresponds to the period of 16.7-ps delay inside the cancellation module. Under an estimate on the attenuation k, the one at the 180° position cancels the interference from RAU1 to UE2. Fig. 45(e) shows the interaction of the three signal components with different cancellation phase values. For any signal dedicated to UE2, under a close estimate on k, a cancellation phase between 120° and 240° can mitigate the interference, while a phase at 180° can cancel the interference by maximum.

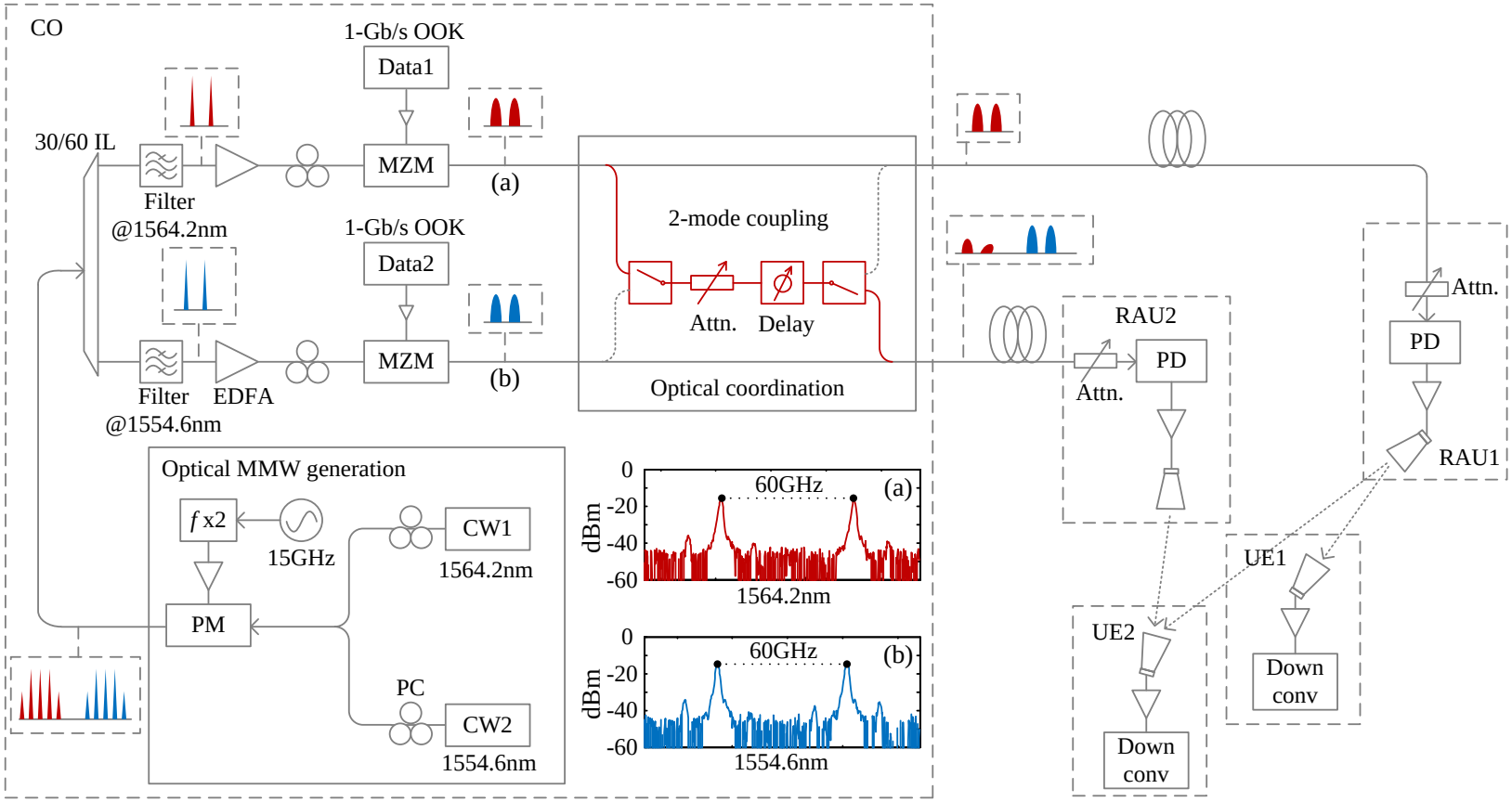

Fig. 44. Experimental setup for MMW OIC in a fiber-wireless system. Insets: spectra of optical MMW signals dedicated to (a) UE1 and (b) UE2.

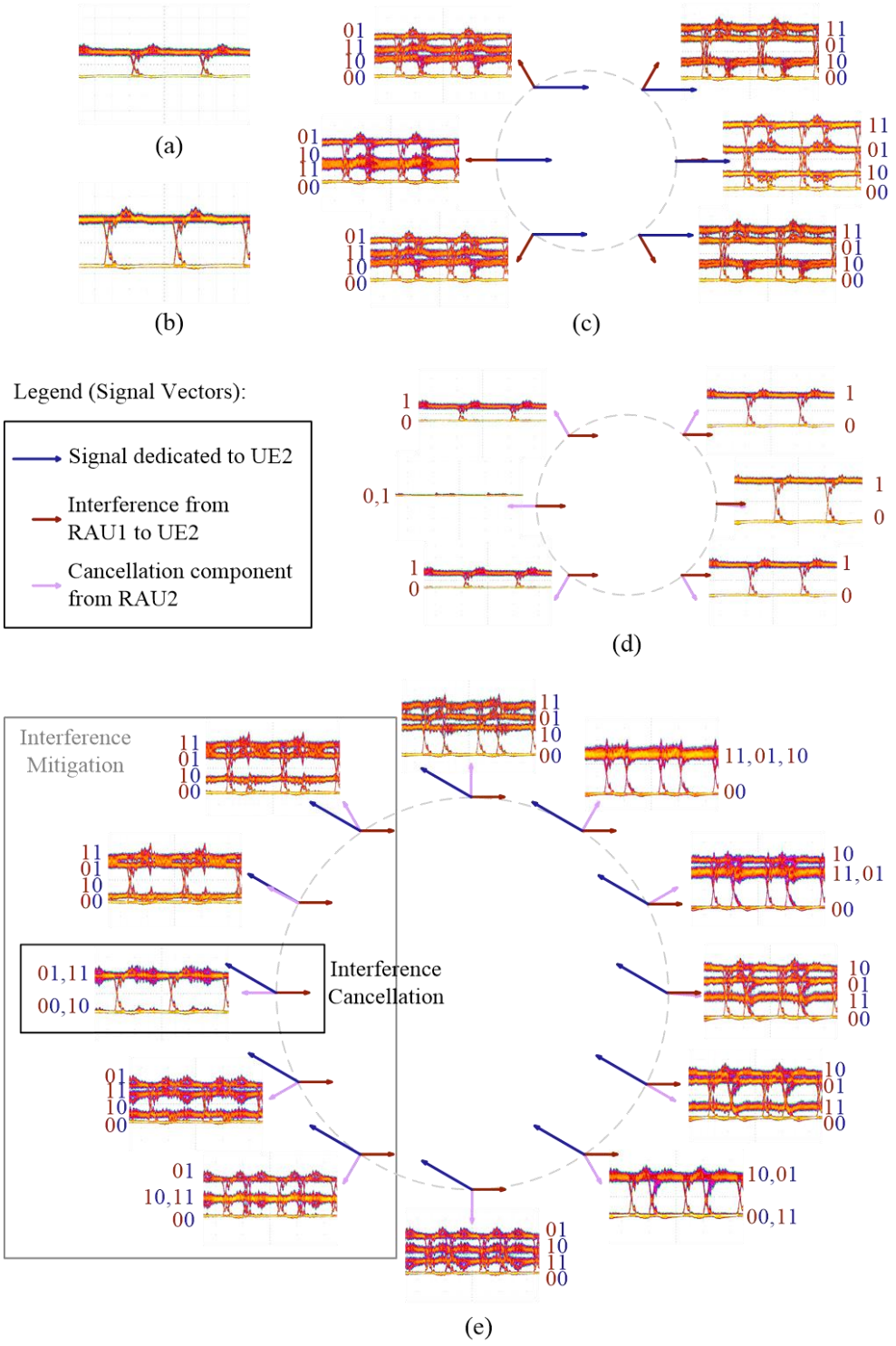

Fig. 45. Eye diagrams of (a) the interference originated from RAU1 to UE2 and (b) the signal dedicated to UE2. Eye diagrams and signal vectors of (c) the interference between two RAUs without CoMP, (d) the interaction between the interference from RAU1 and the cancellation component from RAU2, and (e) the interaction of the three components with different cancellation phase values.

In Fig. 46, the BER performance of the system is given. Two interference receptions, both from RAU1 to UE2, by changing the layout of the antenna pairs are tested in Fig. 46. Along with the two tests, an interference-free reception is also tested as a reference. In addition, due to the coupling and dependence of optical power at the two RAUs, we only test the received optical power at RAU2. By using OIC, the receiving performance is improved to a level with a penalty less than 1 dB with respect to interference-free single-RAU receptions. On the other hand, the reception with interference but without OIC has worse performance with uncertainty. Generally, the BER performance without OIC is better when the interference and the signal are in-phase and constructive on eye diagram corresponding to the right half of the cycle in Fig. 45(c), while the performance with OIC is better when the interference and the signal are out-of-phase and deconstructive corresponding to the left half of the cycle as a result of higher electrical amplification efficiency at RAU2. Furthermore, it is worth noting that this approach is not limited to binary or scalar signals, but also complex modulation formats such as QAM and OFDM.

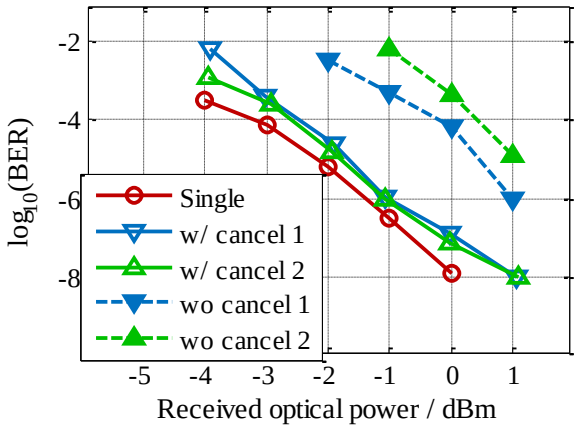

Fig. 46. BER performance measured at UE2 under an interference-free reception and two interfered reception tests.

5.3.2 Cooperative MIMO based on optical processing

5.3.2.1 Application scenario

According to the experiment above, we see that the specific setup for fiber-wireless based OIC can mitigate interference and improve signal quality at cell edge areas. To realize the general case of OIC, MIMO, the multi-antenna technology has great potential to further increase data rate and/or to improve signal quality for MMW communications [104]. In MMW devices, antenna arrays with a large number of elements can be integrated into a small volume because the necessary antenna spacing is on the order of millimeters. However, with the high-attenuation propagation properties, MMW MIMO is more difficult to obtain gains since spatial decorrelation usually relies on rich multipath propagation. The insufficiency of scattering at MMW frequencies results in relatively high spatial correlation, which limits the potential capacity increase. In a LoS system with wireless distance of 5 m, for instance, the antenna spacing at either transmitters or receivers has to be tens of centimeters to reduce the spatial correlation [105]. This spacing can hardly be realized inside a single device.

The preliminary study on OIC in 5.3.1 can be generalized into the field of cooperative MIMO, or multi-cell MIMO, to provide desired transmitter antenna spacing and hence enable the decorrelation at MMW frequencies [106]. A conceptual diagram of the cooperative MIMO for MMW communications is shown in Fig. 47. In this example, RAU1 and RAU2 belonging to two different cells jointly communicate with the UE that features a MIMO transceiver when the UE is in the common coverage area. Considering that cooperative MIMO transmission involves massive communications among multiple cell sites especially in very-high-throughput MMW communications, RoF can provide high capacity links with efficiently centralized processing and friendly radio interface [57, 107]. Based on the RoF infrastructure, we will further develop the optical coordination method to explore the feasibility of deploying the ZF pre-coding in the optical domain

with centralized processing. RoF and optical coordination coming together can highly reduce backhaul traffic and digital signal processing for cooperative MIMO.

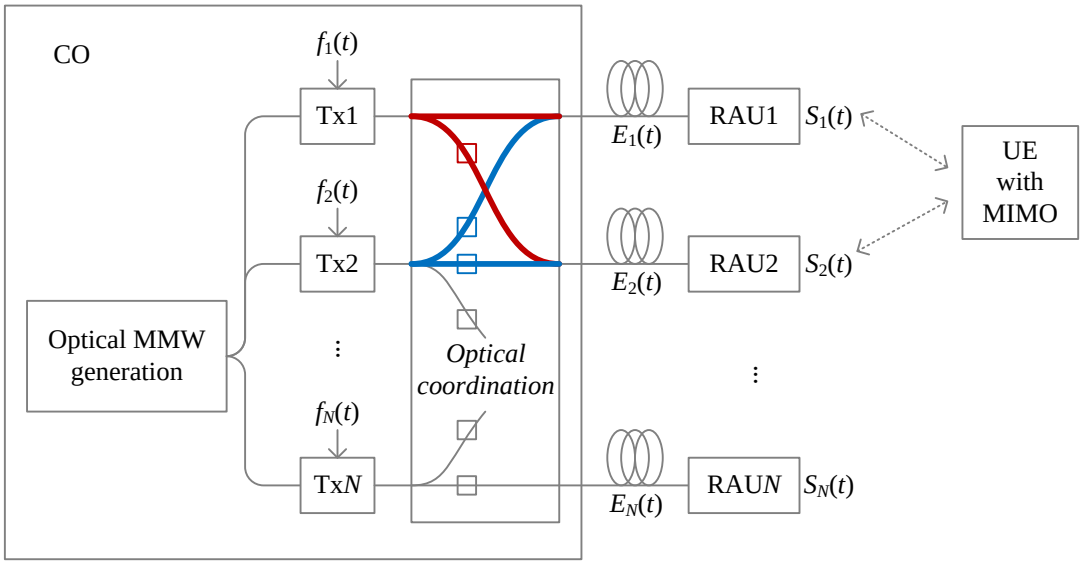

Fig. 47. Functional blocks of MMW cooperative MIMO based on RoF.

5.3.2.2 Optical coordination

In 5.3.1.2, we have derived the wireless MMW output at RAU2 in the form of (40) when the two baseband signals $f_1(t)$ and $f_2(t)$ are mixed over optical links in the form of (38). In fact, the complex matrix of the first two optical links inside the coordination module in Fig. 43 can be expressed as

$$\mathbf{A} = \begin{pmatrix} 1 & 0 \\ k\exp(j\varphi) & 1 \end{pmatrix}. \tag{44}$$

According to the relationship between (38) and (40), the wireless MMW output in a complex vector form is

$$\mathbf{S} = 2\begin{pmatrix} 1 & 0 \\ k^2\exp(j\varphi) & 1 \end{pmatrix}\begin{pmatrix} f_1(t) \\ f_2(t) \end{pmatrix}. \tag{45}$$

To generalize the application to a 2×2 cooperative MIMO as shown in Fig. 47, the optical coordination module will contain more magnitude and phase control components. In this case, we update **A** by expressing it as

$$\mathbf{A}=\begin{pmatrix} 1 & k_{12}\exp(j\varphi_{12}) \\ k_{21}\exp(j\varphi_{21}) & k_{22}\exp(j\varphi_{22}) \end{pmatrix}, \tag{46}$$

where k_{ij} and φ_{ij} denote the magnitude and phase during the coupling from link j to i, respectively. Accordingly, the wireless MMW outputs at two RAUs are

$$\mathbf{S}=2\begin{pmatrix} 1 & {k_{12}}^2\exp(j\varphi_{12}) \\ {k_{21}}^2\exp(j\varphi_{21}) & {k_{22}}^2\exp(j\varphi_{22}) \end{pmatrix}\begin{pmatrix} f_1(t) \\ f_2(t) \end{pmatrix}. \tag{47}$$

Now we consider a 2×2 MIMO system whose channel between the two pairs of antennas is represented as a 2×2 matrix, $\mathbf{H}=(h_{i,j})$. Assuming the invertibility under a low condition number structure, the inverse matrix is

$$\mathbf{H}^{-1}=\frac{h_{22}}{h_{11}h_{22}-h_{21}h_{12}}\begin{pmatrix} 1 & -h_{12}/h_{22} \\ -h_{21}/h_{22} & h_{11}/h_{22} \end{pmatrix}. \tag{48}$$

What we do for optical coordination is to establish $\mathbf{H}^{-1}$ before the wireless transmission so that the original signals $f_1(t)$ and $f_2(t)$ can be directly recovered at the receivers without MIMO decoding. In other words, we want **S** to be

$$\mathbf{S}=2\frac{h_{11}h_{22}-h_{21}h_{12}}{h_{22}}\mathbf{H}^{-1}\begin{pmatrix} f_1(t) \\ f_2(t) \end{pmatrix}. \tag{49}$$

Accordingly, the coordination matrix in the optical domain has to be in the form of

$$\mathbf{A}=\begin{pmatrix} 1 & \sqrt{\left|\frac{h_{12}}{h_{22}}\right|}\exp\left(j\arg\left(-\frac{h_{12}}{h_{22}}\right)\right) \\ \sqrt{\left|\frac{h_{21}}{h_{22}}\right|}\exp\left(j\arg\left(-\frac{h_{21}}{h_{22}}\right)\right) & \sqrt{\left|\frac{h_{11}}{h_{22}}\right|}\exp\left(j\arg\left(\frac{h_{11}}{h_{22}}\right)\right) \end{pmatrix}. \tag{50}$$

Therefore, the attenuators and delay lines are to be tuned to $\sqrt{|h_{21}/h_{22}|}$, $\sqrt{|h_{12}/h_{22}|}$, $\sqrt{|h_{11}/h_{22}|}$, and $\left(\arg(-h_{21}/h_{22})+2k\pi\right)/\Omega_{MMW}$, $\left(\arg(-h_{12}/h_{22})+2k\pi\right)/\Omega_{MMW}$,

$\left(\arg\left(h_{11}/h_{22}\right)+2k\pi\right)/\Omega_{MMW}$, respectively, to realize the optical coordination and hence cooperative MIMO.

5.3.2.3 Experimental setup and results

Fig. 48 shows the proof-of-concept setup of this multi-cell MIMO based on optical coordination in a fiber-wireless system with two RAUs. In this experimental setup, one CO, two RAUs through 20-m fiber links, and one 2-receiver UE are evaluated. At the CO, two CW lightwave sources at different wavelengths, 1564.2 nm and 1554.6 nm, are used to carry the two channels. They are initially phase-modulated by a 30-GHz tone doubled from a 15-GHz source to generate optical MMWs. At the lower link, the 30-GHz microwave input is phase-shifted to obtain a relative phase difference of φ_{22} between the two 60-GHz MMWs. After a 30/60-GHz IL and filters at the two wavelengths, the 60-GHz MMWs are amplified by two EDFAs with tunable amplification. The relative amplification between the lower and upper links is marked as a_{22}. Then the optical MMWs are intensity-modulated by two channels of OOK signals at 1-Gb/s speed. The corresponding spectra are shown in insets (a) and (b) of Fig. 48. At the frontend of the CO, an optical coordination module is implemented for realizing the ZF approach, inside of which each link is coupled with a component from the other link after an optical attenuation and delay (the delay is to introduce linear phase shift on MMWs). Here we note the attenuation and delay of the component coming from the upper link to the lower link as k_{21} and τ_{21} (marked as red), and the ones in the other direction as k_{12} and τ_{12} (marked as blue). After the fiber links, at each RAU, the beat signal at 60 GHz is radiated by a HA with 15-dBi gain and 24° half-power beamwidth. Due to the limited power and high loss, the antenna system is set to be a LoS scenario. The wireless links between transmitters and receivers are within 0.6 m, and the antenna spacing at the transmitter is subject to change to get a fairly low condition number in order to emulate the case of small antenna elements in real life.

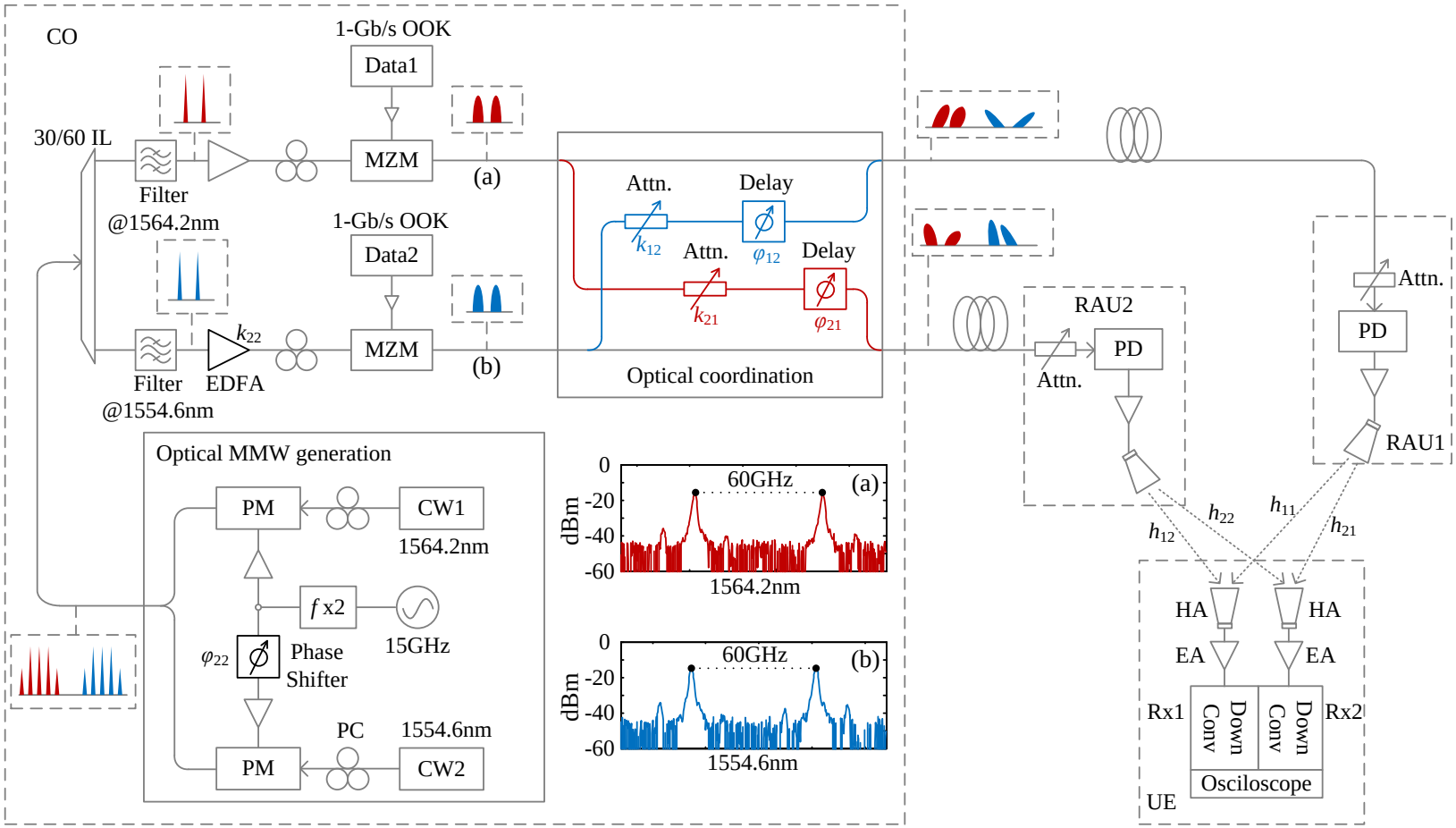

Fig. 48. Experimental setup for optical coordination in 2-cell downlink 2×2 MIMO transmission in 60-GHz fiber-wireless centralized system. Insets: generated MMW spectra of the two OOK streams.

Based on the inheritance of phase and magnitude relationships between the optical and wireless MMWs, as analyzed in 5.3.2.2, we are able to change the amplitudes and the phases of the wireless signals by changing the corresponding optical links at the CO. We use the parameters $k_{i,j}$, $\tau_{i,j}$, and φ_{22} stated above to compose the pre-coding matrix **A** in (46). Corresponding to the setup, **A** can also be written as

$$\mathbf{A} = \begin{pmatrix} 1 & k_{12}k_{22}\exp(j\Omega_{\mathrm{MMW}}\tau_{12} + j\varphi_{22}) \\ k_{21}\exp(j\Omega_{\mathrm{MMW}}\tau_{21}) & k_{22}\exp(j\varphi_{22}) \end{pmatrix}. \tag{51}$$

To tune the six parameters $k_{i,j}$, $\tau_{i,j}$, and φ_{22} according the correspondence between the entries in (50) and (51), the ideal realization is to establish a training and feedback process between the CO and the UE so as to obtain the CSI and hence the solution of the six parameters. However, due to the difficulty to manually quantify the experimental parameters, we adopt the following approach. First, to let $k_{22}^2=|h_{11}/h_{22}|$, we maximize k_{12} and k_{21} to decouple the two links and tune k_{22} to make the power received at Rx1 and Rx2 the same when only RAU1 or RAU2 is transmitting, respectively. Second, to let $k_{21}^2=|h_{21}/h_{22}|$ and $\tau_{21}=\arg(-h_{21}/h_{22})/\Omega_{\mathrm{MMW}}$, we shut down CW2, tune k_{21} so that Rx2 can receive equal power from RAU1 and RAU2, and then tune τ_{21} so that the signals from the two RAUs can cancel each other at Rx2. Third, we shut down CW1 and repeat the same steps at Rx1 to get k_{12} and τ_{12}. Fourth, we tune φ_{22} to optimize the signal quality observed from the oscilloscope. After these steps, two independent channels of decoupled OOK signals can be received at the UE.

In Fig. 49(e) and (f) we show the eye diagrams of the received error-free OOK signals at Rx1 and Rx2, respectively, by using optical coordination method without succeeding DSP. For reference, Fig. 49(a) and (b) are the eye diagrams under error-free single-input single-output (SISO) transmissions at half of the MIMO data rate. Fig. 49(c) and (d) are diagrams received at the two receivers after simultaneous transmission without doing coordination. Fig. 50 gives the BER performance versus the average optical power received at the two RAUs. The blue and green lines show a receiving

performance similar to SISO reception. The MIMO reception may perform better than SISO as a result of SNR gain at the antennas. In addition, the performances at the two receivers are well balanced with a difference less than 1 dB considering the power averaging between the two.

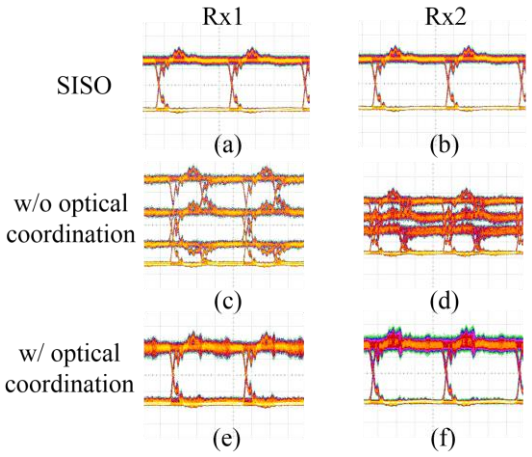

Fig. 49. Eye diagrams measured under SISO and MIMO transmissions without or with optical coordination.

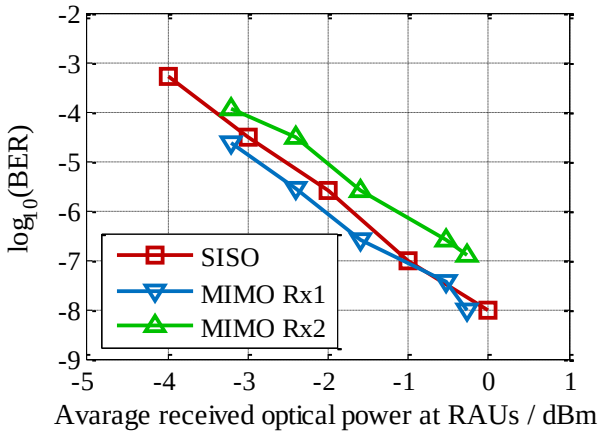

Fig. 50. BER-versus-average received optical power performances measured under SISO and photonic pre-coded MIMO transmissions.

5.3.2.4 Discussion

In the experiment we have used six parameters to realize the 2×2 complex matrix. However, one may notice that k_{22} and φ_{22} are not essential to decouple the two data streams, i.e. signals can still be recovered without knowing the two parameters, considering $\mathbf{H}^{-1}$ can be further written as

$$\mathbf{H}^{-1} = \frac{h_{22}}{h_{11}h_{22} - h_{21}h_{12}} \begin{pmatrix} 1 & -h_{12}/h_{11} \\ -h_{21}/h_{22} & 1 \end{pmatrix} \begin{pmatrix} 1 & 0 \\ 0 & h_{11}/h_{22} \end{pmatrix}. \tag{52}$$

Regardless of the diagonal matrix term in (52), the pre-coding matrix **A** can be simplified as

$$\mathbf{A} = \begin{pmatrix} 1 & k_{12}\exp(j\Omega_{\mathrm{MMW}}\tau_{12}) \\ k_{21}\exp(j\Omega_{\mathrm{MMW}}\tau_{21}) & 1 \end{pmatrix}, \tag{53}$$

including only k_{12}, τ_{12}, k_{21}, and τ_{21}. This means that we can realize the pre-coding regardless of k_{22} and φ_{22}. Nevertheless, k_{22} and φ_{22} affect the receiving quality by changing the condition number of the matrices and the approach of matrix $\mathbf{H}^{-1}$. Specifically, k_{22} and φ_{22} change the power distribution and determine the EA efficiency. In Fig. 51 we plot the BER curves of the reception without the steps of estimating k_{22} or φ_{22}. One of the receivers shows significant penalty compared with the SISO case, and the two receivers show a large performance gap between each other resulting from the deterioration of the condition number of the matrix without the estimation of k_{22} and φ_{22}, and from the unbalanced power distribution between the two optical links corresponding to the unbalanced wireless links. To give an overall view of this phenomenon, in Fig. 52 we simulate the capacity distribution over a 3m × 20m area with different setups – they have different receiver antenna spacing and different numbers of pre-coding parameters. The left plots show higher capacity over the whole plane when we consider all the six parameters to implement the pre-coding, while the right plots have degraded capacities and altered distribution compared to the left ones when only k_{12}, τ_{12}, k_{21}, and τ_{21} are taken

into account and k_{22} and φ_{22} are left as-is values whenever the position is changed. The capacity gap is approximately 2 bit/s/Hz on average.

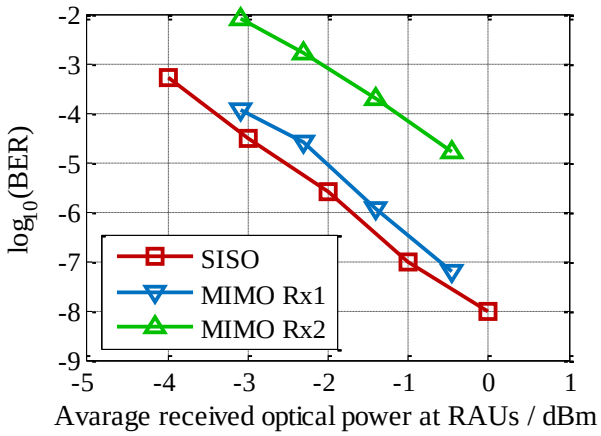

Fig. 51. BER-versus-average received optical power performances measured under SISO transmission and photonic pre-coded MIMO transmission with four parameters.

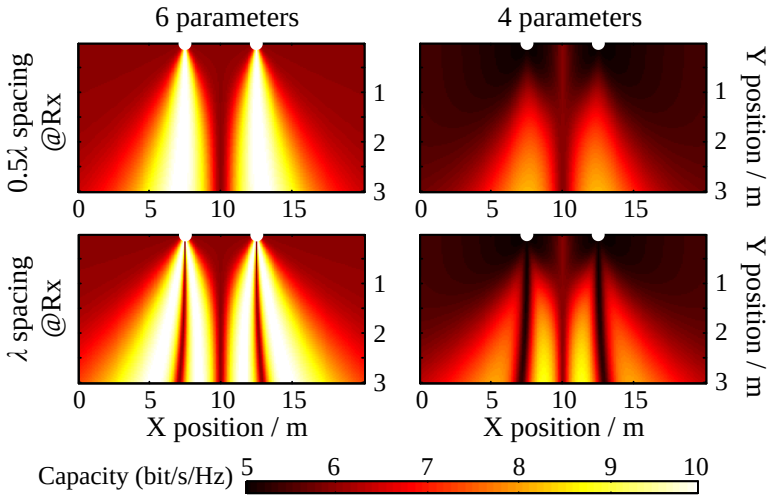

Fig. 52. Capacity over a 3m × 20m plane with two RAU positions marked as small circles and receiver antenna spacing of (up) 0.5λ and (down) λ, calculated with (left) six parameters considered or (right) only four parameters.

CHAPTER 6 SUMMARY

6.1 Technical Contributions

CoMP transmission over MMW bands is studied for future densified HetNets. Theoretical and simulation results on the one hand show that MMW CoMP in SFBC and BF downlink modes provides gains with respect to single-point transmission in terms of receiving SNR, average capacity, BER performance, and the stability of SNR, and at the same time improves infrastructure utilization, increases the chance of LoS, and reduces ICI. On the other hand, problems of distributed MMW CoMP are also revealed including overhead traffic, distributed MMW generation, and asynchronization.

The impact of asynchronization is studied [108]. Results show that MMW CoMP in both SFBC and BF modes are sensitive to CFO and TO, with minimal requirement in the level of ppb and nanosecond for CFO and TO, respectively. Parameters including carrier frequency, bandwidth, and subcarrier spacing affect the sensitivity to asynchronization whereas optimizing them provides very limited improvement. Current technologies for synchronization in HF CoMP are ineffective to solve the problem.

The concept of centralized MMW CoMP is proposed by this dissertation based on fiber-wireless centralization facing the architecture of C-RAN. RoF links for fiber-wireless centralization are studied and their performance is experimentally investigated. The feasibility of fiber-wireless centralized MMW CoMP is verified. Experimental evaluation of a fiber-wireless centralized MMW CoMP system demonstrates that received optical power has up to 3-dB gain, sensitivity to NLoS is reduced, transmission distance is extended by up to 50%, and coverage is enlarged up to 40°.

Compared with distributed MMW CoMP, fiber-wireless centralized MMW CoMP has the following advantages:

1) MMW RoF centralizes network hardware and functions, facilitates JP and resource sharing, reduces RAU complexity, and optically provides high-quality and transparent delivery of analog MMW signals.
2) Fiber-wireless centralization centralizes all data and information and their processing power, leaving the cell sites no distributed intelligence for inter-cell communications, completely avoiding any form of overhead traffic.
3) Through MWP techniques enabled by fiber-wireless centralization, homogeneous MMW signals are optically generated and distributed to RAUs, increasing the overall power and infrastructure efficiency.
4) Fiber-wireless centralization allows CoMP transmitters to share the same signaling resource that provides identical time and frequency information and therefore guarantees inherent synchronization on both time and frequency. The minimal, stable, and compensable latency of RoF links also facilitates time synchronization.

Based on the concept of fiber-wireless centralized MMW CoMP, three techniques are proposed facing various applications and research trends.

Firstly, a MMW cell grouping method is proposed for small-cell design based on fiber-wireless centralized MMW CoMP [109]. The method improves MMW coverage and continuity among densified small cells. Coordination among RAUs in an FFR scheme increases signal quality, link robustness, and smooth handoff region. In an experiment for three-RAU cell grouping, the proposed method provides a 3.5-dB improvement on signal quality at cell edges and marginal angles, a 3.5-dB improvement in optical power performance, and EVM lower than 0.12 in three NLoS transmission scenarios.

Secondly, a reconfigurable MMW radio bundling method is proposed for mobile fronthaul based on fiber-wireless centralized MMW CoMP [110]. The method applies in

multi-section fiber-wireless mobile fronthaul to improve infrastructure utilization and radio access quality and reliability. Results from a multi-point multi-section fronthaul experiment show that the method extends transmission distance by 22% and enlarges tolerance to steering angle misalignment by 76%. Under extreme optical power loss or NLoS MMW propagation, the method maintains an EVM below 11% by providing redundant fronthaul links.

Thirdly, the method of optical processing for centralized MMW CoMP is proposed facing the developing technologies of silicon photonics and all-optical processing. Enabled by the fiber-wireless platform, the method uses optical components in the centralized coordination module to realize OIC and cooperative MIMO across MMW small cells. In an OIC experiment with centralized optical coupling, the BER performance has a power penalty less than 1 dB with respect to interference-free transmission [111]. In a cooperative MIMO experiment with centralized optical pre-coding, original signals are directly recovered at the receivers with a power penalty less than 1 dB compared with SISO transmission [112], proving the multiplexing gain provided by the method.

6.2 Future Research Topics

The proposed concept of fiber-wireless centralized MMW CoMP benefits both uplink and downlink transmission. However, the dissertation mostly focuses on the downlink transmission in analysis and experimental validations. This is motivated by the fact that more critical problems exist in downlink rather than uplink in a MMW CoMP system. For example, asynchronization is much more difficult to be estimated and compensated in downlink than uplink. This is due to the nature of CoMP that the dimension of downlink receivers is smaller than the one of transmitters. Nevertheless, the role of fiber-wireless centralization in MMW CoMP uplink should also be studied as it centralizes combining algorithms, such as MRC [97, 98], in the CO. This centralization

potentially increases the efficiency of MRC by co-location computation and potentially avoids overhead traffic that used to occupy the backhaul and midhaul in a distributed system. Therefore, uplink study on the proposed concept can be a potential research direction to systematically investigate the significance of the concept.

Furthermore, we have been using 2×1 CoMP model for simplicity and have only demonstrated 2×1 setups in all experiments. This has been done because only 2×1 SFBC mode can achieve rate of 1 [67]. However, despite of the SFBC mode, higher dimension of transmitters and receivers should be taken into consideration for more general study. In fact, the higher dimension the system goes, the more severe synchronization problems it will have, the more overhead traffic it will generate, and the more complexity it will distribute. The proposed concept will consequently benefit the system better by solving those enlarged problems. In addition, massive MIMO is promising for MMW cells that have short wavelength and small antenna arrays [113, 35, 36]; multi-cell multi-user MIMO is also promising to increase the spectral efficiency. The study of fiber-wireless centralized MMW CoMP cannot be independent from these network MIMO technologies, as both CoMP and network MIMO contribute to the same channel matrix. Therefore, a joint study including both MMW CoMP with higher dimensions and other network MIMO technologies can be a potential research direction to analyze all possible gains that the proposed concept can deliver.

Lastly, our study on optical coordination gives us a promising direction to expect the evolution of future RANs. Optical processing, silicon photonics, and most importantly fiber-wireless centralization, are all enabling technologies to realize a potentially all-optical network to break through the bottleneck of electrical counterparts. In our study, very simple model is applied with limited number of optical components that are used to realize the optical processing and coordination. Although it is sufficient to achieve very fundamental OIC and MIMO functions thanks to the flat channel of MMW, a more complex model is better to be prototyped so that more advanced

processing can be applied including FDE and precoding. Therefore, study on more advanced optical coordination and processing approaches can be a long term research direction for future fiber-wireless evolution.

REFERENCES

[1] "Cisco Visual Networking Index: Global Mobile Data Traffic Forecast Update, 2015–2020 White Paper," Cisco, 3 Feb 2016. [Online]. Available: http://www.cisco.com/c/en/us/solutions/collateral/service-provider/visual-networking-index-vni/mobile-white-paper-c11-520862.pdf. [Accessed 23 Dec 2016].

[2] P. Mell and T. Grance, "The NIST Definition of Cloud Computing - Recommendations of the National Institute of Standards and Technology," NIST Special Publication 800-145, 2011.

[3] *Evolved Universal Terrestrial Radio Access (E-UTRA) (Release 10), 3GPP TS 36.101,* 2011.

[4] A. Damnjanovic et al, "A survey on 3GPP heterogeneous networks," *IEEE Wireless Communications,* vol. 18, no. 3, pp. 10-21, 2011.

[5] D. Lopez-Perez et al, "Enhanced intercell interference coordination challenges in heterogeneous networks," *IEEE Wireless Communications,* vol. 18, no. 3, pp. 22-30, 2011.

[6] K. Hosseini, J. Hoydis, S. t. Brink and M. Debbah, "Massive MIMO and small cells: How to densify heterogeneous networks," in *IEEE International Conference on Communications (ICC),* Budapest, 2013.

[7] G. Boudreau et al, "Interference coordination and cancellation for 4G networks," *IEEE Communications Magazine,* vol. 47, no. 4, pp. 74-81, 2009.

[8] *Evolved Universal Terrestrial Radio Access (E-UTRA) and Evolved Universal Terrestrial Radio Access Network (E-UTRAN) Overall description (Release 8), 3GPP TS36.300,* 2009.

[9] J. Wannstrom, K. Mallinson and WiseHarbor, "Heterogeneous Networks in LTE," 3GPP, [Online]. Available: http://www.3gpp.org/technologies/keywords-acronyms/1576-hetnet. [Accessed 23 Dec 2016].

[10] *Coordinated multi-point operation for LTE physical layer aspects (Release 11), 3GPP TR36.819,* 2011.

[11] D. Marabissi, G. Bartoli, R. Fantacci and M. Pucci, "An Optimized CoMP Transmission for a Heterogeneous Network Using eICIC Approach," *IEEE Transactions on Vehicular Technology*, vol. 65, no. 10, pp. 8230-8239, 2016.

[12] Y.-N. R. Li, J. Li, W. Li, Y. Xue and H. Wu, "CoMP and interference coordination in heterogeneous network for LTE-Advanced," in *IEEE Globecom Workshops*, Anaheim, 2012.

[13] P. Marsch and G. Fettweis, Coordinated Multi-Point in Mobile Communications: From Theory to Practice, Cambridge University Press, 2011.

[14] V. Jungnickel et al, "Backhaul requirements for inter-site cooperation in heterogeneous LTE-Advanced networks," in *IEEE International Conference on Communications Workshops (ICC)*, 2013.

[15] S. Iwelski et al, "On the performance of CoMP transmission in unsynchronized networks with timing offset," in *IEEE Wireless Communications and Networking Conference (WCNC)*, 2014.

[16] C. Hoymann, L. Falconetti and R. Gupta, "Distributed Uplink Signal Processing of Cooperating Base Stations Based on IQ Sample Exchange," in *IEEE International Conference on Communications (ICC)*, 2009.

[17] J. Wannstrom, "Carrier Aggregation explained," 3GPP, June 2013. [Online]. Available: http://www.3gpp.org/technologies/keywords-acronyms/101-carrier-aggregation-explained. [Accessed 23 Dec 2016].

[18] *Mobile Backhaul Implementation Agreement – Phase 2, Amendment 1 – Small Cells, MEF22.1.1*, 2014.

[19] B. Singh, S. Hailu, K. Koufos, A. A. Dowhuszko, O. Tirkkonen, R. Jäntti and R. Berry, "Coordination protocol for inter-operator spectrum sharing in co-primary 5G small cell networks," *IEEE Communications Magazine*, vol. 53, no. 7, pp. 34-40, 2015.

[20] D. Flore, "LAA standardization: coexistence is the key," 3GPP, 13 July 2016. [Online]. Available: http://www.3gpp.org/news-events/3gpp-news/1789-laa_update. [Accessed 23 Dec 2016].

[21] T. Wheeler, "Leading towards Next Generation "5G" Mobile Services," FCC, 3 Aug 2013. [Online]. Available: https://www.fcc.gov/news-events/blog/2015/08/03/leading-towards-next-generation-5g-mobile-services. [Accessed 23 Dec 2016].

[22] L. Han and N. Hua, "A Distributed Time Synchronization Solution without Satellite Time Reference for Mobile Communication," *IEEE Communications*

Letters, vol. 17, no. 7, pp. 1447-1450, 2013.

[23] R. Irmer et al, "Coordinated multipoint: Concepts, performance, and field trial results," *IEEE Communications Magazine,* vol. 49, no. 2, pp. 102-111, 2011.

[24] *IEEE 802.11ay specification,* 2017.

[25] H. Mehrpouyan et al, "Hybrid millimeter-wave systems: a novel paradigm for HetNets," in *IEEE Communications Magazine,* 2015.

[26] S. Okasaka, R. J. Weiler, W. Keusgen, A. Pudeyev, A. Maltsev, I. Karls and K. Sakaguchi, "Proof-of-Concept of a Millimeter-Wave Integrated Heterogeneous Network for 5G Cellular," *Sensors*, vol. 16, no. 9, p. 1362, 2016.

[27] *Millimeter Wave Propagation: Spectrum Management Implications, FCC,* 1997.

[28] *Channel Models for 60 GHz WLAN Systems, IEEE 802.11-09/0334r7,* 2010.

[29] T. S. Rappaport, G. R. MacCartney, M. K. Samimi and S. Sun, "Wideband Millimeter-Wave Propagation Measurements and Channel Models for Future Wireless Communication System Design," *IEEE Transactions on Communications,* vol. 63, no. 9, pp. 3029-3056, 2015.

[30] J. Lu, D. Steinbach, P. Cabrol, P. Pietraski and R. V. Pragada, "Propagation characterization of an office building in the 60 GHz band," in *The 8th European Conference on Antennas and Propagation (EuCAP 2014),* The Hague, 2014.

[31] L. H. Gonsioroski and L. da Silva Mello, "Preliminary results of measurements of penetration losses through buildings at 2.5 GHz," in *SBMO/IEEE MTT-S International Microwave & Optoelectronics Conference (IMOC),* Rio de Janeiro, 2013.

[32] K. Sato, T. Manabe, T. Ihara, H. Saito, S. Ito, T. Tanaka, K. Sugai, N. Ohmi, Y. Murakami, M. Shibayama, Y. Konishi and T. Kimura, "Measurements of reflection and transmission characteristics of interior structures of office building in the 60-GHz band," *IEEE Transactions on Antennas and Propagation,* vol. 45, no. 12, pp. 1783-1792, 1997.

[33] G. R. MacCartney, S. Deng, S. Sun and T. S. Rappaport, "Millimeter-Wave Human Blockage at 73 GHz with a Simple Double Knife-Edge Diffraction Model and Extension for Directional Antennas," in *IEEE 84th Vehicular Technology Conference (VTC2016-Fall),* 2016.

[34] R. Baldemair et al, "Ultra-dense networks in millimeter-wave frequencies," *IEEE Communications Magazine,* vol. 53, no. 1, pp. 202-208, 2015.

[35] W. Roh, J.-Y. Seol, J. Park, B. Lee, J. Lee, Y. Kim, J. Cho, K. Cheun and F. Aryanfar, "Millimeter-wave beamforming as an enabling technology for 5G cellular communications: theoretical feasibility and prototype results," *IEEE Communications Magazine,* vol. 52, no. 2, pp. 106-113, 2014.

[36] A. L. Swindlehurst, E. Ayanoglu, P. Heydari and F. Capolino, "Millimeter-wave massive MIMO: the next wireless revolution?," *IEEE Communications Magazine,* vol. 52, no. 9, pp. 56-62, 2014.

[37] T. Bai, A. Alkhateeb and R. W. Heath, "Coverage and capacity of millimeter-wave cellular networks," *IEEE Communications Magazine,* vol. 52, no. 9, pp. 70-77, 2014.

[38] "CableFree: Gigabit Wireless Networking," CableFree, [Online]. Available: http://www.cablefree.net/cablefree-millimeter-wave-mmw/. [Accessed 23 Dec 2016].

[39] X. Li, J. Yu, Z. Zhang and Y. Xu, "Field Trial of 80-Gb/s PDM-QPSK Signal Delivery over 300-m Wireless Distance with MIMO and Antenna Polarization Multiplexing at W-Band," in *Optical Fiber Communication Conference (OFC),* Los Angeles, 2015.

[40] J. Yu, X. Li, J. Zhang and J. Xiao, "432-Gb/s PDM-16QAM signal wireless delivery at W-band using optical and antenna polarization multiplexing," in *The European Conference on Optical Communication (ECOC),* Cannes, 2014.

[41] S. Piersanti et al, "Millimeter waves channel measurements and path loss models," in *IEEE International Conference on Communications (ICC),* 2012.

[42] A. Maltsev et al, "Performance evaluation of the isolated mmWave small cell," in *IEEE 26th Annual International Symposium on Personal, Indoor, and Mobile Radio Communications (PIMRC),* 2015.

[43] U. Rizvi et al, "Impact of RF circuit imperfections on multi-carrier and single-carrier based transmissions at 60 GHz," in *IEEE Radio and Wireless Symposium,* 2008.

[44] *C-RAN - The Road Towards Green RAN (white paper), V2.5,* 2011.

[45] K. Miyamoto, S. Kuwano, J. Terada and A. Otaka, "Analysis of mobile fronthaul bandwidth and wireless transmission performance in split-PHY processing architecture," *Optics Express,* vol. 24, no. 2, pp. 1261-1268, 2016.

[46] K. Miyamoto, S. Kuwano, J. Terada and A. Otaka, "Performance evaluation of mobile fronthaul optical bandwidth reduction and wireless transmission in Split-PHY processing architecture," in *Optical Fiber Communications Conference and*

Exhibition (OFC), Anaheim, 2016.

[47] J. Terada, T. Shimada, T. Shimizu and A. Otaka, "Optical Network Technologies for Wireless Communication Network," in *42nd European Conference on Optical Communication*, Dusseldorf, Germany, 2016.

[48] *Common Public Radio Interface (CPRI); Interface Specification, V7.0,* 2015.

[49] *Open base station architecture initiative – BTS system reference document, V2.0,* 2006.

[50] Y. Okumura and J. Terada, "Optical Netowrk Technologies and Architectures for Backhaul/Fronthaul of Future Radio Access Supporting Big Mobile Data," in *Optical Fiber Communication Conference (OFC)*, 2014.

[51] C. Lim, A. Nirmalathas, M. Bakaul, P. Gamage, K.-L. Lee, Y. Yang, D. Novak and R. Waterhouse, "Fiber-Wireless Networks and Subsystem Technologies," *Journal of Lightwave Technology,* vol. 28, no. 4, pp. 390-405, 2010.

[52] A. Ng'oma, "Radio-over-fiber technologies for multi-Gb/s wireless applications," in *Optical Fiber Communication Conference (OFC)*, 2013.

[53] X. Liu, H. Zeng, N. Chand and F. Effenberger, "Efficient Mobile Fronthaul via DSP-Based Channel Aggregation," *Journal of Lightwave Technology,* vol. 34, no. 6, pp. 1556-1564, 2016.

[54] C. Liu et al, "A Novel Multi-Service Small-Cell Cloud Radio Access Network for Mobile Backhaul and Computing Based on Radio-Over-Fiber Technologies," *IEEE Journal of Lightwave Technology,* vol. 31, no. 17, pp. 2869-2875, 2013.

[55] T. Kuri et al, "Reconfigurable Dense Wavelength-Division-Multiplexing Millimeter-Waveband Radio-Over-Fiber Access System Technologies," *Journal of Lightwave Technology,* vol. 28, no. 16, pp. 2247-2257, 2010.

[56] J. Yu et al, "Cost-Effective Optical Millimeter Technologies and Field Demonstrations for Very High Throughput Wireless-Over-Fiber Access Systems," *Journal of Lightwave Technology,* vol. 28, no. 16, pp. 2376-2397, 2010.

[57] M. Presi et al, "Adaptive antenna system for OFDMA WiMAX radio-over-fiber links using a directly modulated R-SOA and optical filtering," in *Optical Fiber Communication Conference (OFC)*, 2009.

[58] H. Bolcskei and A. Paulraj, "Space-frequency coded broadband OFDM systems," in *IEEE Wireless Communications and Networking Conference (WCNC)*, 2000.

[59] L. Shao and S. Roy, "Rate-one space-frequency block codes with maximum diversity for MIMO-OFDM," *IEEE Transactions on Wireless Communications*, vol. 4, no. 4, pp. 1674-1687, 2005.

[60] M. Baker, "REV-090003r1 LTE-Advanced Physical Layer," in *IMT-Advanced Evaluation Workshop*, Beijing, 2009.

[61] B. Ozbek and D. Le Ruyet, "Low complexity ZF receiver for orthogonal SFBC-OFDM in broadband wireless channels," *Electronics Letters*, vol. 42, no. 8, pp. 479-481, 2006.

[62] Y.-i. Min, H.-m. Park, J.-h. Jang, K.-d. Kim and H.-j. Choi, "The Enhanced Decoding Method for QO-SFBC System in Frequency Selective Fading Channel Environment," *Journal of Networks*, vol. 6, no. 3, pp. 378-386, 2011.

[63] H. Eghbali, M. Stojanovic and S. Muhaidat, "Differential decoding for SFBC OFDM systems in underwater MIMO channels," in *IEEE International Conference on Acoustics, Speech and Signal Processing (ICASSP)*, Florence, 2014.

[64] G. Bauch, "Space-time block codes versus space-frequency block codes," in *The 57th IEEE Semiannual Vehicular Technology Conference*, 2003.

[65] L. Zheng and D. Tse, "Diversity and multiplexing: a fundamental tradeoff in multiple-antenna channels," *IEEE Transactions on Information Theory*, vol. 49, no. 5, pp. 1073-1096, 2003.

[66] G. L. Stüber, "Received envelop and phase distribution," in *Principles of Mobile Communication (Second Edition)*, New York, Boston, Dordrecht, London, Moscow, Kluwer Academic Publishers, 2002, pp. 50-55.

[67] V. Tarokh et al, "Space-time block codes from orthogonal designs," *IEEE Transactions on Information Theory*, vol. 45, no. 5, pp. 1456-1467, 1999.

[68] J. Proakis and M. Salehi, "Optimum Receivers for AWGN Channels," in *Digital Communications*, New York, McGraw-Hill, 2008, pp. 160-289.

[69] B. Everitt, The Cambridge Dictionary of Statistics, Cambridge, UK: Cambridge University Press, 1998.

[70] T. Grujic and M. Bonkovic, "Measurement and Analysis of Human Hand Kinematics," *International Journal of Medical, Health, Biomedical, Bioengineering and Pharmaceutical Engineering*, vol. 9, no. 2, pp. 97-102, 2015.

[71] B. Razavi, "Design of Millimeter-Wave CMOS Radios: A Tutorial," *IEEE Transactions on Circuits and Systems I: Regular Papers*, vol. 56, no. 1, pp. 4-16,

2009.

[72] *Radio subsystem synchronization (Release 10), 3GPP TS 45.010 (Section 5.1),* 2011.

[73] *Base Station (BS) radio transmission and reception (Release 11), 3GPP TS 36.104,* 2012.

[74] *Verizon 5G TF; Air Interface Working Group; Verizon 5th Generation Radio Access; Physical channels and modulation (Release 1), V1.7,* 2016.

[75] M. Toeltsch and A. F. Molisch, "Efficient OFDM transmission without cyclic prefix over frequency-selective channels," in *11th IEEE International Symposium on Personal Indoor and Mobile Radio Communications*, London, 2000.

[76] M. Pampin, "LTE Requires Synchronization And Standards Support," Electronic Design, 15 Oct 2012. [Online]. Available: http://electronicdesign.com/communications/lte-requires-synchronization-and-standards-support. [Accessed 23 Dec 2016].

[77] "Base Station Solutions," Rakon, 10 June 2016. [Online]. Available: http://www.rakon.com/component/docman/doc_download/509-base-station-solutions. [Accessed 23 Dec 2016].

[78] "What is a GPS/Multi-GNSS Disciplined Oscillator (GPSDO/GNSSDO)?," Furuno, [Online]. Available: http://www.furuno.com/en/gnss/technical/gnssdo. [Accessed 23 Dec 2016].

[79] *Timing and synchronization aspects in packet, ITU-T G.8261/Y.1361,* 2013.

[80] *IEEE Standard for a Precision Clock Synchronization Protocol for Networked Measurement and Control Systems, IEEE Std 1588™-2008,* 2008.

[81] *Network Time Protocol Version 4: Protocol and Algorithms Specification, IETF RFC 5905,* 2010.

[82] *Timing characteristics of synchronous Ethernet equipment slave clock, ITU-T G.8262/Y.1362,* 2015.

[83] "Improving the Accuracy of a Crystal Oscillator," Semtech, Jan 2009. [Online]. Available: http://www.semtech.com/images/datasheet/xo_precision_std.pdf. [Accessed 23 Dec 2016].

[84] "Rubidium Sync Holdover Ensures Mobile Service Availability (White paper)," Microsemi, 2014. [Online]. Available: http://www.microsemi.com/document-portal/doc_view/134355-rubidium-sync-holdover-ensures-mobile-service-

availability. [Accessed 23 Dec 2016].

[85] Y. Wu, S. Attallah and J. W. M. Bergmans, "Carrier Frequency Offset Estimation for Multi-User MIMO OFDM Uplink Using CAZAC Sequences," in *IEEE Wireless Communications and Networking Conference*, Budapest, 2009.

[86] Y.-R. Tsai, H.-Y. Huang, Y.-C. Chen and K.-J. Yang, "Simultaneous Multiple Carrier Frequency Offsets Estimation for Coordinated Multi-Point Transmission in OFDM Systems," *IEEE Transactions on Wireless Communications,* vol. 12, no. 9, pp. 4558-4568, 2013.

[87] Y. Jiang, X. Zhu, E. Lim and Y. Huang, "Joint semi-blind channel equalization and ICI mitigation for carrier aggregation based CoMP OFDMA systems with multiple CFOs," in *IEEE International Conference on Communications (ICC)*, Budapest, 2013.

[88] Z. Jia, Optical millimeter-wave signal generation, transmission and processing for symmetric super-broadband optical-wireless access networks, 2008.

[89] M. Zhu, L. Zhang, J. Wang, L. Cheng, C. Liu and G.-K. Chang, "Radio-over-fiber access architecture for integrated broadband wireless services," *IEEE Journal of Lightwave Technology*, vol. 31, no. 23, pp. 3614-3620, 2013.

[90] F. Khan, Z. Pi and S. Rajagopal, "Millimeter-wave mobile broadband with large scale spatial processing for 5G mobile communication," in *50th Annual Allerton Conference on Communication, Control, and Computing (Allerton)*, Monticello, IL, 2012.

[91] S. Inudo, Y. Yoshida, A. Kanno, P. T. Dat, T. Kawanishi and K. Kitayama, "On the MIMO channel rank deficiency in W-band MIMO RoF transmissions," in *Optical Fiber Communications Conference and Exhibition (OFC)*, Los Angeles, CA, 2015.

[92] P. Wang, Y. Li, L. Song and B. Vucetic, "Multi-gigabit millimeter wave wireless communications for 5G: from fixed access to cellular networks," *IEEE Communications Magazine,* vol. 53, no. 1, pp. 168-178, 2015.

[93] N. Saquib et al, "Fractional frequency reuse for interference management in LTE-advanced hetnets," *IEEE Wireless Communications,* vol. 20, no. 2, pp. 113-122, 2013.

[94] T. Pfeiffer, "Next generation mobile fronthaul architectures," in *Optical Fiber Communications Conference and Exhibition (OFC)*, Los Angeles, 2015.

[95] X. Pang, A. Lebedev, J. J. V. Olmos and I. T. Monroy, "Multigigabit W-Band (75–110 GHz) Bidirectional Hybrid Fiber-Wireless Systems in Access Networks,"

IEEE Journal of Lightwave Technology, vol. 32, no. 23, pp. 4585-4592, 2014.

[96] S. Babiel, A. Stöhr, A. Kanno and T. Kawanishi, "Radio-over-fiber photonic wireless bridge in the W-Band," in *IEEE International Conference on Communications Workshops (ICC)*, Budapest, 2013.

[97] L. C. Choo and T. T. Tjhung, "Selection diversity combining diversity reception of DQPSK for indoor millimetre-wave communications," *Electronics Letters,* vol. 32, no. 21, pp. 1971-1972, 1996.

[98] Z. Chen, J. Yuan and B. Vucetic, "Analysis of Transmit Antenna Selection/Maximal-Ratio Combining in Rayleigh Fading Channels," *IEEE Transactions on Vehicular Technology*, vol. 54, no. 4, pp. 1312-1321, 2005.

[99] J. Kakande, R. Slavík, F. Parmigiani, P. Petropoulos and D. J. Richardson, "All-optical processing of multi-level phase shift keyed signals," in *Optical Fiber Communication Conference*, Los Angeles, 2012.

[100] V. C. Duarte, M. V. Drummond and R. N. Nogueira, "Photonic true-time delay beamforming system for a phased array antenna receiver," in *SBMO/IEEE MTT-S International Microwave and Optoelectronics Conference (IMOC)*, Porto de Galinhas, 2015.

[101] A. Poustie, "Highly integrated InP-based subsystems for all-optical processing," in *Conference on Optical Fiber Communication (OFC/NFOEC), collocated National Fiber Optic Engineers Conference*, San Diego, 2010.

[102] P. Dong, "Silicon photonic integrated circuits for high-capacity optical communications," in *21st OptoElectronics and Communications Conference (OECC) held jointly with 2016 International Conference on Photonics in Switching (PS)*, Niigata, Japan, 2016.

[103] C. Liu et al, "A novel in-building small-cell backhaul architecture for cost-efficient multi-operator multi-service coexistence," in *Optical Fiber Communication Conference (OFC)*, 2013.

[104] E. Torkildson et al, "Indoor Millimeter Wave MIMO: Feasibility and Performance," *IEEE Transactions on Wireless Communications,* vol. 10, no. 12, pp. 4150-4160, 2011.

[105] C. Sheldon et al, "A 60GHz line-of-sight 2×2 MIMO link operating at 1.2Gbps," in *IEEE Antennas and Propagation Society International Symposium*, 2008.

[106] C. Wang et al, "Cooperative MIMO channel models: A survey," *IEEE Communications Magazine,* vol. 48, no. 2, pp. 80-87, 2010.

[107] C.-T. Lin et al, "MIMO-enhanced radio-over-fiber system at 60GHz," in *37th European Conference and Exhibition on Optical Communication (ECOC)*, 2011.

[108] L. Cheng, M. M. U. Gul, F. Lu, M. Zhu, J. Wang, M. Xu, X. Ma and G.-K. Chang, "Coordinated Multipoint Transmissions in Millimeter-Wave Radio-over-Fiber Systems," *IEEE Journal of Lightwave Technology*, vol. 34, no. 2, pp. 653-660, 2016.

[109] L. Cheng, M. Xu, F. Lu, J. Wang, J. Zhang, X. Ma and G.-K. Chang, "Millimeter-Wave Cell Grouping for Optimized Coverage based on Radio-over-Fiber and Centralized Processing," in *Optical Fiber Communication Conference and Exposition (OFC)*, Anaheim, CA, 2016.

[110] L. Cheng, F. Lu, J. Wang, M. Xu, S. Shen and G.-K. Chang, "Millimeter-Wave Radio Bundling for Reliable Transmission in Multi-Section Fiber-Wireless Mobile Fronthaul," in *Optical Fiber Communication Conference and Exposition (OFC)*, Los Angeles, 2017.

[111] L. Cheng, M. Zhu, M. M. U. Gul, X. Ma and G.-K. Chang, "Adaptive Photonics-Aided Coordinated Multipoint Transmissions for Next-Generation Mobile Fronthaul," *IEEE Journal of Lightwave Technology*, vol. 32, no. 10, pp. 1907-1914, 2014.

[112] L. Cheng, M. Zhu, J. Wang, M. Xu, F. Lu and G.-K. Chang, "Photonic Precoding for Millimeter-Wave Multicell MIMO in Centralized RoF System," *IEEE Photonics Technology Letters*, vol. 26, no. 11, pp. 1116-1119, 2014.

[113] V. Jungnickel, K. Manolakis, W. Zirwas, B. Panzner, V. Braun, M. Lossow, M. Sternad, R. Apelfrojd and T. Svensson, "The role of small cells, coordinated multipoint, and massive MIMO in 5G," *IEEE Communications Magazine*, vol. 52, no. 5, pp. 44-51, 2014.

[114] J. Yu et al, "Optical millimeter-wave generation or up-conversion using external modulators," *IEEE Photonics Technology Letters*, vol. 18, no. 1, pp. 265-267, 2006.

VITA

LIN CHENG

CHENG was born in Beijing, China. He received the B.S. degree and M.S. degree (first-class Hons.) in electronic engineering from Tsinghua University, Beijing, China, in 2009 and 2012, respectively. He is currently working toward the Ph.D. degree in electrical and electronics engineering at Georgia Institute of Technology, Atlanta, GA.

During his Ph.D. study, he works with his advisor Prof. Gee-Kung Chang on several projects under the NSF Center of Fiber-Wireless Integration and Networking. He was also a research intern in CableLabs, Louisville, CO, in 2013 and 2014, Futurewei Technology, Inc., Bridgewater, NJ, in 2015, and Corning, Inc., Painted Post, NY, in 2016. His research interests are mainly focused on system design and signal processing techniques for optical and wireless access systems. He has authored and co-authored more than 50 peer-reviewed journal and international conference papers.